Studies on Mechanisms of Microstructure and Micro-texture Development during Thermo-mechanical processes in single/multiphase Zirconium based alloys

By

S. K. Jha

(ENGG01201004022)

Bhabha Atomic Research Centre, Mumbai

A thesis submitted to the

Board of Studies in Engineering Sciences

In partial fulfillment of requirements

For the Degree of

DOCTOR OF PHILOSOPHY
of
HOMI BHABHA NATIONAL INSTITUTE

HOMI BHABHA NATIONAL INSTITUTE

August, 2017

DECLARATION

I, hereby declare that the investigation presented in the thesis has been carried out by me. The work is original and has not been submitted earlier as a whole or in part for a degree / diploma at this or any other Institution / University.

S. K. Jha

Homi Bhabha National Institute

Recommendations of the Viva Voce Committee

As members of the Viva Voce Committee, we certify that we have read the dissertation prepared by Sanjay Kumar Jha entitled "Studies on Mechanisms of Microstructure and Micro-texture Development during Thermo-mechanical processes in single/multiphase Zirconium based alloys" and recommend that it may be accepted as fulfilling the thesis requirement for the award of Degree of Doctor of Philosophy.

Chairman – Prof. K. B. Khan	**Date:** 30.10.17
Guide / Convener – Prof. D. Srivastava	**Date:** 30.10.17
Co-guide - Prof. G. K. Dey — Gautam Kumar Dey	**Date:** 30.10.2017
Examiner – Prof. Satyam Suwas — Satyam S	**Date:** 30.10.2017
Member 1- Prof. Ashok Arya	**Date:** 30.10.2017
Member 2- Prof. R. N. Singh — R N Singh	**Date:** 30.10.2017

Final approval and acceptance of this thesis is contingent upon the candidate's submission of the final copies of the thesis to HBNI.

I/We hereby certify that I/we have read this thesis prepared under my/our direction and recommend that it may be accepted as fulfilling the thesis requirement.

Date:

Place:

Gautam Kumar Dey
<Signature>
Co-guide (if applicable)

<Signature>
Guide

DECLARATION

I, hereby declare that the investigation presented in the thesis has been carried out by me. The work is original and has not been submitted earlier as a whole or in part for a degree / diploma at this or any other Institution / University.

S. K. Jha

Homi Bhabha National Institute

SYNOPSIS

To utilise the vast reserves of Thorium available in India it is proposed to use Thorium as fertile fuel alongwith Plutonium and Uranium (${}_{92}U^{233}$) in Advanced Heavy Water Reactor (AHWR). AHWR is a 300MWe, heavy water moderated, boiling light water cooled natural circulation reactor. The fuel consists of (Th–Pu)O_2 and (Th–${}_{92}U^{233}$)O_2 pins. Ziracloy-2 will be used for Fuel clad as the reactor is of boiling water type where Zircaloy-2 has long history as clad tube [1]. Expected burnup of fuel in AHWR is likely to be more than 40000 MWD/T and added with power ramp, there is need to improve the performance

Experiment conducted to show the effect of Iodine with Zircaloy, has confirmed that due to combined presence of Iodine vapor and a stress at 300 to 400^{0}C, Zircaloy cracked [2,3]. Since, failure of clad took place due to presence of stress and corrosive fission gas it was identified as the process of stress corrosion cracking (SCC). Since, crucial factor in the cracking of fuel cladding is the concentrated stress at the inner surface of the fuel cladding during a power ramp. This takes place invariably due to expansion of pellet, therefore the process is called pellet clad interaction (PCI). To reduce the stress in clad tube inner surface of the tube was modified [4-6]. Two types of changes in clad tube were attempted. These included, the metallurgically bonded 75 µm thick zirconium layer and 10µm electrodeposited copper [4].At low-burnup and power ramp tests, both barrier types were found successful.

After conducting initial trial, millions of fuel pins with Zirconium lined Zircaloy-2 tube were irradiated in BWR which gave life of fuel clad tube for exposure at 43000MWD/T(bundle average). In case of pure Zirconium as liner, even small ingress of oxygen in the inner side of clad tube, catastrophic failure can take place during service [4]. Therefore, new concept in liner material is addition of about 0.3.% to 0.4.% Sn in Zirconium which results in improved corrosion resistance to large extent without sacrificing the ductility of the material which is requisite for controlling stress due to PCI. For this work dilute ZrSn alloy has been selected for study. Experimental trials have shown [7] that metallurgical bond, uniform thickness of liner and desired chemical composition of the Zirconium barrier are essential requisite for double clad tube to provide PCI resistance. The Zr-barrier cladding tubes are manufactured by co-extrusion at elevated temperature to form a composite tube shell of Zircaloy with a liner of Zirconium, followed by co-reduction in a pilger mill in several passes with intermediate recrystallization anneals. It has been shown [15] that three attributes of the zirconium barrier are essential to provide PCI resistance: (a) the metallurgical bond (b) the thickness of the liner and (c) the purity or softness of the liner material. The bond is quite remarkable in that recystallization occurs across the Zirconium -Zircaloy interface. Thus, the interface is transgranular with no physical boundary that might impede the flow[14]. Dilute ZrSn alloy being developed as liner for clad requires understanding of bulk deformation properties in as cast condition as well as in wrought conditions. During bulk deformation material experiences not only high temperature and high strain rate but also very high strain. Therefore, there is need to understand the effect of all these variables on microstructure and texture development under different set of conditions. In literature, data available on deformation of Zirconium as well as Zr with different percentage of Sn has been extensively considered for wrought material. And it has been established that initial microstructure and texture play dominant role in deformation of an alloy. In this work deformation behavior of as cast material has been studied in detail. Flow properties measured elsewhere mainly uses wrought product for deformation which is not useful for cast material. It is essential to know the thorough understanding of not only about the flow behavior of as cast alloy but also development of microstructure and texture during high temperature deformation. In the light of these issues present thesis is focused on the microstructural and microtextural evolution in case of Zr-Sn alloy (used as a liner material) in the temperature and strain rate regime relevant for actual component fabrication.

Summary of Chapters

The brief description of the present thesis highlighting the background of the work is given in Chapter 1. In Chapter 2, the relevant literature pertaining to the area of research has been detailed. The present status of knowledge on the zirconium alloys, their deformation behavior, texture and microstructure evolution is elaborated in this chapter. The simulation and modelling literature of hot deformation processes is discussed. The experimental methods used for the present study are described briefly in this chapter. These included the processing methods and characterization techniques. Chapter 4 deals with the study of flow behavior of Zr-Sn alloy. The microstructure and texture evolution as a function of hot deformation parameters have been studied and rationalized. The optimum deformation conditions by study of the processing maps is detailed in Chapter 5. This chapter also includes the determination of the constitution equations for Zr-Sn alloy. The chapter six gives the simulation and experimental results for co-extrusion of Zr-Sn liner and Zircaloy clad materials. The chapter 7 also presents the details of the simulation of Zr-2.5Nb-Cu alloy extrusion. In the last Chapter 8, the summary of the results of the present thesis work is presented in brief.

The brief details of the important results obtained in presesis work is given below

Processing Map

Flow curves obtained have shown non-uniform deformation behaviour of this alloy. In low temperature region i.e. upto 700^0C strain hardening takes place continuously for almost all strain rates and its effect is more for higher strain rates. To verify the inhomogeneity in deformation behaviour, processing map is generated using thermo mechanical data obtained by hot compression testing of cast Zirconium Sn alloy. Processing map developed using hot compression test results , shows wide region covered with instabilities especially at low temperature and high strain rate areas and high efficiency i.e. onset of dynamic recovery and recrystallisation in high temperature and high strain rate region. Shaded region of the figure given below represents the region of flow instabilities and remaining areas of map shows efficiency contour. Microstructure obtained for temperature of 650^0C and strain rate of 1.0 S^{-1} shows flow instability in the form of adiabatic shear band figure 2 (a). Two micrographs shown below in figures 2(b) and 2 (c) representing the dynamically recrystallised microstructure lies in the region of high efficiency.

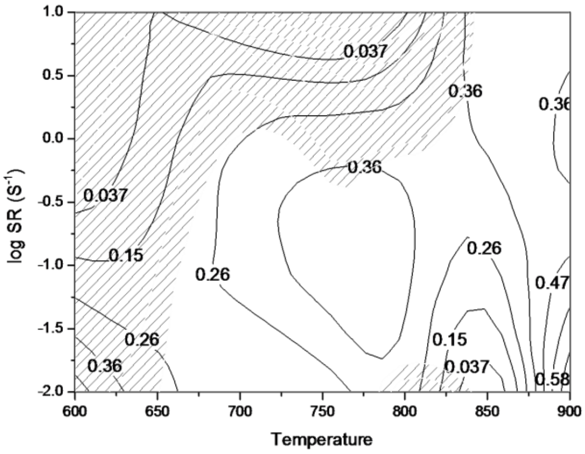

Fig 1. Processing map of Zr Sn alloy at 0.6 strain

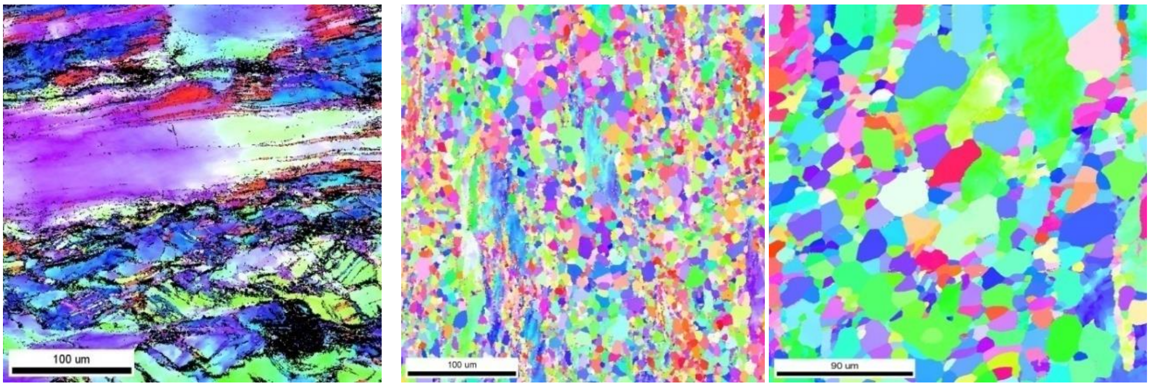

(a) 650^{0}C, strain rate 1.0 S^{-1} (b) 750^{0}C, strain rate 5 S^{-1} (c) 900^{0}C, strain rate 10 S^{-1}

Fig 2: Microstructure of deformed samples taken from different regions of map.

From these studies two new findings have been obtained a) processing map for cast Zirconium Sn alloys and b) possibility of deforming cast Zirconium alloys at very high strain rate to obtain fully recrystallised microstructure. Both results are quite useful in the areas of bulk deformation which is different from conventional understanding of cast alloys as per which lower strain rate deformations are preferable for the cast structures.

Constitutive Equation

The deformation mechanisms of Zirconium based alloys are complex, as mechanism changes not only with change in temperature and strain rate but also with strain. Incorporation of all of these complexities in deformation modeling of thermo mechanical processes (such as hot extrusion) is rather complex and computationally intensive. It is desirable to have a constitutive law that can satisfactorily capture the flow behavior of the alloy which can be used for entire domain of deformation range. The accuracy of constitutive equation thus developed can be validated by fitting it into standard FEM based simulation software and by modeling a deformation process such as extrusion, forging and rolling it will be possible to study the effect of various conditions. Considering above requirements hot deformation studies of cast Zirconium Sn alloy has been carried out. Thermo mechanical simulator was used initially to obtain flow stress data at different temperatures, strain rates and strains.

Constitutive equation developed using thermo mechanical processing data provides relationship of flow stress with the strain; deformation temperature and strain rate of Zr-Sn alloy during high temperature deformation has been expressed as follows:

$$\sigma_{p=} \frac{1}{\alpha}\sinh^{-1}\left(\frac{\dot{\varepsilon}\, exp(Q|RT)}{A}\right)^{1/n} \qquad (1)$$

Flow stress data obtained from the isothermal hot compression tests at different strain rates ($\dot{\epsilon}$) were used to estimate the materials constants in the equation 1. Using the value of flow stress obtained for different strain rates and strain, values of material constants A, n, α and Q were calculated. These constants have been used to develop the constitutive equation to calculate flow stress at different strain and strain rate. The flow stress obtained from experimental and constitutive equation are plotted in figure 3 which shows the error of about 4%, which is well within the acceptable range. Therefore, constitutive equation developed can be utilised for simulation and modelling of any hot deformation process.

Strain Compensated Arrhenius model

From equation 1 it is obvious that the influence of strain is not taken into account in Arrhenius model of constitutive equation. However, it has been reported that the activation energy of any alloy and other constants are significantly affected by strain [8-11]. Flow stress usually varies with strain especially under the occurrence of dynamic recrystallisation which could cause predominantly decrease in flow stress. Thus, Arrhenius model was inappropriate for describing the dynamic softening phenomenon. In order to provide more precise prediction on flow stress, the strain compensated Arrhenius model was developed considering the effect of strain on all material constants. To find the effect of strain on material constants α, Q, n and A under different strains similar steps as adopted to calculate for strain 0.6 were applied starting from minimum value of 0.1- 0.6 in the interval of 0.1 and values obtained for all constants were plotted against strain. Curve fitting of 4th order polynomial were used to find constants for empirical equation.

$$\alpha = B_0 + B_1\varepsilon + B_2\varepsilon^2 + B_3\,\varepsilon^3 + B_4\,\varepsilon^4 \qquad (2)$$

$$n = C_0 + C_1\varepsilon + C_2\varepsilon^2 + C_3\,\varepsilon^3 + C_4\,\varepsilon^4 \qquad (3)$$

$$Q = D_0 + D_1\varepsilon + D_2\varepsilon^2 + D_3\,\varepsilon^3 + D_4\,\varepsilon^4 \qquad (4)$$

$$lnA = E_0 + E_1\varepsilon + E_2\varepsilon^2 + E_4\,\varepsilon^4 \qquad (5)$$

Re-Validation of constitutive equation

Importance of constitutive equation in thermomechanical analysis of a material is well known. However, its application depends on its accuracy and validity in different domains of thermo mechanical processing. After validation of constitutive equation in section 2.2 with flow stress values obtained by experiments in the present study, applicability of constitutive equation for extrusion was examined by comparing the extrusion forces obtained from simulation and actual extrusion. For validation extrusion of ZrSn tube at 3780 T Horizontal extrusion press was done, which is considered to be more appropriate in validation of Constitutive equation. A commercial finite element program HyperXtrude was used to simulate the process.

Table1

Coefficients of polynomial fitting curves for material constants:

α		n		Q		lnA	
B0	.0347	C0	3.6422	D0	506.22	E0	53.365
B1	-0.2091	C1	40.123	D1	-730.03	E1	- 39.774
B2	0.817	C2	- 201.32	D2	1345.3	E2	- 40.405
B3	- 1.3775	C3	373.51	D3	-466.67	E3	287.21
B4	0.85420	C4	-242.19	D4	-433.33	E4	-264.92

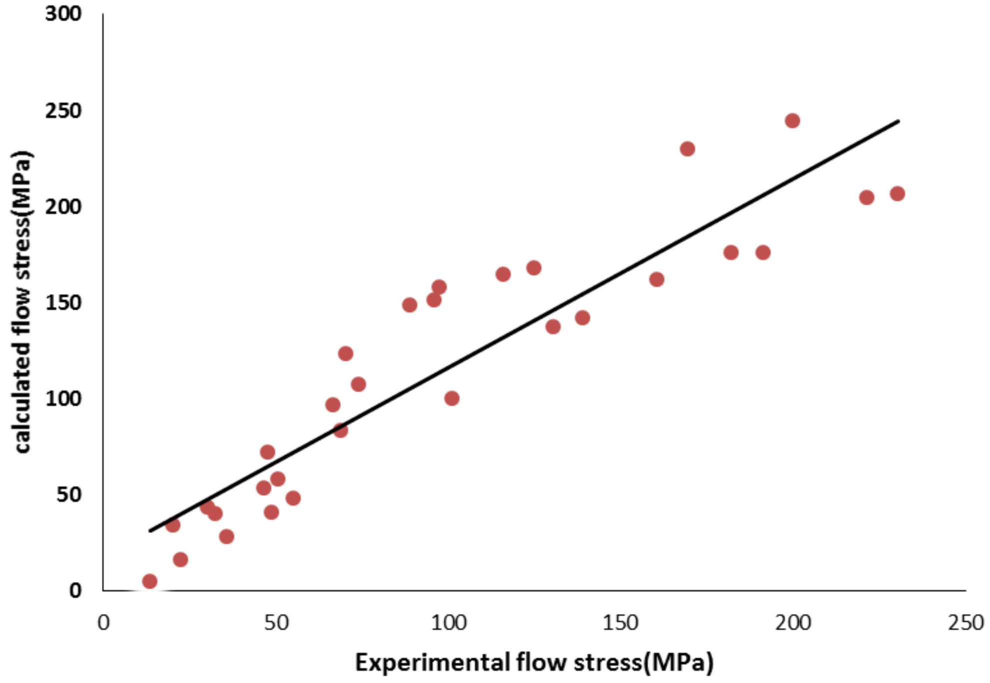

Fig 3. Plot of experimental flow stress Vs calculated flow stress

This program uses arbitrary Lagrangian-Eulerian formulation to compute velocity, temperature, stress, strain, and pressure in the flow field and based on the stresses, forces on the tool are also computed.

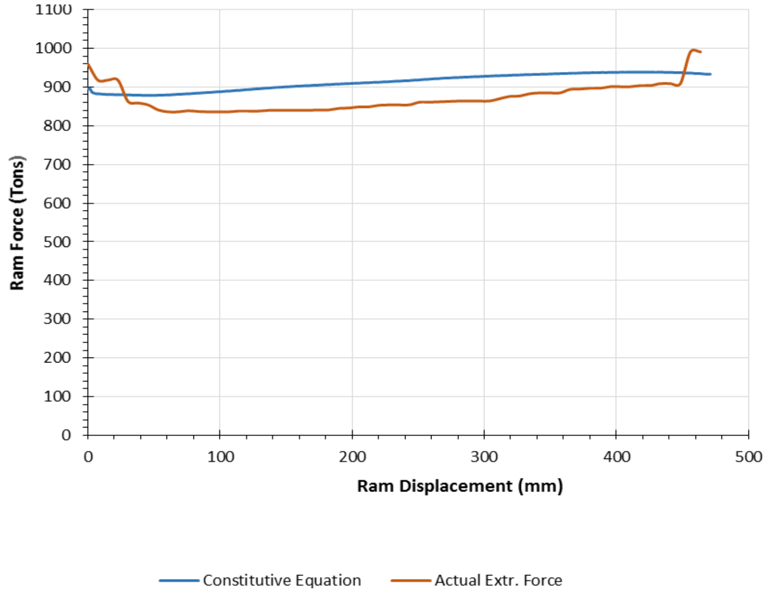

Fig 4. Comparison of Load Vs ram displacement curve

Conservation of mass, momentum, and energy principles produce the fundamental equations that govern flow and heat transfer of incompressible viscous fluids. These equations are written in terms of primitive variables (velocity, pressure, and temperature) with reference to Eulerian frame, i.e., a space-fixed system of coordinates through which the fluid flows. Extrusion load recorded during extrusion at 3780 T HEP for ZrSn alloy and simulations using constitutive equation were compared in extrusion of 50 mm X 8 mm WT size ZrSn alloy. Extrusion load obtained using constitutive equation results and actual extrusion has a difference of 5%.

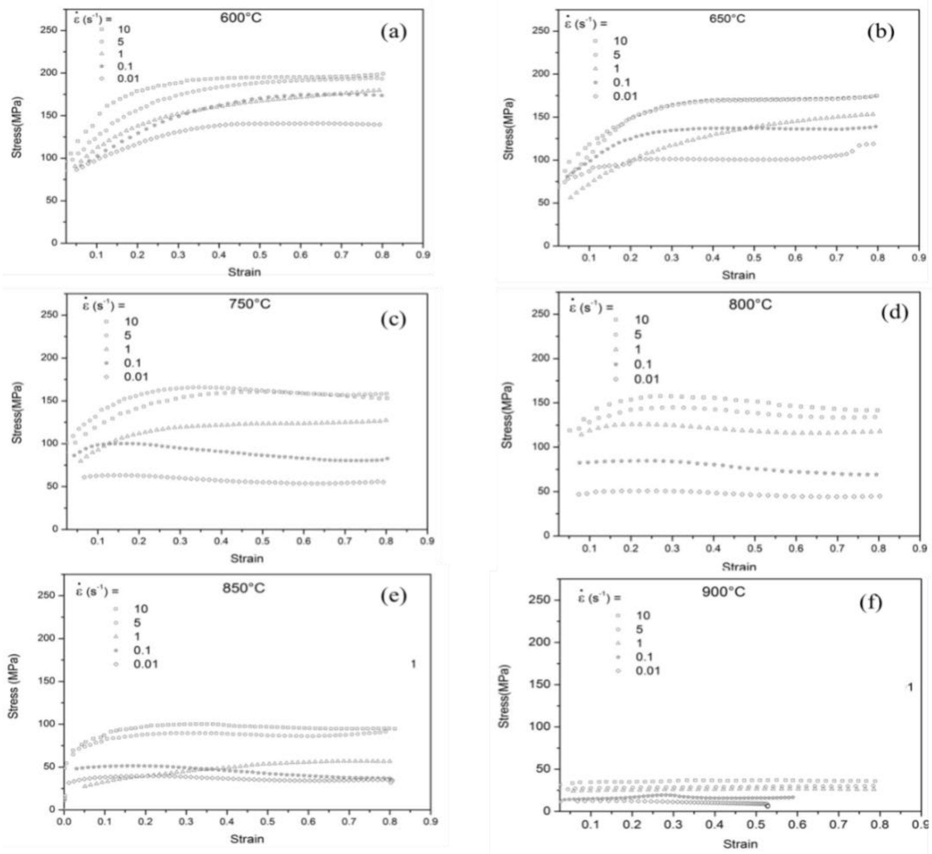

Fig. 5: The true stress-strain curves for the Zr-Sn alloy at different strain rates at temperatures of (a) 600° C, (b) 650° C, (c) 750° C, (d) 800° C, (e) 850° C and (f) 900° C.

Microstructure and Microtexture development during Thermo mechanical Processing

In chapter 4 thermo-mechanical behaviour of the dilute Zr-Sn alloy has been presented. It has been shown that considerable variation in flow stress takes place during deformation at high temperature and strain rate. Processing maps have been developed using adiabatically corrected flow stress versus strain curves. Processing map shows both efficiency of deformation and instability and thereby provides the different domain of deformation. To investigate in detail about deformation mechanism in this alloy it is necessary to study the development of microstructure at different temperature and strain rate. Cylindrical specimens for compression testing with 15 mm height and 10 mm diameter were machined along the axial direction of VAR melted ingot and figure (6) shows the microstructure of as cast ingot. Hot compression tests were performed for a series of strain rates and temperatures in a controlled manner in a Gleeble®-3800thermo-mechanical simulator. The temperature was varied from 600° to 900° C covering the domains of single alpha phase field to the beta phase field. Scanning Electron Microscope (SEM) based Electron Backscattered Diffraction (EBSD) was used to characterize the hot deformed microstructures. The bulk textures of the deformed samples were recorded using a PANalytical™ PRO-MRD XRD system. These measurements were taken from the middle region of the specimen and hence, are unaffected by the localized dead-metal zone near the sample-loading plate interface. Four incomplete pole figures ({01-11}, {01-12}, {0002} and {01-13}) were measured and used for constructing the orientation distribution functions (ODF). The basal pole figures were computed from the ODFs.

Flow behaviour and Microstructure development

The series of flow curves presented in Fig. 4(a)-(f) depict the flow behaviour of the Zr-0.3Sn alloy as a function of temperature and strain rate. Considerable differences in the strain hardening behaviour as a function of both temperature and strain rate are evident. While lower temperature regime (below 750°C) is dominated by higher strain hardening, high temperature (800°C) deformation is characterized by appreciably lower hardening, if any. The work hardening nature was predominant in the flow curves at the temperatures of 600° and 650° C. While some work hardening behaviour was observed for the strain rates higher than 1 S^{-1} at 750° C, for lower strain rates at this temperature and for all strain rates at higher temperatures, negligible work hardening was seen. It could be clearly seen that the material underwent lesser work hardening as the temperature was increased. In fact, at the temperature of 900° C, the flow curves are effectively flat, for all strain rates considered.

Another interesting observation was that the flow curves for different strain rates were widely separated at lower temperatures and were spaced much closer at higher temperatures. This showed that the flow stress sensitivity to the strain rate was an inverse function of temperature. At 1s^{-1}, more signatures of deformation (like grain fragmentation, relatively higher proportion of non indexed regions) could be seen. At high strain rates, some instances of deformation twinning could be seen. The analysis of the twins confirmed them to be of 85°<2-1-10> type, known as tensile twins. No recrystallized grains could be identified at any strain rates at this deformation temperature [12]. Thus the temperature of 600° C was seen to be insufficient to promote dynamic recrystallization. In contrast to the lower temperatures (600 and 650°C), dynamically recrystallized grains were distinctly observed throughout all strain rates at this deformation temperature. This observation has an important practical implication in terms of the processing of this alloy. Deformation of this alloy at 700° C at higher strain rate gives very fine grain recrystallised structure and with increase in temperature there is continuous recrystallisation but microstructure varies with change in strain rates which is also shown in processing map where instability region for high temperature strain rates has been observed for temperatures 600 to 650^{0}C. Deformation at 900°C and low strain rates, the microstructure was essentially composed of $\beta \rightarrow \alpha$ transformation variants [13] in a typical Widmanstatten morphology, signifying no appreciable dynamic recrystallization. Increase in the strain rate resulted in the breakdown of the transformation microstructure and the generation of an increasing proportion of equiaxed grains. It could be seen that while the microstructure generated at 10 s^{-1} was fully equiaxed, the high temperature also resulted in rapid grain coarsening (grain diameter ~50 μm). Thus, a high strain rate was essential at this high temperature to generate sufficient stored energy to initiate dynamic recrystallization. This result is very useful for industrial application where beta alloy can be worked at very high strain rate or high rate of deformation can be given to get the product in short time with higher recovery. Thus, a high strain rate was essential at this high temperature to generate sufficient stored energy to initiate dynamic recrystallization.

This result is very useful for industrial application where beta alloy can be worked at very high strain rate or high rate of deformation.

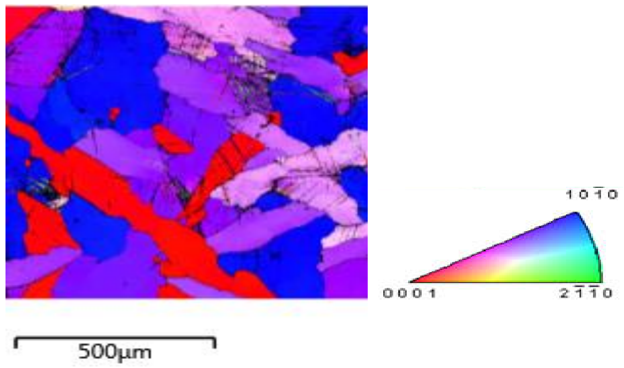

Fig. 6: The microstructure of the as-cast material

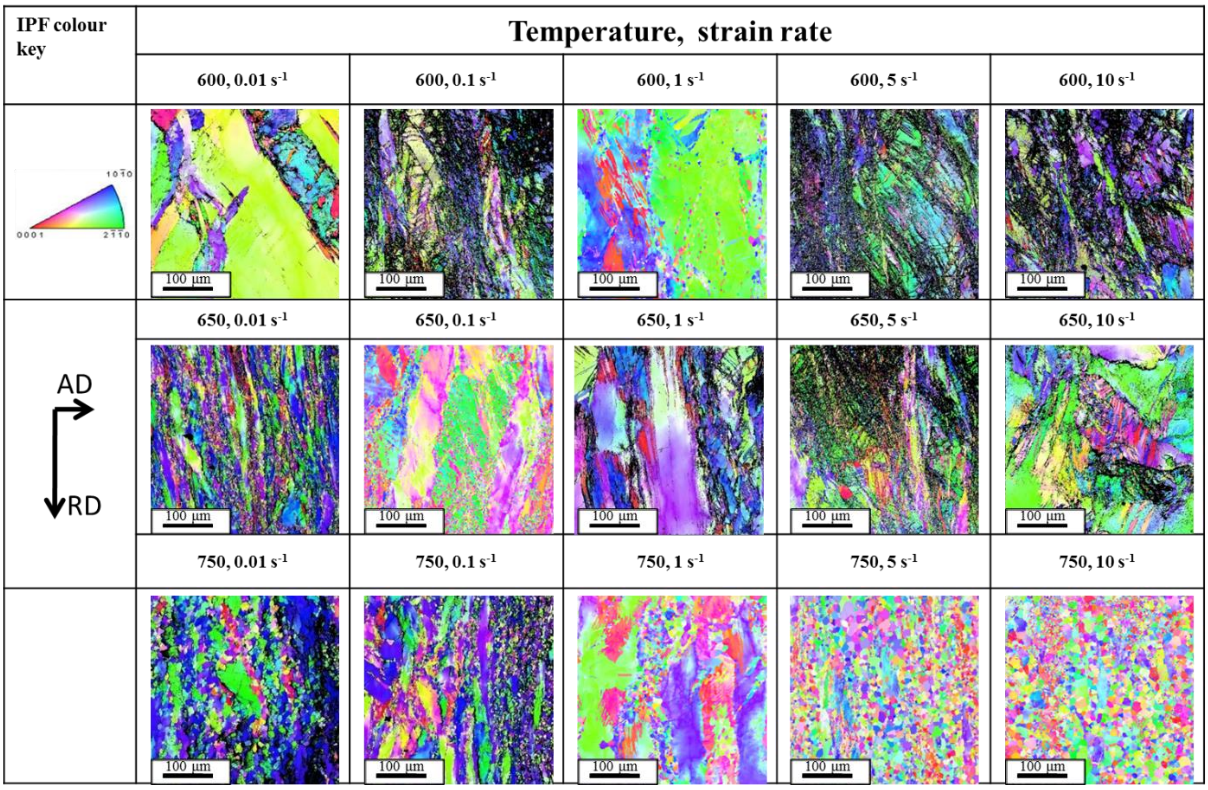

Fig 7: The evolution of the microstructure after compression at different strain rates and temperatures. RD and AD denote radial and axial directions respectively.

Co - extrusion of Zircaloy-2 and Zr-Sn

As discussed above dilute Zr-Sn alloy having Sn in the range of 0.1%-0.4% is used as liner material in fuel clad of light water nuclear reactors where Zircaloy-4 and Zircaloy-2 are selectively used as clad material. Experimental trials have shown [7] that metallurgical bond, uniform thickness of liner and desired chemical composition of the ZrSn alloy barrier are essential to provide PCI resistance. The Zr-barrier cladding tubes are manufactured by co-extrusion at elevated temperature to form a composite tube shell of Zircaloy with a liner of Zirconium. During deformation in addition to metallurgical bonding of liner with base clad material, thickness of liner is very crucial and it has been observed by conducting number of trials that liner thickness is very sensitive to processing parameters. In practice it is difficult to optimise the thermo-mechanical parameters by conducting number of trials as liner thickness variation depends on number process variables. Therefore, to study the effect of co extrusion parameters on liner thickness variation, simulation of co-extrusion process have been attempted which is being discussed in next chapter.

4.2 Numerical Simulation of Co-Extrusion

An FEM model was developed for numerical simulation of Co-extrusion process in Deform-2D Finite element software. The axi-symmetry model showing the objects and their positions in co-extrusion is shown in fig. 8.

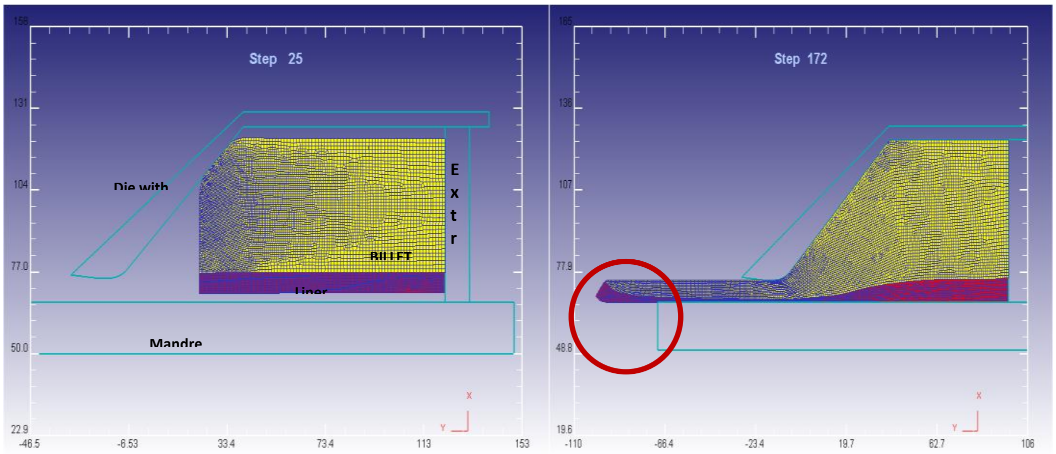

Fig 8 a) Co-extrusion Finite element model showing the billet and liner assembled position w.r.t extrusion tools and b) liner bursting in the leading end

The figure 8 shows bursting of liner prior to billet and the increased liner thickness in the leading end. The 4-noded quadrilateral elements were used for meshing and remeshing in the model. The Lagrangian incremental approach was used for finite element analysis and Newton Raphson methodology was employed for convergence. The simulation was successfully carried out by giving a sticking condition on all along the length of the liner against the actual condition of sticking at both edges. Analysis of Co-Extrusion simulations was done for number of parameters in the process however validation was done mainly for liner thickness. After the thorough analysis of the various parameters in Co–extrusion model, shop floor experiment for co-extrusion was carried out on 3780 T horizontal extrusion press. Fig 9 shows that the peak co-extrusion load in case of experiment is approximately 1300T and then begins to decrease. The peak load in simulated condition is below the actual condition and is close to 1180 T. However, further the decreasing trend in load is similar before the steady state co-extrusion load condition is achieved between 1070 to 1085T which was very close to the load range 1020 to 1100T predicted by co-extrusion simulation. Both the load curves were observed to be converging beyond 20% co-extrusion. The maximum variation observed in the steady state part of the co-extrusion was found to be only 4 %.

The actual liner thickness and co-extrusion load obtained in the experimental co extrusion were compared with the results obtained for simulated co-extrusion at the optimized parameters in figure 10. Liner thickness was obtained after metallographic examinations of multiple samples under SEM. Table 2 indicates that the ZrSn liner thickness in the range of 570 to 660µ was obtained which is very close to the predicated range of 550 to 620µ for co-extrusion in the employed rage of extrusion parameters. Microstructure of as extruded duplex clad is shown in figure 11. The results obtained from this simulation have been applied in optimisation of the co-extrusion parameters for development of ZrSn lined Zircaloy-2 double clad tube by co-extrusion.

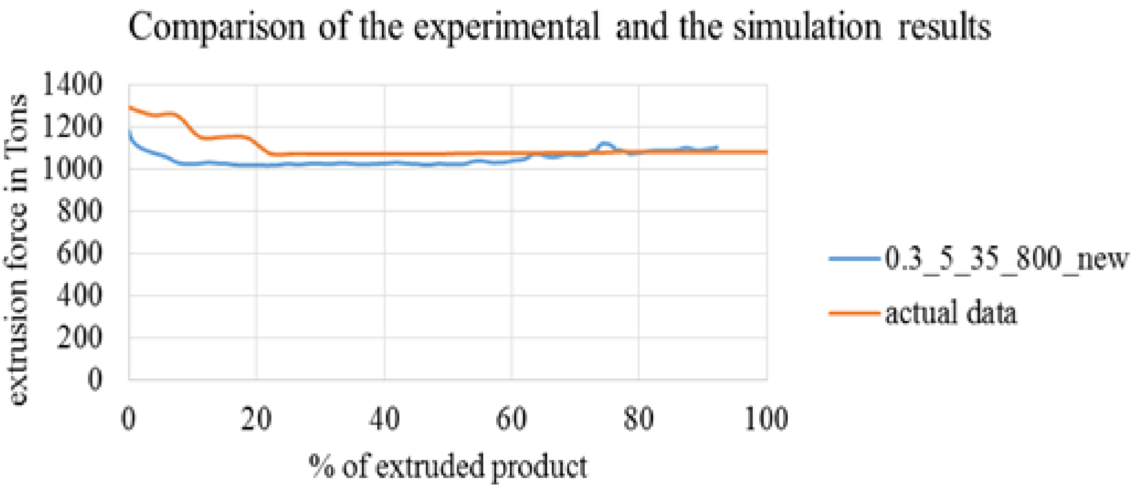

Fig 9. Comparison of the simulated and experimental load curve for Co-extrusion of Zr-2/Zr-Sn

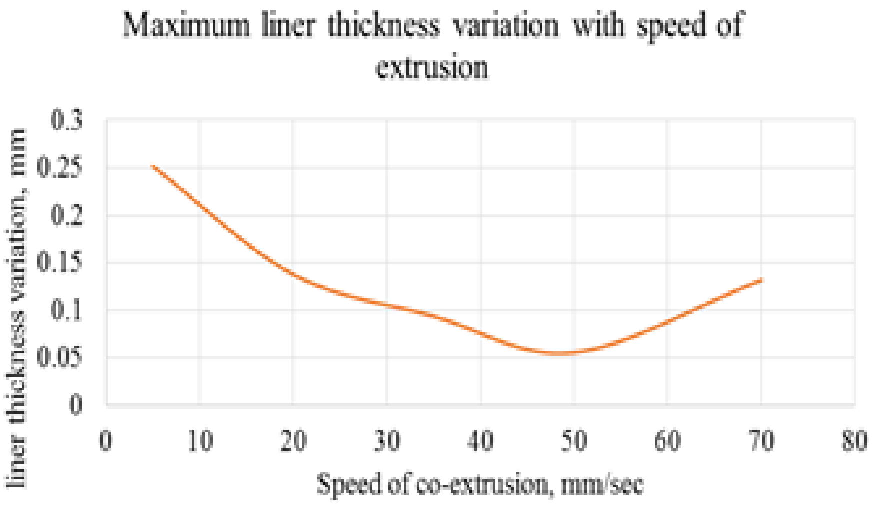

Fig.10 Maximum Liner thickness variation with speed of co-extrusion

Table 2 Simulated and experimental results for co-extrusion of Zr-2 and Zr-Sn alloys

Parameter in steady state	**Experimental result**	**Simulated result**
Extrusion Load	1070 – 1085 tons	1020 to 1100 tons
Liner thickness	572 to 660 µm	550 to 620 µm

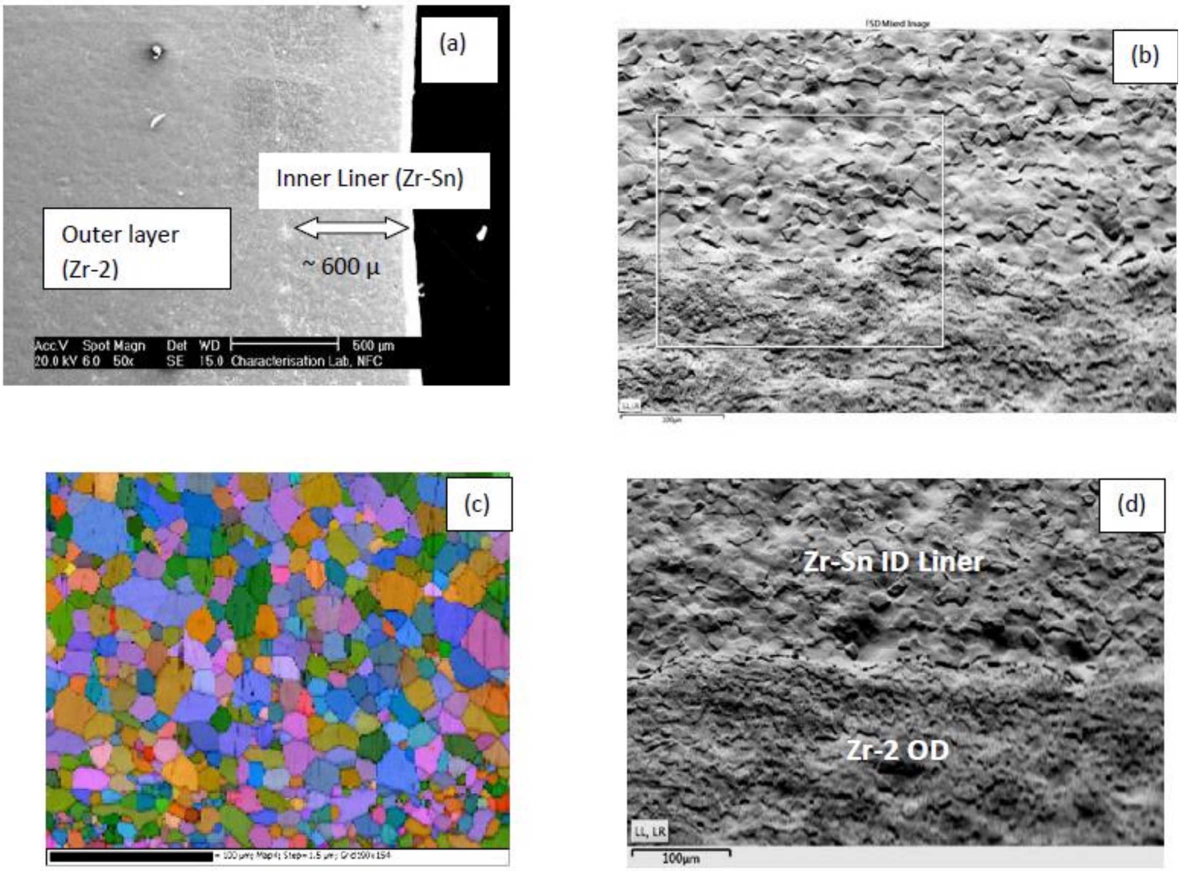

Fig. 11 Microstructure of Co extruded Showing the a)Low Mag SEM image (b) image of the region covering Zr-Sn layer and Zr-2 c) Orientation Map of interface region d) High Mag SEM image of interface region showing well bonded layer Zr-2 respectively

Thermo-Mechanical Simulation of Zr-2.5Nb-0.5Cu Alloy

Zr-2.5Nb-0.5Cu alloy is an important structural component of pressurized heavy water reactors (PHWRs) and used to manufacture garter spring. It separates pressure tube from calandria tube. It is a helical extension or compression spring whose ends are connected in order to form each spring into a circle which exerts radial forces around pressure tube. Garter spring needs adequate strength to support pressure tube and it should prevent contact between pressure tube and calandria tube in the event of diametral creep of pressure tube. Copper is added to Zr-2.5%Nb alloy used as pressure tube material in PHWRs to improve its strength by precipitation. The corrosion properties are also improved due to addition of copper. The properties of Zr-2.5Nb-0.5Cu alloy are very sensitive to the thermo mechanical fabrication steps starting with hot extrusion followed by multiple working with intermediate annealing. In extrusion, correct design and control of process requires, among other things, the determination of the deformation mechanics involved in the process.

Fig. 12(a), (b) and (c) show there is wide variation of flow stress at low temperature with true strain (ε) and as expected flow stress decrease with increase in temperature for a given strain rate ($\acute{\varepsilon}$). Extent of decrease in flow stress is higher for low temperature flow curves i.e. $700^{o}C$ & $750^{0}C$ compare to 815, 850 and $925^{0}C$. The flow of material at lower temperatures do not stabilizes with the increase of strain which can lead plastic instability while deformation of material in lower temperature region where volume fraction of alpha phase is likely to be very high.

Modelling and simulation of Zr-2.5Nb-0.5Cu hot extrusion

Computation was made for velocity, temperature, stress, strain and pressure in the flow field and based on the stresses, forces on the tool were also determined. While deciding the meshing both tetrahedron and hexahedron elements were tried. The tetrahedrons however showed a stiff behaviour and the extrusion force was heavily overestimated by these elements whereas hexahedral elements indicated reasonably good results hence hexahedral elements were finally used in the extrusion simulation.

FEM based HyperXtrude program was used in conjunction with the determined flow properties to optimize the extrusion parameters. Look up table (LUT) was used for simulation purpose and its validity was checked using extrusion force directly obtained actual extrusion trials.

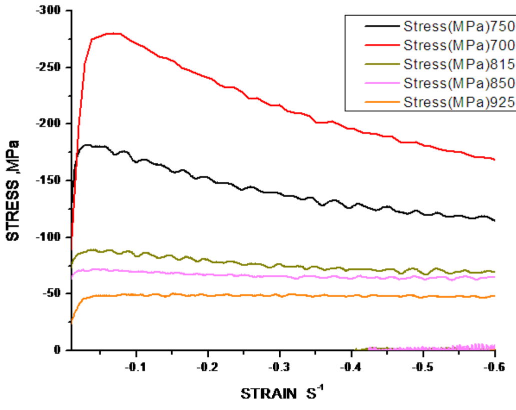

12 a

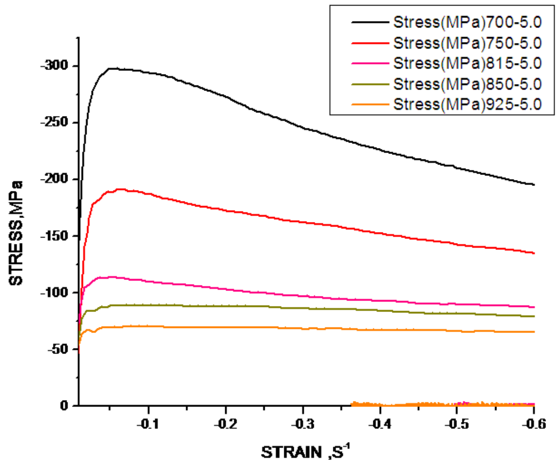

12 b

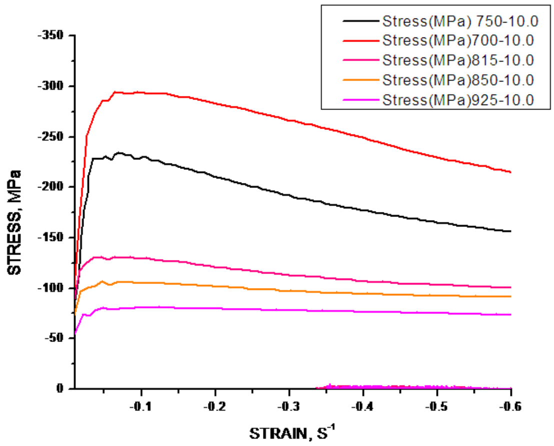

12c

Fig. 12 Flow stress of Zr-2.5Nb-0.5Cu

Results of extrusion Simulation

Extrusion forces were determined by inserting data obtained from hot compression tests conducted using Gleeble-3500 for different temperature and strain rate. Fig. 13(a) shows the variation of extrusion force for die angle of 60^0 and at temperature of 815^0 C, as a function of ram speed from 20 mm/sec to 50 mm/sec. there is increase in peak extrusion force as ram velocity increases which results in increase of strain rates. Similar trend in increase of peak flow stress can be seen in the flow curves obtained for all temperatures. It can be seen that for a given ram speed as the extrusion length decreases, the extrusion load increases which is contrary to the conventional extrusion concept of reduced friction force load should decrease. In this case load increase due to temperature loss is more pre dominant than reduced friction load with surface area contact with container.

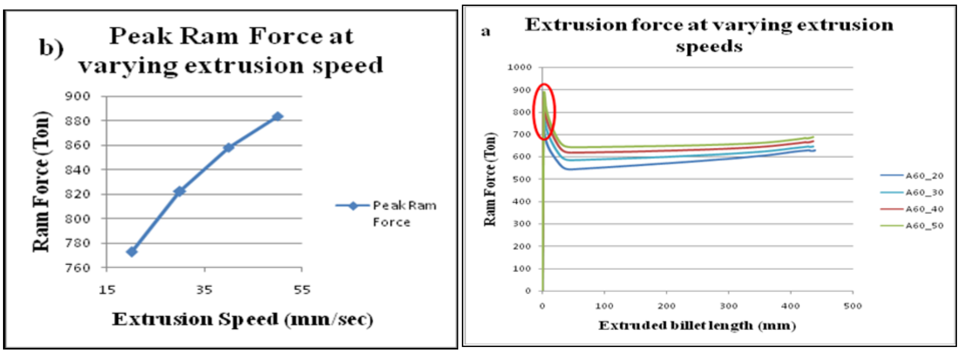

Fig. 13 Variation of extrusion forces with extrusion speed and ram displacement

The peak extrusion loads at 815^{o}C for different ram speed is shown in fig 13 b. It can be seen that with increasing initial speed the peak load requirement for extrusion increases almost linearly, this suggest that for a given extrusion temperature there ram speed should be minimum to reduce peak load. Simulation results for the temperature variation across the radius billet during hot extrusion have been shown in fig 14. This temperature distribution across the radius has been plotted for after 2 secs. of extrusion at 815^{o}C, i.e at the start of extrusion. It shows the effect of ram speed on increase in surface temperature, which provides crucial in designing extrusion of product without surface defect and uniform microstructure from surface to centre.

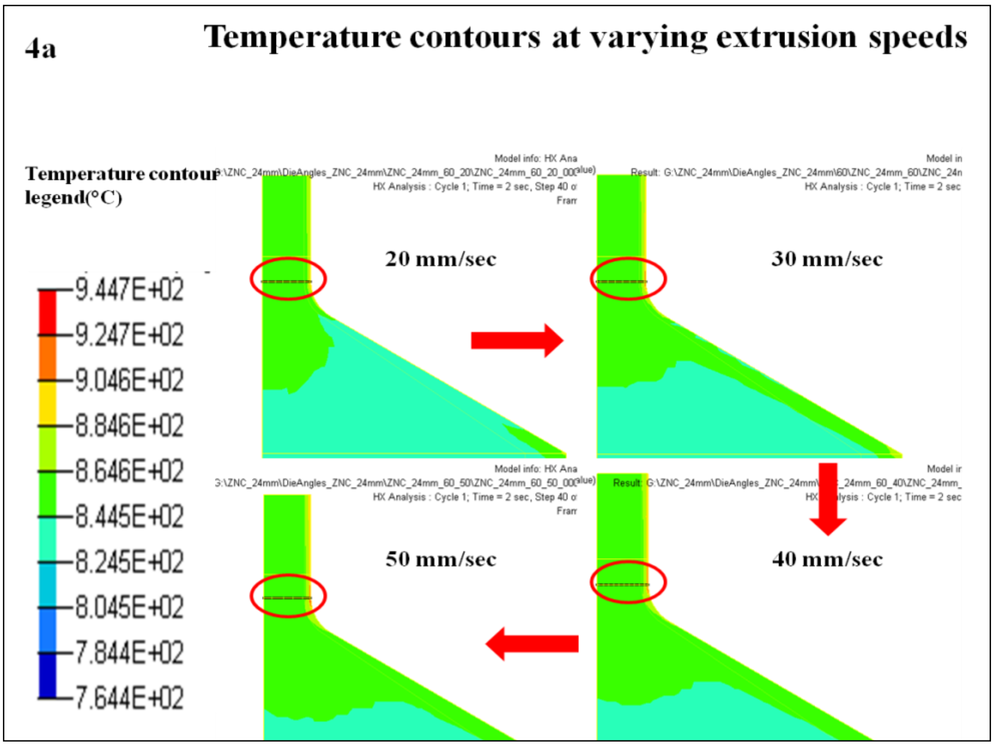

Fig. 14 Effect of ram speed on temperature distribution near die exit region.

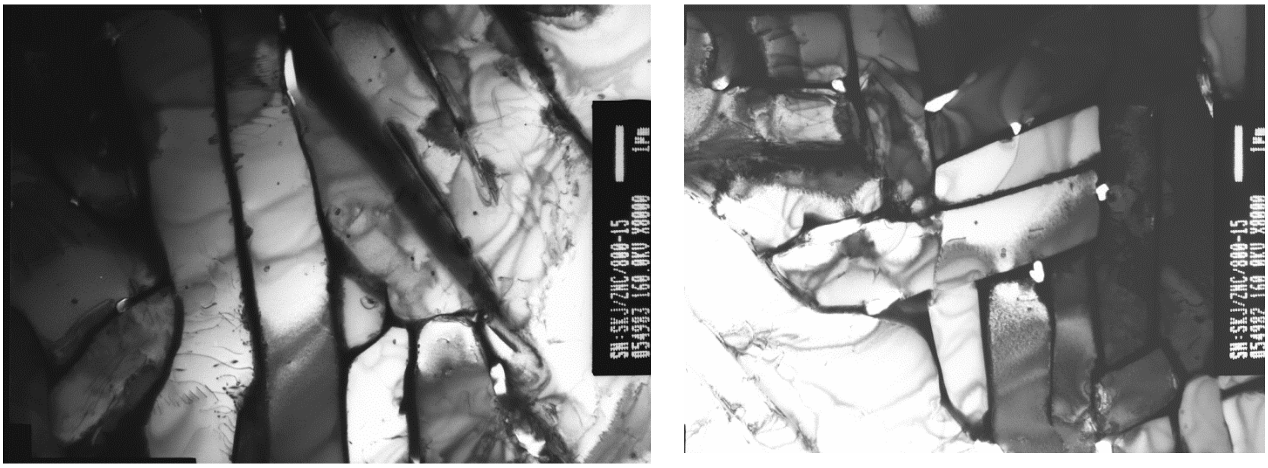

Fig. 15 Recrystallised microstructure of Zr-2.5Nb-0.5Cu deformed at 815^{0}C strain rate of 1 S^{-1}

Summary of results

1. In as cast dilute ZrSn alloy there is wide variation in flow stress and in low temperature region flow stress increases continuously with increase in strain rate and strain.

2. Processing maps developed for cast alloy has wide region of flow instabilities. One of the new information is Beta phase working of this material instead of a widmanstatten structure. It is possible to get fully recrystallised structure at strain rate of 10 $S^{-1}$and random alpha grain. This result has significant industrial applications since, at high temperature flow stress is extremely low therefore with less force and high rate of deformation it is possible to get fully recrystallized product.
3. First time constitutive equation for as cast alloy is developed and also validated for a bulk deformation process like extrusion.
4. Microstructure and micro texture of entire deformation range is reported in this work which explains in detail about the change in microstructure with deformation variables.
5. Dynamic recrystallization has occurred at 750° C and above, with the microstructure showing recrystallized grains and the flow curves displays no appreciable work hardening
6. At 900° C, the microstructure changed from the Widmanstatten structure of β to α transformation variant to equiaxed grains as the strain rate was increased. A high strain rate of 10 S^{-1} was found to be required to result in complete dynamic recrystallization, overriding the microstructural features of β → α phase transformation.
7. Co-extrusion parameters for Zircaloy-2 and ZrSn have been optimized first time and results from this work used for co-extrusion has matched the all predicted values. This work has potential application in duplex and also in triplex clad extrusion in future.
8. In this work simulation of Zr-2.5Nb-.5Cu has also been done and extrusion parameters have been optimized.
9. Results obtained from this work have significant application in bulk deformation processing of other alloys.

References

1. Kass, S., “ The Development of the Zircaloys.” Corrosion in Zirconium Alloys, STP368. American Society for testing of Materials, Philadelphia, 1964. P.3.
2. Rosenbaum, H.S., “The Interaction of Iodine with Zircaloy-2, “Electrochemical Technology, Vol.4, 1966, pp. 153-156.
3. Rosenbaum, H.S. Davies J.H., and Pon J.Q., “the Interaction of Iodine with Zircaloy-2, “General Electric company Report GEAP-5100-5, 1966.
4. Tomain, D. S., Adamson, R. B., and gangloff, R.P., “ Performance of Irradiated Copper and Zirconium Barrier Modified Zircaloy Cladding under simulated Pellet – Cladding Interaction Coditions,” Zirconium in the Nuclear Industry: Fourth International Symposium, ASTM STP 681, American Society for testing of Materials, Philadelphia, 1979. pp. 122-144.
5. Davies, J. H. , Rosenbaum, H. S., Armijo, J. S., Proebstle, R. A., Rowland, T. C., Thompson, J.R., Esch, E. L., Romeo, G., and Rutkin, D.R., “Irradiation Tests to Characterise the PCI Failure Mechanism, “ in Proceedings. ANS Topical Meeting on Water Reactor Fuel performance, American Nuclear Society, St. Charles, III., 1977, pp. 230-242
6. Rosenbaum, H. S., Davies, J. H., Adamson, R. B., Armijo, J.S., Rosicky, E., Wisner, S. B., Tucker, R. P., and Esch, E. L., “Resistance of Zirconium Barrier Fuel to Pellet-Cladding Interaction, “Transactions Of American Nuclear Society, Vol. 38, 1981, pp. 270-272.
7. Rosenbaum, H. S., Rand, R. A., Tucker, R. P., Cheng, B., Adamson, R. B.,
8. F. Ren, J. Chen, F. Chen, Constitutive modeling of hot deformation behavior of X20Cr13 martensitic stainless steel with strain effect, Trans. Nonferr. Metal. Soc. 24 (2014) 1407–1413.

9. Y.C. Lin, Y.C. Xia, X.M. Chen, M.S. Chen, Constitutive descriptions for hot compressed 2124-T851 aluminum alloy over a wide range of temperature and strain rate, Comp. Mater. Sci. 50 (2010) 227–233.

10. W. Li, H. Li, Z. Wang, Z. Zheng, Constitutive equations for high temperature flow stress prediction of Al–14Cu–7Ce alloy, Mater. Sci. Eng. A 528 (2011) 4098–4103.

11. H.L. Gegel, J.C. Malas, S.M. Doraievelu and V.A. Shende, in: Metals Handbook, Vol. 14 (American Society for Metals, Metals Park, Ohio 1987) p. 471.

12. J.K. Chakravartty, S. Banerjee, Y.V.R.K. Prasad, M.K. Asundi, J. Nucl. Mater. 187 (1992) 260.

13. R.A. Holt, J. Nucl. Mater. 35 (1970) 322.

14. Rosenbaum, H. S., Rand, R. A., Tucker, R. P., Cheng, B., Adamson, R. B.,

Davies, J. H., Armijo, J. S., and Wisner, S. B., "Zirconium-Barrier Cladding Attributes," *Zirconium in the Nuclear Industry: Seventh International Symposium, ASTM STP 939,* R. B. Adamson and L. F. P. Van Swam, Eds., American Society for Testing and Materials, Philadelphia, 1987, pp. 675-699

Publications in Referred Journals from This Work:

1. S. K. Jha, NachiketKeskar, Vishnu Narayan K, Mani Krishna, Dinesh Srivastava, Gautam K. Dey and Saibaba N. " Microstructural and textural evolution during hot deformation of dilute Zr-Sn alloy" , Journal of Nuclear Material

2. S.K. Jha*[1], Kumar Vaibhaw[1], V. Raizada[1] N. Saibaba[1] D. Srivastava[2] and G. K. Dey[2]"Thermo-Mechanical Simulation Of Hot Extrusion Process For Zr-2.5Nb-0.5Cu Alloy Garter Spring"

Manuscripts prepared for publication

1. Constitutive Modelling of Hot deformation incast Zirconium Sn Alloy

S K Jha*, Kumar Vaibhaw*, K Chetan*, M Ravindran*, D Srivastava#, N Saibaba*

2. Numerical Simulation and Modeling of Co-Extrusion of Zircaloy-2 and Zr-Sn Alloy for Double Clad Tube Manufacturing”

ACKNOWLEDGEMENTS

I express my sincere gratitude to Dr. Dinesh Srivastava, Dy. Chief Executive, NFC who has provided me valuable guidance not only in preparation of my thesis work but also in conducting analysis of experimental results. Dr. G. K. Dey has continuously inspired and encouraged me in doing this work. Dr. N. Saibaba has been kind enough in providing me necessary facilities to complete this project. Contribution made by Dr. R. N. Singh in preparation this manuscript has been noteworthy. Special thanks to Shri Nachiket without his continuous support this work wouldn't have been completed. I also thank Dr. Mani Krishna and Dr. Kulkarni from BARC for providing his valuable suggestions in completing this work. I also thank Shri Kumar Vaibhaw, ADM, EPP, NFC, Shri L. Sudarsanam, Manager(EPP), Shri Ch S. K. Charry, DM(EPP) for their valuable contribution in conducting experiments and supporting me in preparation of this manuscript. I would also like to mention the special contribution made by Shri Vishnu Narayan and K. Chetan in developing number of analytical models in obtaining the results. I am also thankful to Prof. I. Samajdar and his entire team in providing their laboratory facilities in conducting micro-structural analysis. In completing this thesis I cannot forget the contribution made by Dr. Saurabh Dixit, Manager (R&D) of MIDHANI.

I also thank my wife, Kalpana, daughter Priyanka and son Prateek who have supported and encouraged me to complete this project.

S. K. Jha

Acronyms

NFC	Nuclear Fuel Complex
EPP	Extrusion and Piercing Plant
FEM	Finite Element Method
ANN	Artificial Neural Network
ID	Inner Diameter
OD	Outer Diameter
WT	Wall Thickness
HDA	Half Die Angle
BC	Boundary condition
Inconel alloy	Superalloy 718
Ω	Current configuration bounded domain
Γ	Piecewise smooth boundary
Γ_u	Velocity specified boundary
Γ_t	Stress specified boundary
Γ_T	Temperature specified boundary
Γ_q	Heat flux specified boundary
n	Outward unit normal vector over Γ
∇	Gradient
u	Velocity vector
u_0	Initial velocity
σ	Total stress tensor
t	Time

T	Temperature
T_0	Initial temperature
ρ	Mass density
C_p	Specific heat of the fluid at constant pressure
q	Heat flux vector
h	Convective heat transfer coefficient
Φ	Internal heat generation rate due to viscous dissipation
τ	Viscous shear stress tensor
p	Pressure
I	Unit tensor
γ	Rate of Deformation tensor
η	Fluid Viscosity
k	Isotropic thermal conductivity
έ	Effective strain rate
λ	Penalty parameter
p^n	Pressure at n^{th} iteration.
V	Spaces of admissible velocities
H	Subspaces of solenoidal velocities
W	Space of admissible temperatures

Q	Space of admissible fluid pressures
$\int_{\Omega}$	Integration over domain Ω
$\parallel v \parallel$	Norm of space of admissible velocities
$\parallel w \parallel$	Norm of space of admissible temperatures
$\parallel q \parallel$	Norm of space of admissible fluid pressures

Index

List of Figures

Chapter 1

Introduction

1.1. Motivation and objective of this Study

To utilise the vast reserves of Thorium available in India it is proposed to use Thorium as fertile fuel alongwith Plutonium and Uranium ($_{92}U^{233}$) in Advanced Heavy Water Reactor (AHWR). AHWR is a 300MWe, heavy water moderated, boiling light water cooled natural circulation reactor. The fuel consists of $(Th–Pu)O_2$ and $(Th–_{92}U^{233})O_2$ pins. Ziracloy-2 will be used for Fuel clad as the reactor is of boiling water type where Zircaloy-2 has long history as clad tube [1]. Expected burnup of fuel in AHWR is likely to be more than 40000 MWD/T and to withstand the power ramp, there is need to improve the performance of clad tube.

Experiment conducted to show the effect of Iodine with Zircaloy, has confirmed that due to combined presence of Iodine vapour and stress between 300 to 400^{0}C, Zircaloy cracked [2,3]. Since, failure of clad took place due to presence of stress and corrosive fission gas it was identified as the process of stress corrosion cracking (SCC). Crucial factor in the cracking of fuel cladding is the concentrated stress at the inner surface of the fuel cladding during a power ramp. This takes place invariably due to expansion of pellet; therefore the process is called pellet clad interaction (PCI). To reduce the stress in clad tube inner surface of the tube was modified [4-6]. Two types of changes in clad tube were attempted which includes, the metallurgically bonded 75 µm thick zirconium layer and 10µm electrodeposited copper [4]. At low-burnup and power ramp tests, both barrier types were found successful. After conducting initial trial, millions of fuel pins with Zirconium lined Zircaloy-2 tube were irradiated in BWR which gave life of fuel clad tube for exposure at 43000MWD/T(bundle average). In case of pure Zirconium as liner, even small ingress of oxygen in the inner side of clad tube, catastrophic failure can take place during service [4]. Therefore, new concept in liner material is addition of about 0.3. % to 0.4.% Sn in Zirconium which results in improved corrosion resistance to large extent without sacrificing the ductility of the material which is requisite for controlling stress due to PCI. Experimental trials have shown [7] that metallurgical bond, uniform thickness of liner and desired chemical composition of the Zirconium barrier are essential requisite for double clad tube to provide PCI resistance. The Zirconium-barrier cladding tubes are manufactured by co-extrusion at elevated temperature to form a composite tube shell of Zircaloy with a liner of Zirconium, followed by co-reduction in a pilger mill in several passes with intermediate recrystallization anneals.

For two phase Zirconium based alloys Zr-2.5Nb-0.5Cu alloy used as garter spring has been selected to know its flow behavior and modeling of extrusion. Motivation for selecting garter spring is mainly due to its critical use in PHWR where it supports pressure tube both in initial condition and later after creep sag of the pressure tube should have adequate strength. Addition of small amount of Copper to Zr-2.5%Nb, which used as pressure tube material in PHWR, improves its strength by precipitation of Zr_2Cu on ageing the ternary martensite. Addition of copper also improves the corrosion properties of the garter spring. Although physical metallurgy and characterization of Zr-2.5 %Nb have been studied significantly, but the studies on Zr-2.5Nb-0.5Cu are rather limited. The properties of Zr-2.5Nb-0.5Cu alloy are very sensitive to the thermo mechanical fabrication steps including hot and cold working due to their anisotropic deformation behavior and presence of the intermetallic phase.The properties of Zr-2.5Nb-0.5Cu alloy are very sensitive to the thermo mechanical fabrication steps starting with hot extrusion followed by multiple working with intermediate annealing. In extrusion, correct design and control requires, among other things, the determination of the deformation mechanics involved in the process. Without the knowledge of the influence of variables such as friction process conditions, material properties and workpiece geometry on the process mechanics, it would not be possible to design the dies and the equipment adequately, or to predict and prevent the occurrence of defects.

1.2. Objective

Dilute ZrSn alloy being developed as liner for clad requires understanding of bulk deformation properties in as cast condition as well as in wrought conditions. During bulk deformation material experiences not only high temperature and high strain rate but also very high value of strain. Therefore, there is need to understand the effect of all these variables on microstructure and texture development under different set of conditions. In literature, data available on deformation of Zirconium as well as Zirconium with different percentage of Tin has been extensively considered for wrought material. And it has been established that the initial microstructure and texture plays dominant role in deformation of an alloy. Co-extrusion of Zr-Sn lined Zircaloy-2 tubes at elevated temperature requires optimization of extrusion parameters. Deformation behavior of liner material was studied using hot compression testing method at different temperatures and strain rates. Deformation mechanism for cast Zirconium Tin alloy with respect to micro-structural stability can be obtained by developing power dissipation maps with the concept of Dynamic Materials Model. Processing map needs to be developed using thermo-mechanical data generated using thermo-mechanical simulator. The map developed systematically can be used to know the influence of temperature and strain rate on the constitutive flow behavior of cast zirconium Tin alloy. Different region of processing maps needs to be validated with microstructure developed during deformation of cast Zr-Sn alloy. Further maps are useful for knowing the phenomena of bulk deformation process which can be utilized in industrial practice. For FEM based simulation and modeling of hot deformation process there is need of constitutive equation for an alloy. As deformation of as cast material is expected to be inhomogeneous, it becomes difficult to obtain a constitutive equation which is valid in entire range of deformation conditions. Although physical metallurgy and characterization of Zr-2.5 %Nb has been studied significantly, however the studies on Zr-2.5Nb-0.5Cu are rather limited. The properties of Zr-2.5Nb-0.5Cu alloy are very sensitive to the thermo mechanical fabrication steps including hot and cold working due to their anisotropic deformation behavior and presence of the intermetallic phase. The properties of Zr-2.5Nb-0.5Cu alloy are very sensitive to the thermo mechanical fabrication steps. In extrusion, correct design and control requires\, among other things, the determination of the deformation mechanics involved in the process. Without the knowledge of the influence of variables such as friction process conditions, material properties and workpiece geometry on the process mechanics, it would not be possible to design the dies and the equipment adequately, or to predict and prevent the occurrence of flow instabilities.

1.3. Structure of Thesis

In Chapter 2 extensive literature review on high temperature deformation behavior of Zirconium alloys have been discussed and also voluminous work carried out on Constitutive modeling for different materials has been summarized. An attempt is made to summarize the vast literature available in simulation of hot extrusion.

In chapter 3 experimental work starting from development of alloys to its processing and various experimental works has been covered in brief. Hot compressed samples under different set of temperatures and strain rates were studied to know the microstructure changes. Scanning Electron Microscope (SEM) based Electron Backscattered Diffraction (EBSD) was used to characterize the hot deformed microstructures. The bulk textures of the deformed samples were recorded using a PANalytical™ PRO-MRD XRD system. In chapter 4 microstructure and texture evolution during hot deformation of dilute Zr-Sn alloy has been covered extensively. A systematic study in knowing the micro structural and micro textural development is examined in wide range of deformation to get the complete insight into the type of deformation involved.

In chapter 5 deformation behaviour of the cast Zr - 0.3 Sn alloys with respect to micro-structural stability is explained using power dissipation maps generated on the basis of the Dynamic Materials Model. In order to simulate the material flow behaviour under specified conditions, constitutive equation correlating the flow stress, strain, strain rate and deformation temperature have been developed which has resulted in development of constitutive model.

Chapter 6 covers the Numerical Simulation and Modeling of Co-extrusion of Zircaloy-2 and Zr-0.3Sn alloys where material flow stress data obtained under uniaxial hot compression tests as a function of temperature and strain rate were taken as input. Optimization of Co-extrusion parameters in terms of ram speed, preheat temperature and semi die angles through numerical simulation was carried out over the fairly wide range.

In chapter 7 deformation of two phase Zr-2.5%Nb-0.5Cu alloy during hot working has been simulated. It has been demonstrated that the application of FEM in the extrusion process provides an excellent means of obtaining information about the material flow and using this information the desired geometry of tools can be achieved. Such objectives essentially consist of, a) establishing the kinematic relationships (velocities, strain-rates) between the deformed and unreformed part, i. e. predicting metal flow, b) establishing the limits of formability, i. e.

establishing, whether it is possible to form the extrudate without surface and\or internal defects and c) predicting the forces and stresses necessary to execute the process so that tooling and equipment can be designed or selected accordingly.

Outcome from the analysis carried out in this thesis has been in depth knowledge about microstructure development during deformation of a cast Zirconium alloys. Understanding its deformation behaviour has provided us the information that under bulk deformation stages it is possible to get fully recrystallised structure. Constitutive equation development of Zirconium alloys has been developed, which can be utilised for modelling of the deformation process. Co extrusion work for Zircaloy-2 and ZrSn alloy is quite useful work and has application in development of duplex tube. More information can be obtained from this work.

Chapter 8 presents the summary of the work carried out in this thesis and also future work which can be carried out using results obtained during the course of investigation.

1.4. References:

1. Kass, S., “ The Development of the Zircaloys.” Corrosion in Zirconium Alloys, STP368. American Society for testing of Materials, Philadelphia, 1964. P.3.
2. Rosenbaum, H.S., “The Interaction of Iodine with Zircaloy-2, “Electrochemical Technology, Vol.4, 1966, pp. 153-156.
3. Rosenbaum, H.S. Davies J.H., and Pon J.Q., “the Interaction of Iodine with Zircaloy-2, “General Electric company Report GEAP-5100-5, 1966.
4. Tomain, D. S., Adamson, R. B., and gangloff, R.P., “ Performance of Irradiated Copper and Zirconium Barrier Modified Zircaloy Cladding under simulated Pellet – Cladding Interaction Coditions,” Zirconium in the Nuclear Industry: Fourth International

Symposium, ASTM STP 681, American Society for testing of Materials, Philadelphia, 1979. pp. 122-144.

5. Davies, J. H. , Rosenbaum, H. S., Armijo, J. S., Proebstle, R. A., Rowland, T. C., Thompson, J.R., Esch, E. L., Romeo, G., and Rutkin, D.R., “Irradiation Tests to Characterise the PCI Failure Mechanism, “ in Proceedings. ANS Topical Meeting on Water Reactor Fuel performance, American Nuclear Society, St. Charles, III., 1977, pp. 230-242.
6. Rosenbaum, H. S., Davies, J. H., Adamson, R. B., Armijo, J.S., Rosicky, E., Wisner, S. B., Tucker, R. P., and Esch, E. L., “Resistance of Zirconium Barrier Fuel to Pellet-Cladding Interaction, “Transactions Of American Nuclear Society, Vol. 38, 1981, pp. 270-272.
7. Rosenbaum, H. S., Rand, R. A., Tucker, R. P., Cheng, B., Adamson, R. B., Davies, J. H., Armijo, J. S., and Wisner, S. B., "Zirconium-Barrier Cladding Attributes," *Zirconium in the Nuclear Industry: Seventh International Symposium, ASTM STP 939,* R. B. Adamson and L. F. P. Van Swam, Eds., American Society for Testing and Materials, Philadelphia, 1987, pp. 675-699

Chapter 2

Literature Review

2.1. Zirconium alloys as core structural material

Zirconium and its alloys are widely used as structural materials in nuclear reactors, because of their unique combination of good corrosion resistance in water near 300° C, good mechanical properties and low capture cross section for thermal neutrons [1]. These components are mainly used in the form of tubes of different size ranges for applications such as fuel sheathing, guide tubes/calandria tubes, and pressure tubes [2-3] . The alloying of zirconium for nuclear applications need that thermal neutron absorption cross-section of pure zirconium does not increase significantly. Therefore, only relatively small amounts of alloying elements are added. The alloying elements were added in zirconium alloys mainly to improve the corrosion behaviour in water[3-7]. For example tin is added to counteract the detrimental effect of Nitrogen on corrosion resistance. Addition of small amounts of iron, chromium and nickel found to improve the corrosion resistance of zirconium-tin alloys due to the formation of intermetallic second phase particles (SPPs). The size and distribution of the SPPs is strongly related to the corrosion resistance. The Zircaloys which contain about 1.5 wt% Sn and Fe, Ni, and O as alloying elements have two important derivatives; Zircaloy-2 and Zircaloy-4. Zircaloy-4 is a nickel-free variant of Zircaloy-2 with similar oxidation behaviour, but different level of affinity with hydrogen[4-5]. Zirconium-Niobium alloys showing better strength and improved corrosion resistance have been used for reactor components, the Zircaloys, are widely used in both pressurised water and boiling water reactors as fuel cladding materials In PHWRs, they are used as fuel cladding, calendria tube in the early stages[8], cold-worked Zircaloy-2 was used as pressure tube material in CANDU type reactors[9].

Russians were first to report that an alloy of zirconium containing 1-5% niobium has superior mechanical strength and adequate corrosion resistance in comparison to Zircaloys. Subsequently Zr-2.5%Nb alloy as a pressure tube material and the Zr-1.0%Nb as a fuel cladding material have been found to be suitable because of their high strengths at the operating temperature[10]. This permits the use of thinner components, reducing the loss of neutrons by parasitic absorption with an accompanying improvement in corrosion resistance. Since 1967 CANDU reactors started using cold-worked Zr-2.5Nb as pressure tube material and subsequently all such PHWR reactors were using this material as pressure tube due to its higher strength, creep and fracture strength [1,2,4]. It was reported that in comparison to cold-worked Zircaloy-2, cold-worked Zr-2.5Nb has extraordinarily low deuterium absorption and good corrosion resistance [2,5]. In the same study it was shown that the corrosion of Zr-2.5Nb tubes was about one-third of that in Zircaloy-2 under similar operating conditions, and the deuterium uptake was only 2%~4% of that measured for Zircaloy-2 [11]

2.2. Zircaloy as cladding material

Commercial light water reactor fuel is composed of uranium dioxide pellets in a sheath or cladding of Zirconium alloys. Zircaloy-2 and Zircaloy-4 were developed [12] in the early 1950s, havebeen used as standard fuel cladding materials for boiling water reactors (BWRs) and pressurized water reactors (PWRs), respectively. In evaluating the in reactor performance of fuel it was identified that Zircaloy claddingsare subjectedto a persistent failure mechanism known as fuel pellet cladding interaction(PCI). It has been also established that fuel failure due to PCI was directly related to sudden increase of fuel rod power after sustained operation at a lower power. The PCI mechanism indicates the involvementof simultaneous effects of stress on the cladding imposed by the expansion of the pellet and the release of fission products, some of which act as stress corrosion cracking agents. Subsequent studies and experimental trials has established that, Zircaloy is susceptible to cracking when exposed simultaneously to stress and the corrosive effects of certain fission products [13]. The susceptibility of Zircaloy cladding to stress corrosion cracking was verified by laboratory tests of irradiated tubing material [14] and in power ramp tests of irradiated fuel rods [15-17]. With number of experimental trials it was known that the reason of crack in fuel clad is mainly due to concentration in stress at the inner surface of the fuel cladding during a power ramp. The Zr-barrier cladding is designed to maintain this stress at a level so low that cracks cannot propagate through the cladding.

2.2.1. Essential requirement of Zirconium lined Zircaloy cladding tube

The necessity of PCI resistant fuel cladding has led to development of composite Zircaloy tubing with inner surface metal barriers selected to control one or more elements of the fracture mechanism. Number of inner surface metal barriers were attempted and finally Dilute Zr-Sn alloy liner were hypothesized which, in compared to Zircaloy, is more resistant to fission product embrittlement and also reduces the magnitude of either the local stress or strain concentrations developed during PCI. The essential features of the Zr-barrier fuel cladding which distinguish it from other fuel designs are (1) the metallurgical bond between the Zircaloy substrate and the zirconium liner (2) the liner thickness and (3) the softness of the liner [22].

2.2.2. Material properties of Zirconium alloys

The input material properties required for simulation include the thermal and physical properties and the deformation flow stress for the two alloys.

2.2.2.1. Thermal properties

Thermal conductivity

The thermal conductivity value for both the alloys is slightly different and those values are optimally taken from literature [31].

Thermal conductivity for Zircaloy-2 alloy was in the range of 0.13 to 0.2 in a temperature range of 300 to 900 K. It is assumed to be linearly varied in the present range. For temperatures more than the given limit will be extrapolated. The thermal conductivity values considered are shown table 2.1.

Table 2.1 Thermal conductivity values for Zr-2 alloy at different temperatures

Thermal conductivity, W/(m. K)	**Temperature, K**
0.13	300
0.14	400
0.15	500
0.16	600
0.17	700
0.19	800
0.2	900

(b) Specific Heat capacity

The heat capacity is the amount of heat required to raise the temperature of an object or substance by one degree centigrade or kelvin.

The recommended heat capacity values for Zircaloy-2 material as taken from literature is given table 2.2

Table 2.2 Specific heat capacity of Zr-2 alloy at different temperatures

Temparture, K	Heat Capacity, J/(kg K)	Temparture, K	Heat Capacity, J/(kg K)
273	283.6	1210	1416.6
300	286.4	1214	1438.3
400	296.6	1220	1335.1
500	306.9	1240	739.3
600	317.1	1260	385.2
700	327.3	1280	332.7
800	337.6	1300	330.2
900	347.8	1400	331.5
1000	358.1	1500	336
1100	368.3	1600	343.7
1120	370.4	1700	354.4
1140	372.9	1800	368.3
1160	393.3	1900	385.3
1180	592.3	2000	405.5
1200	1190		

The heat capacity values for Zirconium alloy are ranging in between 0.3 to 0.35 in a temperature range of 300 to 900 K. It is assumed to be linearly varied in the present range. For temperatures more than the given limit will be extrapolated. The specific heat values used for simulation is shown in table 2.3.

Table 2.3 Specific heat capacity of Zr-Sn at different temperatures

Heat capacity, J/(g K)	**Temperature, K**
0.3	300

0.308333	400
0.316667	500
0.325	600
0.333333	700
0.341667	800
0.35	900

2.2.3. Mode of Deformation in Zirconium Alloys

Plastic deformation of hexagonal crystal structured alloys is usually characterized by the activation of a variety of slip and twinning systems. The operation of those systems strongly depends on the c/a ratio [19]. For zirconium with a c/a ratio of around 1.59, the easiest slip system $\{10\bar{1}0\}$ $\langle 11\bar{2}0\rangle$ prismatic <a> slip, followed by (0002) $\langle 1120\rangle$ basal <a> slip, and $\{10\bar{1}1\}$ $\langle 11\bar{2}3\rangle$pyramidal <c+a> slip which is the hardest mode [20-22]. Different types of twinning are also often found to operate in order to provide sufficient deformation modes to meet the von Mises criteria. At high temperatures deformation in Zirconium alloys takes place due to prismatic slip, which is believed to be the easiest slip mode at all temperatures and also basal slip which is activated in ease with increasing temperature.

2.2.3.1. High temperature deformation

High temperature deformation is known to be a process wherein large amount of deformation occurs due to dynamic recovery and or recrystallisation at high temperatures and strain rate. The temperature range where such processes occur is estimated [23] as being above ~0.5Tm (Where Tm is the absolute melting temperature). The lower limit of this range will also depend on the strain rate and the material being considered [24]. In this temperature range the dislocation substructures formed are superficially similar to the cell-like dislocation tangles produced by cold work [25]. They are, however, more perfect and contain fewer redundant dislocations because of the thermally activated restoration processes, such as cross-slip and climb, which are operative at these temperatures [26-27]. At high temperatures most materials undergo an initial stage of transient deformation which eventually leads to a “unsteady state”, in which work hardening is balanced by recovery. In creep tests (constant stress) this appears as secondary creep, where as in constant strain rate tests it appears as a regime of steady state flow stress. It is now evident that the steady state mechanical and structural properties, whether determined under constant strain rate or creep conditions, are equivalent [28]. Therefore, as long as only steady state conditions are considered, there is no need to distinguish between the two deformations modes.

2.2.3.2. Mechanism of Deformation

At high temperatures most of the materials undergo an initial stage of transient deformation which eventually leads to a “steady state”, in which work hardening is balanced by recovery. As long as only steady state conditions are considered, there is no need to distinguish between the two deformations modes. Therefore, to understand the behavior of metal flow majority of work have been carried out under creep conditions where, the stress is maintained constant and the strain is measured as a function of time. On application of the stress, an “instantaneous” strain is observed which is followed by a transient region (primary creep) in which the strain rate continually decreases with time (strain). The Extent of primary creep depends on the temperature and stress as well as on the material considered. The transient region is followed by a steady state region where the strain rate remains constant until tertiary creep, associated with localized necking and cavitations, begins. The emphasis in creep studies has been on deformation at relatively low stresses and therefore low strain rates (less than $10^{-3}S^{-1}$). Also, as tests are usually carried out in tension, they have been restricted to low strains (less than 0.5). These studies are only useful mainly to study the mechanism of deformation but are of limited significance in case of bulk deformation. So, need for understanding the high rate of deformation under hot working conditions ($\varepsilon=10^{-2}S^{-1}$ to $10^{3}S^{-1}$) has led to the use of hot compression and hot torsion testing where high amount of strain rate can be given for reasonably high strain. Data thus generated is being used to develop number of deformation related information such as deformation maps, constitutive equations, activation energies and material specific constants etc.

2.3. Deformation Maps

A material can be deformed according to several deformation mechanisms. In a certain interval of temperatures and strain rates, one deformation mechanisms will prevail. All of them work at the same time and the faster one can usually control the flow behaviour. A way to determine the process that occurs during the deformation is the use of deformation maps .

2.3.1. Ashby-Frost Deformation Maps

Each deformation mechanism can be described by an equation that relates the shear strain rate, the shear stress, the absolute temperature and the microstructure. Ashby and Frost designed deformation maps that depicted the normalized stress multiplied for the shear modulus opposite of homologues temperature ($T/T_{melting}$) pointing out in each strain rate, which was the active mechanism. These maps provide information about the deformation mechanism that is expected to be found in conditions of a thermodynamic process at strain rates smaller than 10^{-3} s-1 [29]

2.3.2. Raj Deformation Maps

Raj [19] extended the concept of the deformation maps considering two important mechanisms of damage that are relevant to the deformation. One is the cavities formation at hard particles in a soft matrix. These particles do not deform but localization strain occurs at the surrounding matrix which can lead to pore formation. This mechanism occurs at lower temperatures and higher strain rates.

When the temperature is high, the velocity of the cavities formation is slow because of the low hardness speed due to recovery. Thereby, Raj [30] established the minimum conditions (combination of temperature and strain rate) for the cavities formation near the hard particles.

The second damage mechanism is the triple junction cracking, the crack is formed at in the grain boundary to decrease the stress concentration due to the gliding of the grains boundaries at high temperatures and low strain rates.

Additionally, when the strain rates are high, flow localization can take place by local increment of the temperature due to adiabatic flow behaviour.

2.3.3. Manufacturing of Zirconium lined Zircaloy cladding

The Zr-barrier cladding tubes are manufactured by co-extrusion at elevated temperature to form a composite tube shell of Zircaloy with a liner of Zirconium, followed by co-reduction in a pilger mill in several passes with intermediate recrystallization anneals. Thus the interface is identified solely by a change in chemical composition from that of Zirconium to that of Zircaloy, therefore no physical interface exists. There is no oxide, no surface, and no grain boundary; there is nothing to interrupt the atomic continuity between the Zirconium liner and the Zircaloy portion of the cladding. It is the cohesion between Zirconium atoms in the alpha zirconium phase, indeed within the same crystals, which determines the strength of the bond.

2.3.4. Dynamic Modeling of the Material Behaviour

The basic notions for the construction of the power dissipation maps is the dynamic materials model (DMM) developed by Prasad et al. [31] In this model, the workpiece formed at high temperature is considered as the only part of the whole system of the process that is able to dissipate energy. The constitutive equation is an empirical relation that describes the flow stress change with the deformation parameters. For a given temperature and strain rate, it is assumed that the constitutive dynamic equation follows a potential law where at constant temperature and strain, the dynamic response of the workpiece material undergoing hot deformation is represented by the constitutive equation

$$\sigma = K\dot{\epsilon}^{m} \qquad 2.1$$

where K = constant and m = strain rate sensitivity of flow stress given by

$$m = \partial(\ln\sigma)/\partial(\ln\dot{\epsilon})$$

Fig. 2.1, the rectangle formed by σ versus $\dot{\epsilon}$ plot gives the total power dissipated instantaneously by the workpiece and manifests as a temperature rise in the material and a change in the internal energy of the material through a change in the microstructure. The dynamic constitutive equation (Eq.2.1) decides how the power is partitioned between these two manifestations. The total power (P) may be represented as a sum of two complementary functions

$$P = \sigma.\dot{\varepsilon} = \int_0^{\dot{\varepsilon}} \sigma d\dot{\varepsilon} + \int_0^{\sigma} \dot{\varepsilon}\, d\sigma \qquad 2.2$$

In systems modeling terminology, the first integral is called G content and the second one J co-content which is a complementary function of G content. As per Eq. (2.3), G content represents the area under the dynamic constitutive equation curve and J co-content represents the area above it.

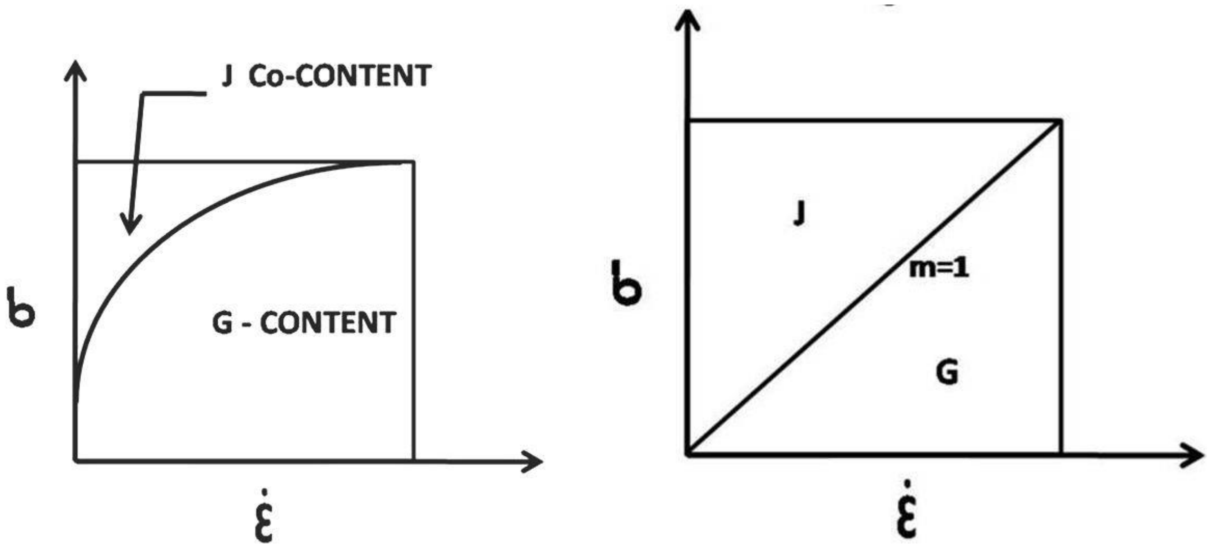

Fig 2.1. σ Vs ε· plot (a) Viscoplastic solid following power law behaviour and (b) an ideal linear power dissipator at constant temperature and strain.

The factor that partitions power between these two complementary parameters is the strain rate sensitivity of flow stress (m), since

$$\frac{dJ}{dG} = \frac{\varepsilon^{\cdot} d\sigma}{\sigma\, d\varepsilon^{\cdot}} = \frac{\varepsilon^{\cdot}\, d\ln\sigma}{\sigma\varepsilon^{\cdot} d\ln\varepsilon^{\cdot}} \approx \frac{\Delta\log\sigma}{\Delta\log\varepsilon^{\cdot}} \equiv m \qquad 2.3$$

In the dynamic materials model, special significance is attached to the physical interpretation of power partitioning using strain rate sensitivity. Partition of energy applied to the energy dissipater depends on the strain rate sensitivity m and its value depends mainly on constitutive behavior of the material.

For understanding the physical sense of G and J, the microscopic process of plastic deformation should be considered. Plastic flow occurs for crystallographic sliding, that results of the dislocation motions in their slide planes undergoing a shear stress(τ). The τ action increases the kinetic and potential energy. A big part of the potential energy is almost instantly transformed in kinetic energy. However the kinetic energy provided by the plastic flow is transformed into heat. The most of these transformations is dissipated by heat and it is represented by the dissipator G and the rest of the energy is stored like faults.

Other microscopic processes which annihilate dislocations and dissipate energy can exist as well. All of these metallurgical phenomena contribute to the energy dissipation but in a lower proportion than the power dissipator content, and they represent the complementary function, J the dissipator co-content. The conclusion is that at either instant the energy dissipation occurs through heat (the dissipator content, G) or structural changes (the dissipator co-content J).

The efficiency of power dissipation(η) is given by

$$\eta = {}^{J}/_{J_{max}} = {}^{2m}/_{(m+1)} \qquad 2.4$$

$\eta$is then calculated and plotted as a contour map in a frame of temperature and strain rate. The variation of efficiency of power dissipation with temperature and strain rate constitutes a power dissipation map, which exhibits various domains in which specific microstructure mechanisms occur.

2.3.4.1. Continuum Instability Criterion

Ziegler has shown that the condition for the plastic flow to become unstable is given by [32]

$$\frac{dD}{d\dot{\varepsilon}} < \frac{D}{\dot{\varepsilon}} \qquad 2.5$$

Where, D is the dissipative function that is characteristic of the constitutive behavior of the material and is given by the dissipated power. If the power is separated into two parts G and J, D may be replaced with J and we get a condition for flow instabilities that are microstructure related, as

$$\xi(\dot{\varepsilon}) = \frac{\partial \ln[^{m}/_{(m+1)}]}{\partial \ln\dot{\varepsilon}} + m < 0 \qquad 2.6$$

The parameter $\xi(\dot{\varepsilon})$may be plotted as a function of temperature and strain rate and the regime where it is negative will give flow instabilities. Such a plot is called an instability map. The above instability criterion has the physical meaning that if the system is not able to generate entropy at a rate that at least matches with the imposed rate, the system will localize the flow and cause flow instability.

2.4. Hot Deformation of Zirconium Alloys

Hot compression of α-Zr and a series of Zr-Sn solid solution temperature between 625 to 825°C and strain rates of 10-4 to 3 X 10^{-1} sec^{-1} were carried out study the development of substructure formation and its effect on mechanical properties mainly useful for creep studies[33]. Jonas and co-worker have conducted deformation at low strain rate and concluded that Addition of Sn in Zirconium retards dynamic recovery and also imparts strength to substructure. Deformation mechanism were discussed in detail by generation of deformation data for ZrSn in which tests were carried out between 625° and 925°C at strain rates of 10^{-4} and $1S^{-1}$ by M.J. Luton et al [34]. They concluded that empirical power law operates at the higher temperatures and lower strain rates and power law breaks down at lower temperatures and higher strain rates, which leads to athermal deformation[31]. Charavarty et al. [35-38] have done hot compression testing on number of Zirconium alloys in wide range of temperature and strain rates 650-1050°C and 0.001-100 s^{-1} respectively. Using power dissipation maps generated on the basis of the Dynamic Materials Model they systematically explained the influence of temperature and strain rate on the constitutive flow behavior of different zirconium alloys during hot-working and identified the different metallurgical processes occurring in the various temperature –strain rate regimes. Most of the samples utilised for their studies were homogenised wrought structures. Hot compression testing in temperature range of 625 to 825°C for α-Zr and a series of Zr-Sn solid solution alloys using strain rates of 10^{-4} to 3 X 10^{-1} sec^{-1}shows development of substructures. Over the subgrain size range 0.3 to 7, μm, the high temperature flow stress and subgrain size were inversely related. The increase in flow stress due to substructure formation also obeyed this type of relation. The results are consistent with a glide model of deformation in which the build-up of internal stress is due to the substructure developed by the deformation. The Tin (Sn) additions retard dynamic recovery. The mean size of the subgrains and the perfection of the subboundaries both decrease with decreasing temperature, increasing strain rate, and increasing Sn content. There have been many studies on the high temperature deformation behavior of zirconium and Zirconium-based alloys [24-28] which led to the evaluation of deformation mechanisms. Mehrotra and Tangri [33] studied high temperature thermally activated deformation behaviour of α-zircaloy-4 containing oxygen, with a view to elucidating the rate controlling mechanism which is identified as thermally-activated breaking of attractive junctions leading to softening by dynamic recovery. Chakaravarthy and Prasad et al have done extensive studies in knowing the hot deformation behaviour of Zirconium alloys in wide domain of temperatures and strain rates. But deformation samples used were mostly from wrought and finished products. Therefore, majority of the investigations carried so far have considered the fundamental aspects of deformation behaviour but optimization of hot workability has not received adequate attention.

2.5. Background on constitutive Equations

Constitutive equations describe relationship among stress, strain rate, and deformation temperatures. It helps to calculate expected load and power required for the forming processes and also suggest material flow behaviour along with the kinetics of metallurgical transformations[39]. Thus, it is necessary to develop accurate constitutive equation for a given material. The constitutive equations are classified into three different categories empirical, phenomenological and analytical. Various constitutive models such as Garofalo equation, Arrhenius type model with or without strain compensation, Johnson Cook (JC) model, Zerilli–Armstrong (ZA) model, Modified-ZA model and artificial neural network (ANN) were developed to predict constitutive behaviour for variety of metals and alloys by various researchers [39-53]. Sellars and Tegart[54] and Jonas et al. [55] have proposed a phenomenological approach, in which flow stress is related to strain rate by sine-hyperbolic law in an Arrhenius type equation. Extensive work on constitutive analysis of hot deformation for different metals and alloys was reported by McQueen [56], McQueen and Ryan[56], Cingara and McQueen [41, 42], Phaniraj et al. [57] and Samantaray et al. [58,60]. Flow stress of a material depends upon both strain rate and temperature which can be combined in a single parameter, Zener-Hollomon parameter(Z) [59].

2.5.1. Establishment of constitutive equations

Development of the constitutive equation allows extrapolation of stress data beyond the test window. Arrhenius type equations were proposed to relate flow stress with strain rate and temperature.

2.5.1.1. Arrhenius-type constitutive equation

Usually all materials exhibit increase in flow stress with increase in strain rate and decrease in temperature. Flow stress behaviour depends on rate of generation of defects and their removal by thermally activated processes. Zener and Hollomon[59] proposed a single parameter (Z) to express stress as a function of strain rate and temperature. Zener-Hollomon parameter (Z) can be defined in terms of temperature (T) and strain rate $(\dot{\varepsilon})$, as $Z = \dot{\varepsilon} \exp(Q/RT)$ [61]

In Arrhenius equation, the strain rate is a common parameter to relate the deformation temperature and activation energy. Thus strain rate is generally expressed by one of the three different types of equations the power law (Eq. 2.1), the exponential law (Eq. 2.7) and sine-hyperbolic law (Eq. 2.9). Applicability of each equation depends upon the stress value. It is reported that the power law equation is valid for low stress values, i.e. $\alpha\sigma < 0.8$, (Eq. 2.7), whereas the exponential law equation is valid at high stress values, i.e. $\alpha\sigma > 1.2$ (Eq. 2.8). But sine-hyperbolic law equation (Eq. 2.9) is valid for a wider range of flow stresses and more commonly in use [41,49, 51,54, 58]. $\alpha\sigma$ is called stress exponent factor.

$$\dot{\varepsilon} = A_1 \sigma^{n'} \exp\left(-\frac{Q}{RT}\right) \tag{2.7}$$

$$\dot{\varepsilon} = A_2 \exp(\beta\sigma) \exp\left(-\frac{Q}{RT}\right) \tag{2.8}$$

$$Z = \dot{\varepsilon} \exp\left(\frac{Q}{RT}\right) = A[\sinh(\alpha\sigma)]^n \tag{2.9}$$

whereas *A*, A_1, A_2, *n*, *n'* are material constants, *Q* is the activation energy for hot deformation (kJ/mol), R is the universal gas constant (8.314J mol^{-1} K^{-1}) and *T* is the absolute temperature (K).

For the development of constitutive equation flow stress cannot be defined uniquely for a given strain rate and temperature condition. Therefore in available literature on hot deformation, either peak stress (strain can vary) or stress value at a constant strain is considered for development of constitutive equation. Stress values other than peak stress may vary due to thermally activated softening mechanisms and may not be obtained accurately [50]. Thus, it is better to use peak stress values to determine constitutive equation [40, 57]. Also, peak stress is uniquely related to Zener-Hollomon parameter *(Z)*, for the entire range of deformation conditions [62]. Additionally, peak stress is more important for industrial processes [63, 64]. In this study, peak flow stress was considered to develop sine-hyperbolic law equation.

2.5.1.2. Identification of material parameters

The sine-hyperbolic law constitutive equation (Eq. 2.10), requires the determination of few material constants i.eA, n, α and Q. These material constants can be obtained as follows.

2.5.1.3. Determination of α value

The value of α can be calculated by $\alpha\left(\approx \beta/n'\right)$ [36], where n' and β can be calculated from Eqs. 2.2 and2.3.Taking natural logarithm on both sides of Eqs.2.7 and 2.8 yields Eqs.2.10 and 2.11, respectively.

$$\ln \dot{\varepsilon} = \ln A_1 + n' \ln \sigma_p - \frac{Q}{R}(1/T) \qquad (2.10)$$

$$\ln \dot{\varepsilon} = \ln A_2 + \beta \sigma_p - \frac{Q}{R}(1/T) \qquad (2.11)$$

The partial differentiation of Eqs. 2.10 and 2.11 with respect to peak flow stress (σ_p) at constant temperature yield

$$n' = \left[\frac{\partial \ln \dot{\varepsilon}}{\partial \ln \sigma_p} \right]_T \tag{2.12}$$

$$\beta = \left[\frac{\partial \ln \dot{\varepsilon}}{\partial \sigma_p} \right]_T \tag{2.13}$$

Where constant β and n' can be calculated using linear regression of the σ_p *vs* $\ln \dot{\varepsilon}$ plot and the plot of $\ln \sigma_p$ *vs* $\ln \dot{\varepsilon}$ respectively at each temperature as shown in Figs. 5 a and b. The final value of parameter n' and β are their average value calculated from the slope obtained at each temperature.

2.5.1.4. Determination of *n*

Using Eq.2.11, *n* value can be calculated. Simplification of Eq. 2.4 using natural logarithm on both sides yields Eq. 2.14. Partial differentiation of Eq. 2.14 with respect to peak flow stress at constant temperature results in Eq. 2.15

$$\ln \dot{\varepsilon} = \ln A + n \ln[\sinh(\alpha\sigma_p)] - \frac{Q}{RT} \tag{2.14}$$

$$\left[\frac{\partial \ln \dot{\varepsilon}}{\partial \ln\left[\sinh\left(\alpha\sigma_p\right)\right]} \right]_T = n \tag{2.15}$$

The relationship of $\ln\left[\sinh\left(\alpha\sigma_p\right)\right] - \ln \dot{\varepsilon}$ is plotted in Fig 2.6a at constant temperature. Thereafter, the final *n* value is an average value and summarised in Table 2.1.

2.5.1.5. Determination of the activation energy (Q)

For high temperature deformation, activation energy *(Q)* can be obtained by rearranging Eq. 2.14 as follows

$$\ln\left[\sinh\left(\alpha\sigma_p\right)\right]=\frac{Q}{nR}\frac{1}{T}+\frac{1}{n}\ln\dot{\varepsilon}-\frac{1}{n}\ln A \qquad (2.16)$$

The partial differentiation of Eq. 2.14 at constant strain rate with respect to the reciprocal of deformation temperature *(1/T)* yield Eq. 2.17

$$\left[\frac{\partial\ln\{\sinh(\alpha\sigma)\}}{\partial\left(1/T\right)}\right]_{\dot{\varepsilon}}=\frac{Q}{nR} \qquad (2.17)$$

Therefore the activation energy can be defined as follows

$$Q=R\,n\,s \qquad (2.18)$$

where $s=\left[\frac{\partial\ln\{\sinh(\alpha\sigma)\}}{\partial\left(1/T\right)}\right]_{\dot{\varepsilon}}$

which is determined by linear regression of the *(1000/T)*vs $\ln\left[\sinh(\alpha\sigma_p)\right]$ plots at constant strain rate. Afterwards the final value of *s*can be an average of *s* obtained at different strain rates. By using average value of *n* and *s* in Eq. 2.18, final activation energy can be calculated.

2.5.1.6. Determination of A

The linear regression of the $\ln\dot{\varepsilon}$ *vs* $\ln[\sinh(\alpha\sigma_p)]$ plots from Eq. 2.14 at each temperature can provide the intercept value to calculate constant *A,* as shown inFig.*6a***.** Furthermore *A* can be calculated by following equations.

$$\left(\ln\dot{\varepsilon}-\mathrm{int}\,erception\right)=\ln A-\frac{Q}{RT} \qquad (2.19)$$

Simplifying Eq. (2.19) yield to Eq. (2.20)

$$A=\exp\left[\left(\ln\dot{\varepsilon}-\mathrm{int}\,erception\right)+\frac{Q}{RT}\right] \qquad (2.20)$$

Since the value of Q is already obtained. Value of A can be determined using the intercept of linear regression of the $\ln \dot{\varepsilon}$ *vs* $\ln[\sinh(\alpha\sigma_p)]$ plot at each temperature.

2.6. Modeling and simulation of Hot Deformation

The importance of modeling and simulation in the metal forming industry has increased heavily during the last decades. Process simulation using the finite element method (FEM) is now accepted as an important tool for product and process development. However, the introduction of computer simulation in extrusion technology has not been as fast as in other parts of the manufacturing industry. This is mainly due to the very large deformations which make these simulations technically challenging and computer intensive. The simulation of hot extrusion processes is clearly one of the most difficult problem in process modeling [65].

Nevertheless, the potential of using numerical methods for analysis of extrusion is large. The whole process, including the important initial non-steady state of extrusion, can be analyzed. The evolution of, for example, stress, strain rates and temperatures in the material during the process can be studied in detail. As the capacity of computing hardware and software is increasing, it is no doubt that the FEM will be a tool of great use for development and optimization of extrusion . In the aluminium industry, on the other hand, extensive activities have been devoted to modeling and simulation, and in the recent years great progress has been made in this area. Simulation of magnesium extrusion has also been reported [66].

2.6.1. Different types of finite element methods

There are mainly three different types of FE methods that are utilized in extrusion simulation. Lagrangian, Eulerian and Arbitrary Lagrangian Eulerian (ALE). In recent years, promising results have also been shown with various meshless methods. The appropriate approach is determined by the problem to be solved and to some extent on the computer resources available [66].

In Lagrangian FE codes, the mesh moves with the material and deforms with the material flow. The quadrature points also move with the material which means that the constitutive equations are evaluated at the same material points through the whole analysis [65]. This approach is very useful for extrusion analyses, since the thermo-mechanical history during the process can be studied directly and the free surface of the extrudate can be followed.

The limitations of the Lagrangian description appear when the deformations are large. Large strains and deformations lead to excessive distortion of the elements which implies bad, or non-converging solutions. If the mesh is distorted, mesh refinement or remeshing is often required to obtain a solution. When remeshing is utilized, a new mesh is constructed and a mapping is performed to transfer data from the deformed mesh to the new mesh. In many commercial software packages, the remeshing technique has been automatized and can be controlled based on user defined criteria. Every remeshing involves interpolation and extrapolation of element variables which may accumulate errors in the solution. Remeshing is also a computer intensive step and reduces the computational efficiency. If it is possible, frequent remeshing should, therefore, be avoided. Additional problems often appear with meshing and remeshing in structural parts of small dimensions and/or in three-dimensional simulations.

An alternative to the Lagrangian approach is the Eulerian formulation, where the nodes and elements are fixed in space and the material flows through the mesh. The Eulerian method has a wide field of application in fluid mechanics but it is also suitable for many extrusion problems [66].

For instance, the material flow and temperature evolution in the container and through the die can be effectively studied using an Eulerian FE code. The major advantage of this formulation is that the problem with mesh distortion is avoided and large deformations can be simulated with a low computational cost. It is, however, difficult to model the free surface of the extrudate after it has left the die. Another drawback is that the treatment of constitutive equations is complicated due to flow of material through the elements [65].

The ALE methods are arbitrary combinations of the Lagrangian and Eulerian formulations and were developed in an attempt to bring the advantages with both formulations together. In an ALE formulation the displacements of material and mesh are decoupled and the mesh can move independently of the material. Thus, both the motion of the mesh and the material must be described. The ALE formulation was originally developed for modeling of fluid-structure interaction and motion of free surfaces in fluid mechanics [66]. A couple of years later the method was introduced for metal forming applications. Mesh distortion can generally be avoided using an ALE approach, but in practice it is difficult for the user to choose a mesh motion that eliminates severe mesh distortions. The ALE formulation in metal forming together with practical applications was presented in the work by Gadala and Wang [67]. The punch indentation process and metal extrusion process were simulated.

The capabilities of meshless methods in the simulation of forming processes have recently been investigated by several researchers. In contrast to the traditional mesh-based FEM, the meshless or meshfree methods use the geometry of the simulated object direct for calculations. The advantage with meshless methods over the Lagrangian FEM is that no remeshing is required. The capacity to simulate creation of free surfaces is improved compared to the Eulerian and ALE methods. There are a number of numerical methods that fall within this class of methods. Among these, the smoothed particle hydrodynamics method

(SPH), the element-free Galerkin method (EFG/EFGM) and the natural element method (NEM) have been applied to metal forming applications. The extrusion process has been simulated using NEM by Filice et al [68] and Alfaro et al [69,70]. Application of the SPH method to forging and extrusion was performed in the work by Cleary et al [71]. However, the state of development in meshless methods is much lower than in FEM and they are, so far, only implemented in a few commercial codes [69]. At the current state, meshless methods are mainly for academic use [66].

2.6.2. Element considerations

There are a variety of different element types available for finite element analysis and many of these are implemented in commercial programs. The choice of elements for an extrusion simulation is, however, much more limited. These elements must be applicable for use with remeshing and perform well for plasticity problems.

The elements that are most frequently used are the 3-node triangle and the 4-node quadrilateral in two dimensions, and the 4-node tetrahedron and the 8-node hexahedron in three dimensions. The 4-node quadrilaterals and 8- node hexahedron are generally more accurate than 3-node triangles and 4-node tetrahedral [71]. On the other hand, the triangular and tetrahedral elements have the advantage of being easier to mesh. This is especially important to consider when automatic mesh generators are used [66].

Besides the remeshing, which can be very troublesome, the particular problems with finite elements for extrusion are over-stiff behavior and volumetric locking. The plastic behavior of a von Mises elastic-plastic material is incompressible, which means that the volume is unchanged during deformation and the density remains constant. When low-order elements are utilized for incompressible materials, they tend to lock volumetrically [71]. When locking occurs, the finite element method cannot provide a good solution to the problem and at the same time satisfy the incompressibility condition. All the elements described above can suffer from volumetric locking. There are, however, ways to deal with the problem of locking and the most common way is to utilize different types of reduced integrations .

Three-dimensional simulations Simulation of extrusion in three dimensions is a challenge, mainly due to issues related to the remeshing. The three-dimensional simulations that have been carried out are often restricted to simple shapes and utilize symmetry. Extrusion often involves thin-walled sections which are difficult to mesh and lead to a large number of elements in the problem. This in turn means long computation times. Three-dimensional simulations of forging were carried out in the work by Lee et al [72]. The forging process has a lot in common with the extrusion process, and deals with the same remeshing problems. Traditional tetrahedral and hexahedral elements, assisted by the reduced integration scheme, and tetrahedral MINI-elements were evaluated by Lee et al [71] for two different forging cases. The standard tetrahedral element constrained too much of the metal flow for the solution to be realistic, while the tetrahedral MINI-element and the hexahedral elements predicted nearly the same result .

Hasan [74] studied three-dimensional simulation of extrusion with hexahedral and tetrahedral elements. The tetrahedrons however showed a stiff behavior and the extrusion force was heavily overestimated by these elements whereas hexahedral elements have shown reasonably good results hence hexahedral element showed potential for use in the extrusion technology.

2.7. Reported extrusion modeling survey in literature

Rout et al [73] presented a study on FEM modeling of extrusion of square section from square billet through bezier, polynomial and cosine shaped die, design of non-linear converging die profiles for extrusion from round billet to triangular and square sections, FEM modeling of triangular and square section from round billet through curved dies , followed by partial validation of experiment. Su-Hai Hsiang and Chao-Shun Liao [74] developed a numerical simulation model for forward hot extrusion processes of tube by combining the upper bound method with finite difference method. Effect of ram speed and extrusion temperature over ram force was studied by this model. L.X. Lia [75] has studied hot extrusion of Ti–6Al–4V alloy using finite element simulation and the results were compared with those obtained experimentally. In this study distribution of strain, temperature and effective stress was simulated under different design and processing conditions. F. Parvizian [76] investigated the thermo-mechanical behavior of aluminium alloys of 6000 series (Al Mg Si) and 7000 series (Al Zn Mg) during the extrusion process. The necessity of using the adaptive remeshing method to overcome element distortion and ensure proper contact modelling was shown. Moreover the influence of the friction, heat flux between the contacted surfaces and dissipated inelastic energy on the thermo-mechanical behavior of the workpiece during the simulation process was shown.

Zhou et al [77] made an attempt to predict the temperature evolution during the extrusion of 7075 aluminium alloy by means of 3D FEM computer simulation. Results show that ram speed has a significant influence on the temperature distribution in the billet, which continuously changes throughout the process, as a result of complex heat generation and heat loss. The results confirm the linear relationship between the increase of the maximum temperature and logarithmic ram speed during the steady-state extrusion. Liu et al [78] presented 3D computer simulations of extruding a wrought magnesium alloy AZ31 into a rectangular section at various ram speeds were performed and the results verified in extrusion experiments under identical conditions. It has been found that during upsetting and transient-state extrusion, the temperature in the billet is redistributed all over; it increases in the deformation zone close the die orifice and decreases in the rear part of the billet. Li et al [79], performed cylindrical hot compression tests to determine the dependence of the flow stress of a wrought magnesium alloy, AZ31B, on temperature, strain and strain rate. The tests covered wide ranges of temperature (300–500^{0}C) and strain rate (0.03–90 s^{-1}), as possibly encountered in real-life metal-forming processes. It was found that at a low strain rate, the flow curve reached a steady state at a large strain after the flow stress peak. At a high strain rate, however, the flow curve exhibited continuous flow softening after the peak. In addition, it was noticed that with increasing strain rate, deformation heating became more pronounced. The constants in the constitutive equation of the hyperbolic sine form were determined with the measured flow stresses corrected for deformation heating. Validation tests were then performed through 3D computer simulation of hot extrusion based on the corrected and uncorrected flow stress data, followed by real extrusion experiments under the identical conditions. Good agreements between the predicted and measured values in extrudate temperature and extrusion pressure were achieved. Reinikainen et al [80] in his work compared two commercial finite-element codes called DEFORM and FORGE 2 in the cold forward extrusion of an Al-l.2 (wt%) Si alloy. Comparison of the simulation results with the results of experiment showed generally good agreement, although during the early stages of extrusion both the measured temperature and force values appeared to be somewhat lower than the calculated values.

Kumar et al [81], the paper presents designing, fabrication and experiments for shaped extrusion of aluminum alloy (Al 2024) and lead alloy (70Pb30Sn). Flat and conical dies of H, T, L, elliptical and two-hole sections have been designed on the basis of upper bound technique by the authors for cold and hot extrusion. Hot extrusion has been performed in the temperature range 300–500 ◦C. Experimental investigation have been conducted for average extrusion pressure in cold case for lead alloy (70Pb30Sn) billets and in hot case for commercial grade aluminum (Al 2024) billets respectively. Extrusion pressure in the both cases has been compared with the theoretical work by the author for cold extrusion and for hot extrusion of aluminium alloy, results have been compared with a finite element based commercial package HyperXtrude. Theoretical results obtained by the upper bound technique and the HyperXtrude compare well with the experiments. Zhang at el [84] Extrusion stem speed is one of important process parameters during aluminum profile extrusion, which directly influences the profile quality and choice of extrusion equipments. In this paper, the extrusion process of a thin-walled hollow aluminum profile was simulated by means of the HyperXtrude commercial software.

Sivaprasad et al [83], the mechanical properties of a processed material depend to a great extent on the microstructural evolution during hot working. A thorough understanding of the various metallurgical processes with respect to the process parameters, namely temperature and strain rate are essential to decide the optimum parameters of processing. An attempt is made in this study to use the predictions of a processing map developed based on dynamic materials model and finite element simulation of the hot extrusion process to identify the optimum processing conditions. In the present simulation, a two-dimensional, axisymmetric, nonisothermal, rigid–plastic analysis was employed for the billet and the extrusion tooling, namely the ram and the container were considered as rigid bodies. The distribution of strains and strain rates in hot extrusion were predicted using a finite element analysis package (Marc 2000). This paper discusses the use of a processing map with the output of the finite element analysis to design the process.

In the work of Hansson et al [84], FE models of the stainless steel tube extrusion process were developed and used. Simulations were carried out for different tube dimensions and three different materials two austenitic stainless steels and one duplex (austenitic/ferritic) stainless steel. The models were validated by comparing the predicted values of extrusion force with measurements from production presses. A large number of input parameters are used in a FE analysis of extrusion. This includes boundary conditions, initial conditions and parameters that describe the mechanical and thermal properties of the material. The accuracy of the extrusion simulation depends, to a large extent, on the accuracy of these parameters. Experimental work, both in the form of material testing and production trials, was performed in order to give an accurate description of the input parameters in these extrusion models. A sensitivity analysis was performed for one of the models and the results showed that the initial billet temperature is the parameter that has the strongest impact on the extrusion force. In order to study the temperature evolution in the billet during manufacturing, the entire process chain at extrusion of stainless steel tubes was simulated using FEM. Pawel Kazanowski et al [85], the influence of the initial billet geometry on the product geometry during bi-material rod extrusion has been investigated. Both physical and numerical modeling techniques have been used in this study. Initial inner material length within a bi-material billet was optimized. The obtained experimental and numerical results confirmed the influence of the initial bi-material billet geometry on the geometrical stability of the extrudate cross-section. The proposed process modification resulted in improved process yield. A complex interface structure between AA2014 and AA6063 has been noted by light optical microscopy.

Donati et al [86], viscoplastic analyses with the rod technique were performed in the extrusion of AA6060 alloy at different processing conditions in order to measure the friction effect at the billet-container interface. During the trials an accurate monitoring of the relevant process variables such as punch force and temperatures was performed in order to validate FEM simulations. Different FE codes were used to carry out the simulations Deform, HyperXtrude, and Superform. A particular attention was given on evaluating the several coefficients of the available friction models by comparing the FEM results with experimental results. Flitta et al [87], this investigation focuses on simulation of the extrusion process and in particular the effect of the initial billet temperature on friction and its consequences on material flow. The simulation is compared with data obtained from an experimental extrusion press. All the simulations are performed with the implicit finite element codes FORGE2 and FORGE3.

Reddy et al [88], in this study presents an algorithm for optimal design of extrusion dies using an hp-adaptive finite element model and shape optimization based on an efficient response surface methodology. Of particular importance is the shape of the openings in the die. Response surface methodology is used to fit quadratic polynomials to the data from the flow analysis. Hp adaptive finite element analysis is used to obtain accurate flow solutions. Starting with an initial guess for the die geometry, we iteratively solve the fluid flow and optimization problems to produce a die design that satisfies the objective function and constraints. Results of two- and three-dimensional problems are presented to show the robustness of the approach and its effectiveness in simplifying the method of extrusion die design. The advantage of this approach is that, in addition to removing the guesswork out of mesh generation; it eliminates the time consuming trial-and error method of extrusion die design. The present research also highlights the usefulness of the response surface approach in multidisciplinary design optimization.Mahender P. Reddy [90], presented a numerical algorithm to automatically design polymer extrusion dies is developed. The method uses an adaptive finite element model and shape optimization methodology to define the transition section and the land lengths of a profile die. The ultimate goal of this work is to develop a simulation tool that could be used by extrusion die designers which functions like the CAD integrated simulation tools available for injection mould designers today. Reddy et al [91], presented a numerical algorithm to analyze and optimize aluminium extrusion dies is presented. Material flow and heat transfer in extrusion dies is analyzed using a finite element model. Bearing area shape/length optimization influences metal flow behavior and the quality of extruded product. The finite element model is coupled with an optimization algorithm to compute optimum bearing lengths/shapes. Reddy et al [89], presents a numerical algorithm that helps to optimize the design of aluminium extrusion dies is presented. The bearing area of the die is the last part of the die that comes in contact with the extruded metal before it leaves the container. Shape and length of the bearing area greatly influence the characteristics of the metal flow and the quality of the extruded product. The technique presented here adaptively determines the land length of the bearing so that uniform flow is produced over all regions of the profile. The method uses an adaptive finite element model and shape optimization methodology to define the bearing length in an aluminium extrusion die. Ultimately, the goal is to develop a simulation tool that could automatically determine the optimal design of the die. Two and three-dimensional cases are presented. Bastani et al [92], studied in this work the isothermal extrusion of Aluminum. Transient finite element simulations of the extrusion process have been performed over 20 press cycles using the 3D finite element software Altair HyperXtrude 9.0 and the 2D finite element software ALMA2π. The process parameters considered are front billet temperature, initial billet temperature gradient (taper), ram speed and container cooling rate. The press cycle has been divided into three phases start, middle and the end of the ram stroke. The best combinations of process parameters for isothermal extrusion has been found and represented as so called “isothermal maps” for each phase of the press cycle. Abdul et al [92], laboratory-scale extrusion experiments using a conical die were conducted on AZ61 billets of 1.25 inch diameter.

Experiments were performed with two different types of billets: cylindrical billets of 1.00 inch length, which did not have metal protruding into the conical die; and tapered billets of 1.60 inch length, which were also cylindrical but machined with extra taper to fit the die cone. Load and temperature data were recorded on the tooling for these two billet combinations. Comparison of the data from each of these two trials indicates expected results the breakthrough load did not vary significantly but the die temperature was drastically different. Based on this experimental data, Eulerian code, HyperXtrude, and Lagrangian code, ABAQUS, were used to simulate the extrusion process. While HyperXtrude has an implicit assumption that the die cavity is filled with metal at the beginning of the simulation cycle, ABAQUS can simulate the filling of the die cavity. Hence, commercial Lagrangian and Eulerian codes are compared with experimental evidence to validate the simulations.

2.8. FEM Simulation of Hot extrusion of Zr-2.5Nb-0.5Cu alloy

The morphology and distribution of the alpha and beta phase get greatly influenced during this hot extrusion stage[21], [22]. These micro structural and textural features are influenced by the actual temperature and stress distribution during the hot extrusion process. In addition, extruded product quality in terms of variation from leading end to tailing end, surface cracks, bend in bar, etc also depend on the presence of steep temperature gradients during the hot extrusion[78], [83]. Hence a detailed knowledge of the role of process parameters such as billet preheat temperature, extrusion speed, extrusion ratio etc on the temperature and stress distribution during the hot extrusion process can help tailor the process. However, the design and control of the experiments to acquire such information during hot extrusion process is rather difficult. An alternative approach could be application of computational / numerical analysis of the extrusion process for the process optimization. In the recent past the three-dimensional finite element analysis for hot extrusion is being pursued in case of aluminium based materials[84]–[86]. Such studies in case of the Zr based alloys seem to be rather limited in the open literature, forming the motivation to present study.

Arbitrary Lagrangian Eulerian FE formulation and 8 noded Hexahedron types of elements, which have shown great potential in the finite element methodology of metal forming, were used for the current study. Some of the key parameters of the extrusion process such as ram velocity, billet pre-heat temperature, fillet radius and reduction ratio, have been studied for their role in determining the overall temperature distribution during hot extrusion, requirement of ram force etc.

2.9. References

[1] M. Division and B. Atomic, “Zirconium alloys in nuclear technology,” vol. 4, no. April, pp. 41–56, 1981.

[2] B. Cheadle, C. Coleman, and H. Licht, “CANDU-PHWR pressure tubes: their manufacture, inspection, and properties,” Nucl. Technol.;(United States), 1982.

[3] B. Cox, “Some thoughts on the mechanisms of in-reactor corrosion of zirconium alloys,” J. Nucl. Mater., vol. 336, no. 2–3, pp. 331–368, Feb. 2005

[4] G. Sabol, “ZIRLOTM — An Alloy Development Success,” J. ASTM Int., vol. 2, no. 2, p. 12942, 2005.

[5] E. Tenckhoff, “Review of Deformation Mechanisms, Texture, and Mechanical Anisotropy in Zirconium and Zirconium Base Alloys,” J. ASTM Int., vol. 2, no. 4, p. 12945, 2005.

[6] K. L. Murty and I. Charit, “Texture development and anisotropic deformation of zircaloys,” Prog. Nucl. Energy, vol. 48, no. 4, pp. 325–359, May 2006.

[7] R. Krishnan and M. K. Asundi, “Zirconium alloys in nuclear technology,” Proceedigs Indian acadamy Sci. (Engg. Sci.), vol. 4, pp. 41–56, 1981.

[8] K. Kargol, J. Stevens, J. Bosma, J. Iyer, and G. Wikmark, “Modern fuel cladding in demanding operation - ZIRLO in full life high lithium PWR coolant,” in American Nuclear Society - 2007 LWR Fuel Performance/Top Fuel, 2007, pp. 169–175.

[9] R. L. Tapping, “Materials performance in CANDU reactors: The first 30 years and the prognosis for life extension and new designs,” J. Nucl. Mater., vol. 383, pp. 1–8, 2008.

[10] R. Holt, “In-reactor deformation of cold-worked Zr–2.5 Nb pressure tubes,” J. Nucl. Mater., 2008.

[11] D. O. Northwood and U. Kosasih, “Hydrides and delayed hydrogen cracking in zirconium and its alloys,” Int. Met. Rev., vol. 28, pp. 92–121, 198

[12] Kass, S., The Development of the Zircaloys. Corrosion in Zirconium Alloys. STP368. American Society for testing of Materials, Philadelphia, 1964.

[13] Rosenbaum, H.S., The Interaction of Iodine with Zircaloy-2, Electrochem. Technol. 4 (1966) 153–156.

[14] Rosenbaum, H.S. Davies J.H., and Pon J.Q., “the Interaction of Iodine with Zircaloy-2, “General Electric company Report GEAP-5100-5, 1966, (n.d.).

[15] Tomain, D. S., Adamson, R. B., and gangloff, R.P., “ Performance of Irradiated Copper and Zirconium Barrier Modified Zircaloy Cladding under simulated Pellet – Cladding Interaction Coditions,” Zirconium in the Nuclear Industry: Fourth International Symposium, ASTM STP 681, , Philadelphia, 1979. pp. 122-144, (n.d.).

[16] Davies, J. H., Rosenbaum, H. S., Armijo, J. S., Proebstle, R. A., Rowland, T. C., Thompson, J.R., Esch, E. L., Romeo, G., and Rutkin, D.R., “Irradiation Tests to Characterise the PCI Failure Mechanism, “ in Proceedings. ANS Topical Meeting on Water Reactor Fuel performance, American Nuclear Society, St. Charles, III., 1977, pp. 230-242, (n.d.).

[17] Rosenbaum, H. S., Davies, J. H., Adamson, R. B., Armijo, J.S., Rosicky, E., Wisner, S. B., Tucker, R. P., and Esch, E. L., “Resistance of Zirconium Barrier Fuel to Pellet-Cladding Interaction, “Transactions Of American Nuclear Society, Vol. 38, 1981, pp. 270-272, (n.d.).

[18] H. Rosenbaum, R. Rand, R. Tucker, B. Cheng, R. Adamson, J. Davies, J. Armijo, S. Wisner, Zirconium-Barrier Cladding Attributes, in: R. Adamson, L. Van Swam (Eds.), Zircon. Nucl. Ind., ASTM International, 100 Barr Harbor Drive, PO Box C700, West Conshohocken, PA 19428-2959, 1987: pp. 675-675–24.

[19] A.M. Garde, E.R. Bradley, ASTM Committee B-10 on Reactive and Refractory Metals and Alloys, Zirconium in the Nuclear Industry: Tenth International Symposium, ASTM, 1994..

[20] A.. Nowick, On the interpretation of "low-temperature" recovery phenomena in cold-worked metals, Acta Metall. 3 (1955) 312–321. .

[21] T. Lin, D. McLean, Changes produced by deformation in grains and grain boundaries of nickel, Met. Sci. J. 2 (1968) 108–113.

[22] A. Keh, S. Weissmann, Electron microscopy and strength of crystals, Intersci. N. Y. 231 (1963).

[23] G. Thomas and J. Washburn, P. R. Swann, in Electron Microscopy and Strength of Crystals, , Eds. (Interscience Publishers, New York, 1963), p. 172., (n.d.).

[24] A.M. Garde, H.M. Chung, T.F. Kassner, Micrograinsuperplasticity in Zircaloy at 850°C, Acta Metall. 26 (1978) 153–166.

[25] D. Lee, The strain rate dependent plastic flow behavior of zirconium and its alloys, Metall. Trans. 1 (1970) 1607–1616.

[26] M. Boček, G. Faisst, C. Petersen, Examination of the plastic properties of zircaloy-4 at elevated temperatures in air atmosphere, J. Nucl. Mater. 62 (1976) 26–36..

[27] M.J. Luton, J.J. Jonas, Solute strengthening at high temperatures in zirconium-tin alloys, Can. Metall. Q. 11 (1972) 79–90.

[28] H.M. Chung, A.M. Garde and T.F. Kassner, UNIAXIAL TENSILE PROPERTIES OF ZIRCALOY CONTAINING OXYGEN: SUMMARY REPORT, ANL-75-78, Quarterly Progress Report, 1977.

[29] H.J. Frost, M. F. Ashby, Deformation-mechanism maps, Pergamon press, 1982.

[30] R. Raj, Metallurgical Transactions A, 12 (1981) 1089-1097.

[31] Y.V.R.K. Prasad. Metal. Trans. A27 (1996) 235-236

[32] Ziegler.H. Progress in solid mechanica, ed. I.N.Sneddon and R.Hill. 1963:93.

[33] B.. Mehrotra, K. Tangri, High temperature (600–800°C) thermally activated deformation behaviour of α-Zircaloy-4-Oxygen alloys, Acta Metall. 28 (1980) 1385–1394..

[34] D.J. Abson, J.J. Jonas, Substructure strengthening in zirconium and zirconium-tin alloys, J. Nucl. Mater. 42 (1972) 73–85..

[35] J.K. Chakravartty, G.K. Dey, S. Banerjee, Y.V.R.K. Prasad, Characterization of hot deformation behaviour of Zr□2.5Nb□0.5Cu using processing maps, J. Nucl. Mater. 218 (1995) 247–255..

[36] J.K. Chakravartty, S. Banerjee, Y.V.R.K. Prasad, M.K. Asundi, Hot-working characteristics of Zircaloy-2 in the temperature range of 650–950°C, J. Nucl. Mater. 187 (1992) 260–271..

[37] R. Kapoor, J.K. Chakravartty, Characterization of hot deformation behaviour of Zr–2.5Nb in β phase, J. Nucl. Mater. 306 (2002) 126–133. J. Chakravartty, R. Kapoor, S. Banerjee, Y. Prasad, Characterization of hot deformation behavior of Zr–1Nb–1Sn alloy, J. Nucl. Mater. 362 (2007) 75–86.

[38] Y.C. Lin, Y.C. Xia, X.M. Chen, M.S. Chen, Computational Materials Science, 50 (2010) 227-233.

[39] C. G'Sell, A. Marquez-Lucero, P. Gilormini, J.J. Jonas, ActaMetallurgica, 33 (1985) 759-770.

[40] A. Cingara, H.J. McQueen, Journal of Materials Processing Technology, 36 (1992) 31-42.

[41] A. Cingara, H.J. McQueen, Journal of Materials Processing Technology, 36 (1992) 17-30.

[42] Z.H.A. Kassam, Z. Wang, E.T.C. Ho, Materials Science and Engineering: A, 158 (1992) 185-194.

[43] R. Liang, A.S. Khan, International Journal of Plasticity, 15 (1999) 963-980.

[44] M.A. Meyers, O. Vöhringer, V.A. Lubarda, ActaMaterialia, 49 (2001) 4025-4039.

[45] A.K. Mukherjee, Materials Science and Engineering: A, 322 (2002) 1-22.

[46] M.A. Meyers, D.J. Benson, O. Vöhringer, B.K. Kad, Q. Xue, H.H. Fu, Materials Science and Engineering: A, 322 (2002) 194-216.

[47] R. Ebrahimi, S.H. Zahiri, A. Najafizadeh, Journal of Materials Processing Technology, 171 (2006) 301-305.

[48] D. Samantaray, S. Mandal, A.K. Bhaduri, Materials & Design, 31 (2010) 981-984.

[49] S. Banerjee, P.S. Robi, A. Srinivasan, L. Praveen Kumar, Materials Science and Engineering: A, 527 (2010) 2498-2503.

[50] D. Samantaray, C. Phaniraj, S. Mandal, A.K. Bhaduri, Materials Science and Engineering: A, 528 (2011) 1071-1077.

[51] Z. Wang, L. Qi, J. Zhou, J. Guan, J. Liu, Computational Materials Science, 50 (2011) 2422-2426.

[52] D. Samantaray, S. Mandal, A.K. Bhaduri, S. Venugopal, P.V. Sivaprasad, Materials Science and Engineering: A, 528 (2011) 1937-1943.

[53] C.M. Sellars, W.J. McTegart, ActaMetallurgica, 14 (1966) 1136-1138.

[54] J.J. Jonas, C.M. Sellars, W.J.M. Tegart, Metallurgical Reviews, 14 (1969) 1-24.

[55] H.J. McQueen, Metallurgical and Materials Transactions A, 33 (2002) 345-362.

[56] H.J. McQueen, N.D. Ryan, Materials Science and Engineering: A, 322 (2002) 43-63.

[57] C. Phaniraj, D. Samantaray, S. Mandal, A.K. Bhaduri, Materials Science and Engineering: A, 528 (2011) 6066-6071.

[58] D. Samantaray, S. Mandal, A.K. Bhaduri, Computational Materials Science, 47 (2009) 568-576.

[59] C. Zener, J.H. Hollomon, Journal of Applied Physics, 15 (1944) 22-32.

[60] D. Samantaray, S. Mandal, A.K. Bhaduri, P.V. Sivaprasad, Trans Indian Inst Met, 63 (2010) 823-831.

[61] F.J. Humphreys, M. Hatherly, Recrystallization and Related Annealing Phenomena, 2 ed., PERGAMON, 2004.

[62] H. Mirzadeh, A. Najafizadeh, M. Moazeny, Metallurgical and Materials transactions A, 40 (2009) 2950-2958.

[63] T. Sakai, Journal of Materials Processing Technology, 53 (1995) 349-361.

[64] A. Paine, M. Aloe, J. Walters, Simulation of hot extrusion processes, Alum. Extrus. (2002) 39–45.

[65] P.V. Sivaprasad, S. Venugopal, C.H.J. Davies, Y.V.R.K. Prasad, Identification of optimum process parameters for hot extrusion using finite element simulation and processin

[66] M.S. Gadala, J. Wang, ALE formulation and its application in solid mechanics, Comput. Methods Appl. Mech. Eng. 167 (1998) 33–55. L. Filice, I. Alfaro, F. Gagliardi, E. Cueto, F. Micari, F. Chinesta, A preliminary comparison between

finite element and meshless simulations of extrusion, J. Mater. Process. Technol. 209 (2009) 3039–3049.

[67] I. Alfaro, F. Gagliardi, E. Cueto, L. Filice, F. Chinesta, Simulation of Porthole Die Extrusion Process comparing NEM and FEM modelling, in: Trans Tech Publ, 2010: pp. 97–104.

[68] P. Cleary, M. Prakash, J. Ha, Novel applications of smoothed particle hydrodynamics (SPH) in metal forming, J. Mater. Process. Technol. 177 (2006) 41–48.

[69] I. Alfaro, D. Bel, E. Cueto, M. Doblaré, F. Chinesta, Three-dimensional simulation of aluminium extrusion by the α-shape based natural element method, Comput. Methods Appl. Mech. Eng. 195 (2006) 4269–4286.

[70] T. Belytschko, W.K. Liu, B. Moran, K. Elkhodary, Nonlinear finite elements for continua and structures, John wiley& sons, 2013.

[71] M. Lee, S. Chung, S. Jang, M. Joun, Three-dimensional simulation of forging using tetrahedral and hexahedral elements, Finite Elem. Anal. Des. 45 (2009) 745–754.

[72] S. Hansson, Modeling of the stainless steel tube extrusion process, (2010).

[73] A.K. Rout, A Class of Solutions for Extrusion through Converging Dies, PhD Thesis. (2010).

[74] S.-H. Hsiang, C.-S. Liao, Study on hot extrusion of tubes, J. Mater. Process. Technol. 63 (1997) 254–259.

[75] L.X. Li, K.P. Rao, Y. Lou, D.S. Peng, A study on hot extrusion of Ti–6Al–4V using simulations and experiments, Int. J. Mech. Sci. 44 (2002) 2415–2425..

[76] F. Parvizian, T. Kayser, C. Hortig, B. Svendsen, Thermomechanical modeling and simulation of aluminum alloy behavior during extrusion and cooling, J. Mater. Process. Technol. 209 (2009) 876–883.

[77] L. Li, J. Zhou, J. Duszczyk, Prediction of temperature evolution during the extrusion of 7075 aluminium alloy at various ram speeds by means of 3D FEM simulation, J. Mater. Process. Technol. 145 (2004) 360–370..

[78] G. Liu, J. Zhou, J. Duszczyk, Prediction and verification of temperature evolution as a function of ram speed during the extrusion of AZ31 alloy into a rectangular section, J. Mater. Process. Technol. 186 (2007) 191–199..

[79] L. Li, J. Zhou, J. Duszczyk, Determination of a constitutive relationship for AZ31B magnesium alloy and validation through comparison between simulated and real extrusion, J. Mater. Process. Technol. 172 (2006) 372–380.

[80] T. Reinikainen, T. Welo, A.S. Korhonen, S. Kivivuori, Comparison of two commercial FEM codes in cold extrusion simulation, J. Mater. Process. Technol. 42 (1994) 137–146.

[81] S. Kumar, P. Vijay, Die design and experiments for shaped extrusion under cold and hot condition, J. Mater. Process. Technol. 190 (2007) 375–381.

[82] C. Zhang, G. Zhao, Z. Chen, H. Chen, F. Kou, Effect of extrusion stem speed on extrusion process for a hollow aluminum profile, Mater. Sci. Eng. B. 177 (2012) 1691–1697.

[83] P. Sivaprasad, S. Venugopal, C. Davies, Y. Prasad, Identification of optimum process parameters for hot extrusion using finite element simulation and processing maps, Model. Simul. Mater. Sci. Eng. 12 (2004) 285.

[84] S. Hansson, Modeling of the stainless steel tube extrusion process, (2010).

[85] P. Kazanowski, M.E. Epler, W.Z. Misiolek, Bi-metal rod extrusion—process and product optimization, Mater. Sci. Eng. A. 369 (2004) 170–180.

[86] L. Donati, L. Tomesani, M. Schikorra, N.B. Khalifa, A. Tekkaya, Friction model selection in FEM simulations of aluminium extrusion, Int. J. Surf. Sci. Eng. 4 (2009) 27–41.

[87] I. Flitta, T. Sheppard, Nature of friction in extrusion process and its effect on material flow, Mater. Sci. Technol. 19 (2003) 837–846.

[88] M. Reddy, O. Hardy, H. Thomas, P. Bangarpet, Optimal design of extrusion dies using hp-adaptive finite element model, in: 1998: p. 4790.

[89] Mahender P. Reddy, Edward G. Schaub, Computational Mechanics Company, Inc., Austin, TX Louis G, Design and optimization of three dimensional extrusion dies using FEM, Presented at ANTEC'99 New York, (n.d.).

[90] Mahender P. Reddy, RavisankarMayavaram, David Durocher, HakanCarlsson, Ola Bergquist, Analysis and Design Optimization of Aluminum Extrusion Dies, 8th International Extrusion Technology Seminar – Orlando, FL – May 2004., (n.d.).

[91] Mahender P. Reddy, Osama N. Hamzeh, Optimization of bearing surfaces in aluminium extrusion die design, Presented at OPTICON '99., (n.d.).

[92] AbdulAfooParkar, ClemenceBouvard, Stephen J. Horstemeyer, Esteban B. Marin, Paul T. Wang, Mark F., Experiments and Simulation of AZ61 Extrusion through Conical Dies with Eulerian and Lagrangian, Horstemeyer Alum. Extrus. Technol. (n.d.).

Chapter 3

Experimental

Preamble: Experimental work carried out to complete the entire work of thesis starts with preparation of alloy using VAR melting and alloy thus obtained has been deformed using hot compression testing and extrusion. Deformed samples are studied for microstructure using optical microscopy, scanning electron microscopy and transmission Electron Microscopy. EBSD methods have been used to understand the change in microstructure as well as microtexture. Extrusion of both Zr-0.3Sn and Zr-2.5Nb-0.5Cu with different temperature and strain rate were carried out to validate the simulation results obtained using customized FEM based software.

3.1. Preparation of Zr-Sn alloy

Zircaloy-2 and Zr-2.5Nb-0.5Cu alloy were obtained from Nuclear Fuel Complex, whereas synthesis of Zr-0.3Sn was carried out in following manner:

Low oxygen Zirconium sponge with oxygen content around 600 ppm was mixed with Sn in required proportion and consolidated into cylindrical compact logs using a 2000 ton hydraulic press. These compacts were subsequently welded together longitudinally using electron beam welding to form the requisite electrodes for further melting. These welded compacts, which act as the electrodes, were melted in a vacuum arc furnace multiple times to form a 350 mm diameter ingot. Cylindrical specimens for compression testing with 15 mm height and 10 mm diameter were machined along the axial direction of this ingot. The starting as-cast microstructure is shown in Fig. 3.1.

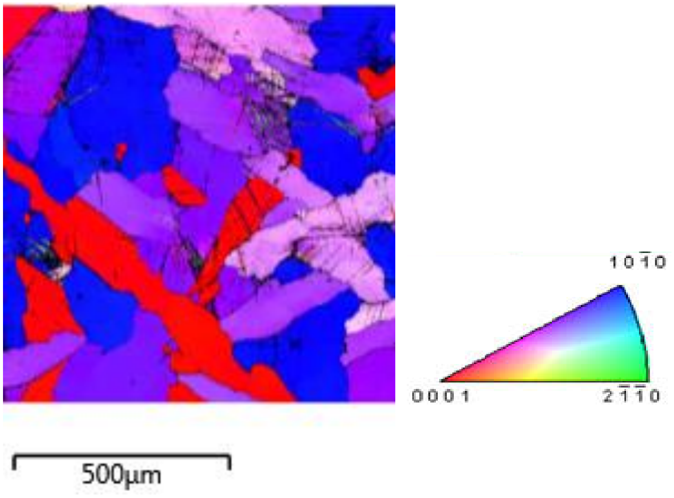

Fig. 3.1 The microstructure of the as-cast material

The Chemical composition of Zr-0.3Sn alloy is tabulated in table 3.1.

Element	Tin	Oxygen	Iron	Chromiun	Nickel
Chemical composition (wt %)	0.28	600 ppm	500 ppm	100 ppm	24 ppm

The Chemical composition of Zr-2.5Nb-0.5Cu is tabulated in table 3.2.

Element	Nb	Oxygen	Cu	Chromiun	Nickel
Chemical composition (wt %)	2.45	800 ppm	0.45%	100 ppm	24 ppm

The Chemical composition of Zircaloy-2 is tabulated in table 3.3.

Element	Tin	Oxygen	Iron	Chromiun	Nickel
Chemical composition (wt %)	1.45%	900 ppm	0.03%	0.08%	0.025%

3.2. Microstructure characterization

3.2.1. Sample Preparation for Microscopy

Preparation of Specimens for Optical Microscopy

Appropriately heat treated specimens were first ground on successive grades of silicon carbides paper down to 600 grade. After cleaning the samples were chemically polished and/or etched in a solution containing 50 parts of water, 40 to 45 parts of nitric acid and 5 to 10 parts of hydrofluoric acid. It was noticed that the etching was very uniform with 6 to 7 parts of the hydrofluoric acid.

Samples prepared for optical microscopy could be used directly for X-ray diffraction investigations for phase identification and analysis [1]. The same samples could also be used for scanning electron microscopy studies using the back scattered electron and the secondary electron modes of imaging.

Preparation of Specimens for Scanning Electron Microscopy

Specimens for secondary electron imaging were prepared in a similar manner as that for the optical microscopy specimens. After mechanical polishing samples were chemically polished and/or etched in a solution containing 50 parts of water, 40 to 45 parts of nitric acid and 5 to 10 parts of hydrofluoric acid. In case of back scattered imaging specimens were only polished to the mirror finish by using both mechanical and chemical methods [2].

Preparation of Specimens for Orientation Imaging Microscopy

Coarse grinding was used to produce flat surface for examination and it started with 240 upto 1200 grit SiC. Polishing is used to remove any deformation introduced earlier during grinding and it is done by alumina abrasives and diamond solutions for harder materials. Alumina is used as final polishing medium, however for good EBSD pattern quality colloidal silica was used. Mechanical polishing alone is not enough to produce good EBSD patterns and subsequently electro-polishing was used [3].

Preparation of Specimens for Transmission Electron Microscopy

For preparing specimens for transmission electron microscopy (TEM) [4] slices of thickness of about 0.5 mm were cut with a low speed diamond saw from appropriately treated specimens of different alloys. When required, theses slices were subjected to the desired heat treatments. These slices and strips were ultrasonically cleaned, ground on both sides with 320 grit silicon carbide abrasive paper until they were 100-150 μm thick, and then ultrasonically cleaned again. Disc specimens of 3 mm diameter were punched out from the sliced and ground material, followed by thinning by dual jet electropolishing in a Tenupol dual jet electropolisher, using an electrolyte consisting of perchloric acid (30 parts), n butanol (170 parts), and methanol (300 parts). The thinning was carried out by maintaining the electrolyte temperature at around -40°C and using a voltage of 20 V. Immediately after perforation the discs were removed from the electrolyte and thoroughly rinsed with methanol.

3.2.2. Microscopy Examination of the Specimen

Optical microscopy investigations of the heat treated samples were performed using Carl zeiss and Leika microscopes. Bright field as well as polarized light images were examined.

Scanning Electron Microscope (SEM) based Electron Backscattered Diffraction (EBSD) was used to characterize the hot deformed microstructures[5–7].The sample preparation involved cutting the deformed cylindrical samples along the axial-radial plane of the deformed samples, which contained two distinctly identifiable directions. This was followed by metallographic polishing and electropolishing using a 20% by volume solution of perchloric acid in methanol at -30° C with an applied potential difference of 20 V for 20 s. The EBSD mapping was carried out using an Oxford Nordlys® detector attached to a Carl Zeiss Auriga CrossBeam® Scanning Electron Microscope (SEM). A step size of 0.3 μm was used for all the scans and the camera settings were kept the same for all scans.

Some of the TEM thin foils were examined in a JEOL 3010 microscope and some others JEOL-2000-FX microscopes operating at 200 kV and 300 kV respectively. Standard electron microscopy techniques like bright and high resolution dark field microscopy, selected area diffraction (SAD), weak beam imaging, etc. were employed.

3.3. Bulk texture measurement

The bulk textures of the deformed samples were recorded using a PANalytical™ PRO-MRD XRD system. These measurements were taken from the middle region of the specimen and hence, are unaffected by the localized dead-metal zone near the sample-loading plate interface. Four incomplete pole figures ({01-11}, {01-12}, {0002} and {01-13}) were measured and used for constructing the orientation distribution functions (ODF). The basal pole figures were computed from the ODFs.

3.4. Hot compression test

The material used for this study was a cast Zr - 0.3 Sn dilute alloy, from which, cylindrical specimens of 15 mm height and 10 mm diameter were machined along the axial direction. A graphite sheet was placed between the specimens and the crossheads of the anvil to reduce the friction during compression. The temperatures of specimen as well as the adiabatic temperature rise during compression at high strain rate ($1s^{-1}$) were measured by two thermocouples attached directly to the middle area of the specimens. The isothermal compression tests were carried out on a Gleeble-3500® (Thermo-Mechanical Simulator) in the temperature range of 600°-900° C and strain rates of 10^{-2} – $10s^{-1}$. All specimens were deformed up to a true strain of 0.69. During the hot compression run, the flow stress data were recorded automatically as a function of strain for each deformation temperature and strain rate by the software directly linked with Gleeble-3500®. During deformation, the change in the microstructure in terms of grain/sub-grain orientation and grain refinement at different temperatures and strain rates was analysed using EBSD technique. The micro structural features which evolved at the different temperatures and strain rates gave an indication of the extent of recovery and recrystallization in the sample. The bulk texture measurements were also obtained for this alloy capturing the deformation behavior of this alloy in α as well as the α + β phase domain. The work carried out in processing of this material has been also validated with regards to the optimum deformation parameters obtained by development of processing maps. Number of tests were carried out to check the metallurgical and mechanical properties. This alloy has been also co extruded with Zircaloy tube to see its flow behavior during hot extrusion. Domain of deformation identified has been used to investigate the effect of temperature and strain rate on flow behavior of this alloy.

3.5. Hot extrusion of Zr- 0.3Sn and Zircaloy

Co extrusion was selected as a primary step in manufacturing of double clad hollow having inner layer of ZrSn alloy over outer shell of Zircaloy-2 followed by co reduction in a pilger mill in several passes with intermediate recrystallization anneals. A process flow sheet as given in fig 3.4 was designed to produce thin wall the Zr-Sn linned Zircaloy-2 tube.

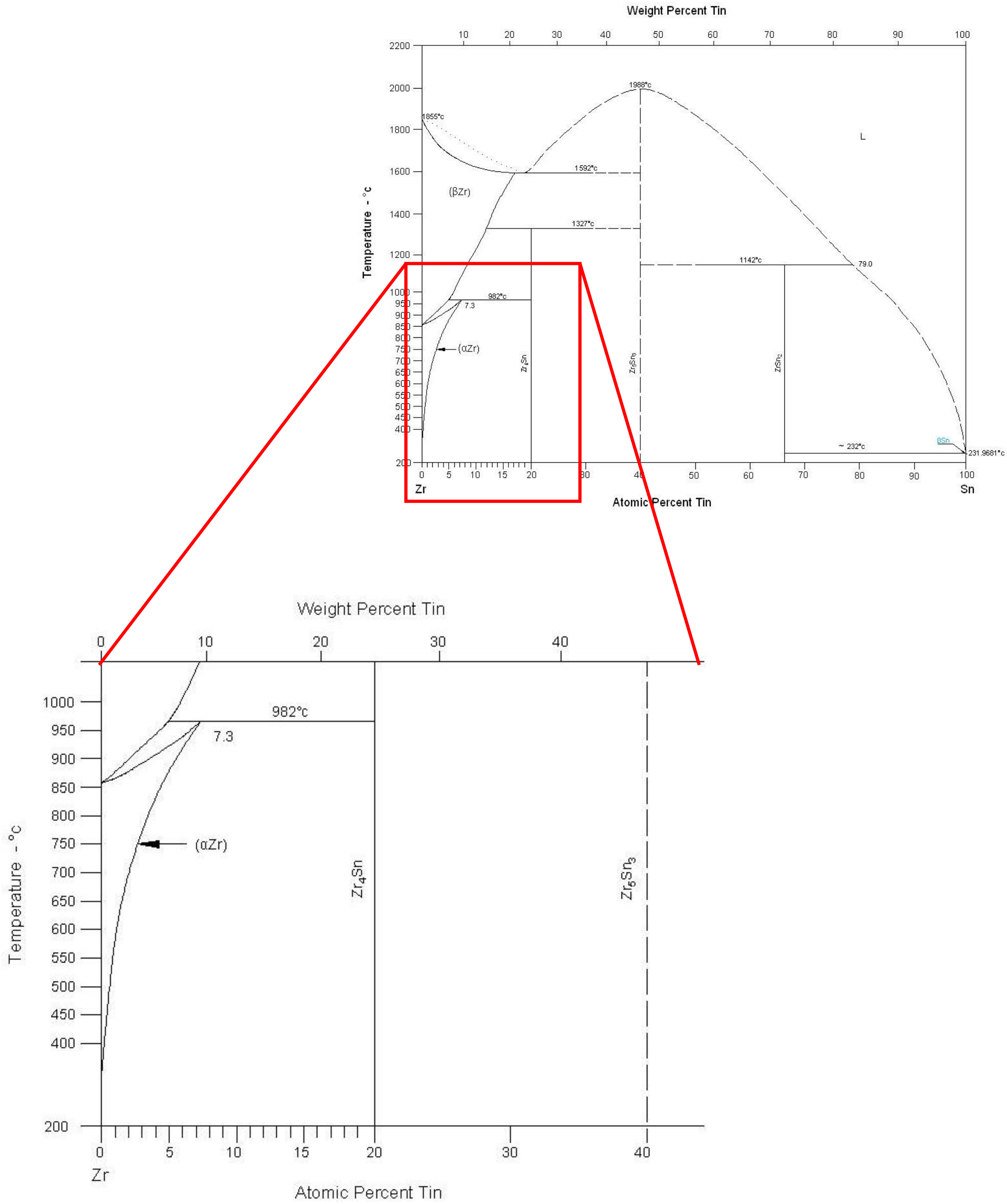

Fig 3.2 Phase diagram of Zr-Sn

3.5.1. Billet preparation

Hollow billet of Zr-2 was machined in ID with a very close tolerance and Zr-Sn liner tube was also machined with a positive tolerance for shrink fitting. Billet assembly is a very important task in the experiment of co-extrusion. For initial co-extrusion trials composite billets were prepared by hot shrink fitting and without EB welding at interfaces on two perpendicular surfaces. Due to lower flow stress of Zr-Sn which is a liner has the tendency to extrude much faster than the Zr-2 billet causing bursting of the liner in the front end. After conducting number of trials on bonding by shrink fitting, an optimized billet assembly procedure was employed in sequential steps as shown in fig 3.5. During the composite billet assembly, the machined liner was shrink fitted into the already machined billet with an interference of 0.05 mm. The composite billet was machined to the required dimensions. Initially one end of the billet-liner interface was welded using electron beam welding and other end of the liner was electron beam welded leaving a small opening to the interface. Opening provided on face of the billet was then evacuated by a vacuum pump to remove any air entrapped in between the interface of ZrSn liner and inner face of Zircaloy-2 billet. The composite billets were copper jacketed in ID and OD with a purpose to prevent excessive oxidation during preheating and provide lubrication.

3.5.2. Finite element model development

Many finite element packages are available for simulating the bulk deformation process. For our purpose, we used Finite element software, Deform-2D for simulation of the Co-extrusion process [35].

Initially a geometric model was developed resembling the co-extrusion process, in which the relative arrangement of different objects required for to simulate the process were made. The

GUI of Deform-2D software showing the geometries of the objects and their arrangement developed for co-extrusion is shown in figure 3.3.

The objects in the model

Billet of Zr-2 material of dimensions – 142 mm OD and 53.6 mm ID

- Liner of Zr-Sn material – 53.6 mm OD and 40 mm ID
- Die with semi die angle – 45 deg
- Container size – 150 mm
- Extrusion ram for applying the required force
- Mandrel of size – 34 mm

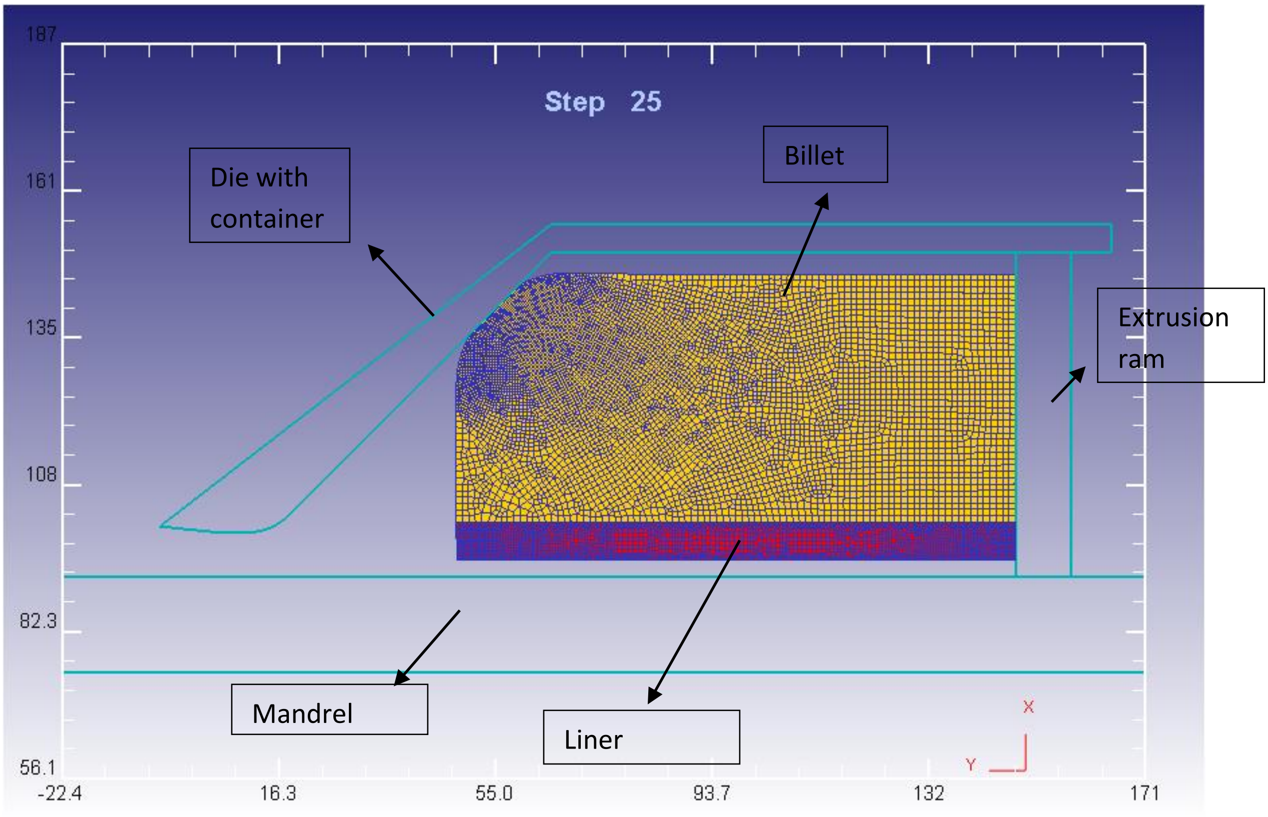

Fig.3.3 GUI of deform-2D showing the geometries of workpiece and tools

The features of the FEM model used for simulating the Co-extrusion process table 4.

Table 3.4 features of the FEM model

Sr. No.	Parameter	Remarks
1	Dimension	2D
2	Type of Geometry model considered	Axi-symmetric
3	Element type	4 noded quadrilateral element
4	FEA approach	Lagrangian incremental
5	Solver type	Sparse Solver
6	Iteration method	Newton Raphson method
7	Remesh criteria	Considered
8	Workpiece	Only plastic deformation
9	Modules considered	Heat transfer and deformation

3.5.3. Assumptions and Boundary conditions

The following were the boundary conditions considered in the FEM model developed.

1. A constant heat transfer and friction coefficients were considered between workpiece and tools throughout the extrusion process.
2. The workpiece was considered as plastic material with no elastic deformation.
3. 90 % of the deformation work in the extrusion process is converted to heat.
4. The tools were considered to be perfectly rigid with constant temperature throughout the extrusion process.
5. The workpiece cannot penetrate through the tools thereby restricting the movement of material beyond tool surface.

6. The workpiece temperature was considered to be uniform throughout the material.
7. The model does not include the thermal expansion of the workpiece.
8. The workpiece properties were uniform throughout the cross section without any defects. The model does not include any nonhomogeneity in the billet material.

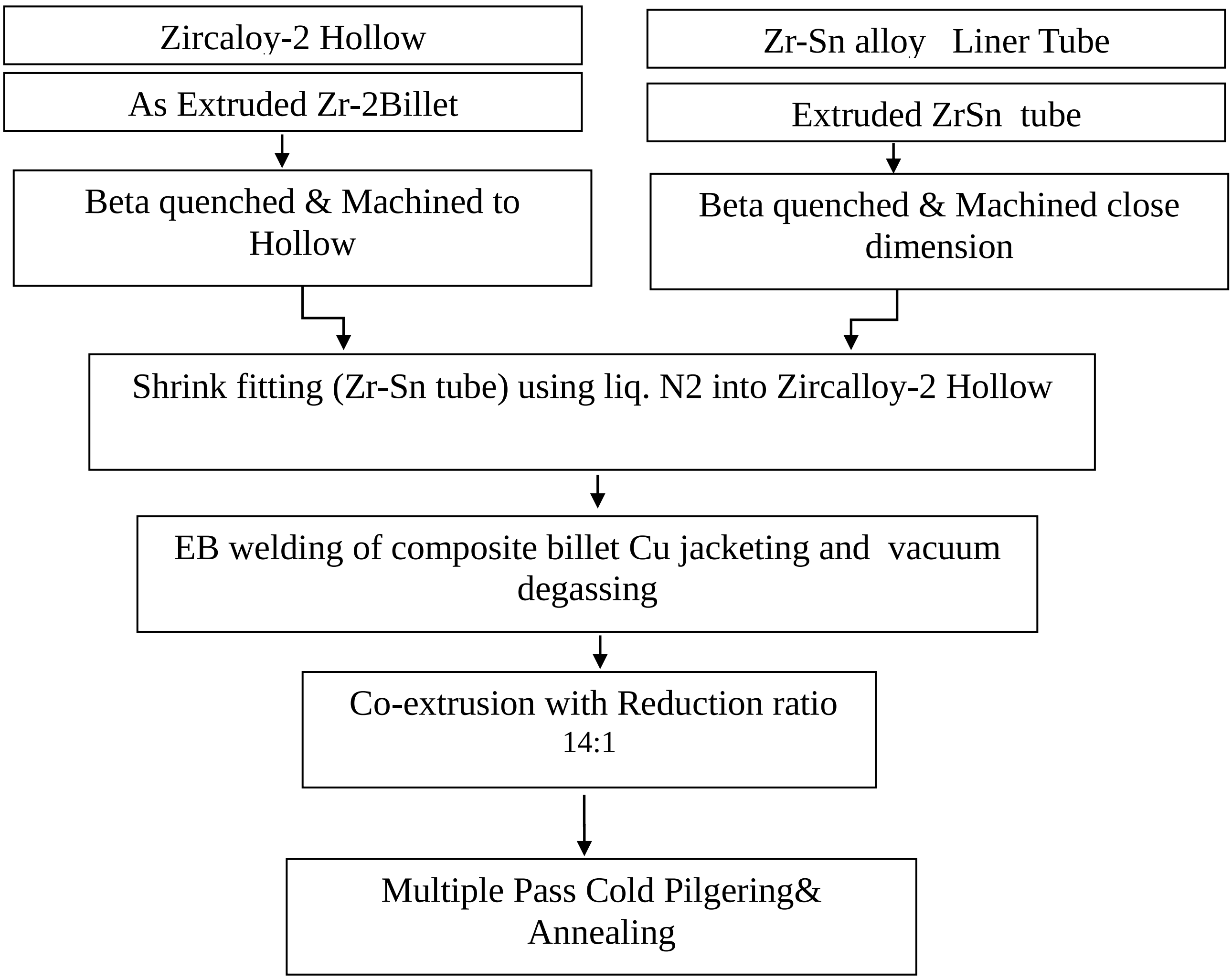

Fig 3.4: Shows the process flow chart of the Zr-Sn lined Zr-2 double clad

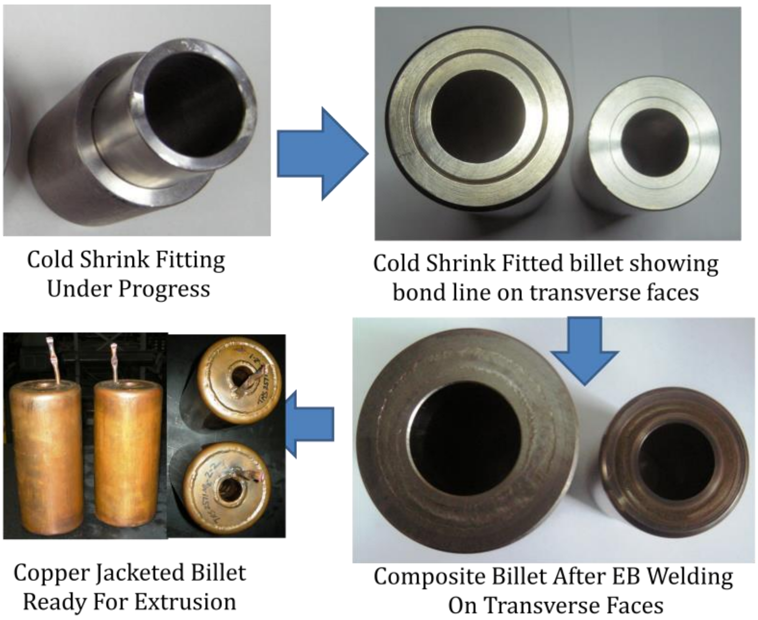

Fig.3.5 Composite Billet preparation in sequential steps

3.6. Hot Extrusion of Zr-2.5Nb-0.5Cu Billet

β-quenched billets of 142mm OD X 550mm length were mechanically jacketed with seamless copper tubes. Jacketed billet was preheated in a resistance heating furnace at 800°C and extruded in a 3780T Horizontal Extrusion Press (HEP) maintaining extrusion ratio of 44:1 and ram speed in the range of 20 to 50 mm/sec. Billets were preheated in a resistance heating furnace and temperature was varied in the range of 700 to 850°C. Copper jacketing of billet prevents oxidation of Zr-2.5Nb-0.5Cu billet and also provides the additional lubricant with oil based graphite. Copper cladding prevents direct contact of material with the extrusion tooling surfaces which otherwise would stick because of galling nature of Zirconium alloys. Copper jacketing remained on the rod surface after extrusion was removed by dissolution into HF& HNO_3 solution.

3.7. References:

[1] V. Accordingly, I. Boxes, Principles of X-ray Diffraction, 2006.

[2] K.D. Vernon-Parry, Scanning electron microscopy: An introduction, III-Vs Rev. 13 (2000) 40–44.

[3] F.J. Humphreys, Characterisation of fine-scale microstructures by electron backscatter diffraction (EBSD), Scr. Mater. 51 (2004) 771–776.

[4] G. Thomas, Transmission electron microscopy of metals, (1962).

[5] A.J. Wilkinson, T. Ben Britton, Strains, planes, and EBSD in materials science, Mater. Today. 15 (2012) 366–376.

[6] N. Allain-Bonasso, F. Wagner, S. Berbenni, D.P. Field, A study of the heterogeneity of plastic deformation in IF steel by EBSD, Mater. Sci. Eng. A. 548 (2012) 56–63.

[7] R. Quey, P.R. Dawson, J.H. Driver, Grain orientation fragmentation in hot-deformed aluminium: Experiment and simulation, J. Mech. Phys. Solids. 60 (2012) 509–524.

[8] N. Subasic, Thermodynamic Evaluation of Sn-Zr Phase Diagram, Calphad. 22 (1998) 157–165.

[9] N. Nieva, Experimental partial phase diagram of the Zr – Sn – Fe system, J. Nucl. Mater. 359 (2006) 29–40.

Chapter 4

Microstructural and textural evolution during hot deformation of Dilute Zr-Sn alloy

Preamble: Thermo-mechanical simulator was used to deform the Zr-0.3Sn alloy samples in as cast condition at different set of temperature and strain rates. Deformed samples have been studied for microstructure and texture using EBSD technique.

4.1. Introduction

The fuel for commercial light water nuclear reactorsis composed of uranium dioxide pellets in a sheath or cladding of Zirconium based alloys[1–4]. In boiling water based nuclear reactors, the cladding is of Zircaloy-2 [3,5,6] while in pressurized water based nuclear reactors, the fuel cladding is of Zircaloy-4 or other Zr-based alloys such as Zirlo® and M5®[7–9]. Such fuel-cladding is susceptible to a persistent failure mechanism known as fuel pellet clad interaction (PCI), which occurs on sudden increase of fuel rod power after long operation at a lower power [10–12]. The PCI mechanism involves the simultaneous effects of stress on the cladding imposed by the expansion of the pellet and the release of fission products, some of which act as stress corrosion cracking agents [13,14]. In the past, a significant improvement in the clad performance was achieved by stringent control on the alloy chemistry, microstructure and texture. With the continued emphasis on the increased fuel burnup, efforts have begun to further improve the clad performance by employing fuel clad materials with better resistance to irradiation damage [15,16] and to PCI. One of such efforts to mitigate PCI-induced damage was in the form of a double layer cladding, in which an inner layer with lower hardness acts as an effective barrier for PCI degradation. The inner barrier cladding is designed to absorb the PCI induced stresses so that cracks cannot propagate through the cladding [17–19].

In a double-clad, an inner liner tube of a dilute Zirconium alloy is metallurgically bonded to the outer Zircaloy layer to form a composite tube with a relatively softer inner surface. Initially, pure Zr was employed as the liner material, but showed poor oxidation resistance [20–22]. In recent years,an alloy of Zr and 0.3% (by weight) Sn is being used as the liner material which is seen to possess better oxidation resistance along with resistance against stress corrosion cracking [23].

The Zr-Sn double-clad tubes are manufactured by co-extrusion at an elevated temperature to form a composite tube of Zircaloy with an inner liner of Zr-Sn , followed by co-reduction in pilger mills in several passes with intermediate recrystallization anneals [24,25]. The integrity of the bond between the two layers of the double-clad determines the performance of the composite tube. While each stage of fabrication of this composite tube has a bearing on the final properties of the tubes (in terms of bond strength of the two layers etc.), most significant step is hot extrusion, wherein the metallurgical bond is established between the two co-extruded layers. It has been established that if the difference in flow properties of two different materials is wide, fracture, decohesion or delamination and non uniform flow may take place during thermo mechanical processing of a composite billet or tube [26,27]. This implies that a successful co-extrusion of the composite tubes requires knowledge of the flow behaviour and microstructural evolution of both the materials (inner layer and outer layer) under question. While the thermo-mechanical properties of Zircaloys (outer layer) have been studied extensively [1,4,22] and are available, no data is available on the flow behaviour of Zr-0.3Sn. Hence, this study has been carried out to understand the deformation behaviour, microstructure and texture evolution of the dilute Zr-0.3Sn alloy. The objective was to document the microstructural and textural changes accompanying the hot deformation of this particular alloy in the processing conditions relevant to industrial practice of Zr based composite clad tube fabrication.

4.2. Flow behaviour

4.2.1. Temperature Effect:

The series of flow curves presented in Fig. 4.1 depict the flow behaviour of the Zr-0.3Sn alloy as a function of temperature and strain rate. Considerable differences in the strain hardening behaviour as a function of both temperature and strain rate are evident. While lower temperature regime (below 750 °C) is dominated by higher strain hardening, high temperature (800 °C) deformation is characterized by appreciably lower hardening, if any.

The work hardening nature was predominant in the flow curves at the temperatures of 600° and 650° C. While some work hardening behaviour was observed for the strain rates higher than 1 s^{-1} at 750° C, for lower strain rates at this temperature and for all strain rates at higher temperatures, negligible work hardening was seen. It could be clearly seen that the material underwent lesser work hardening as the temperature was increased. In fact, at the temperature of 900° C, the flow curves are effectively flat, for all strain rates considered. Another interesting observation was that the flow curves for different strain rates were widely separated at lower temperatures and were spaced much closer at higher temperatures. This showed that the flow stress sensitivity to the strain rate was an inverse function of temperature.

4.2.2. Strain Rate Effect:

Engineering stress strain curves of cast Zr-Sn alloy obtained at different strain rates and in the temperature range of 600 to 900 °C are shown in figure 4.2 (a)-(c). As is evident from this figure at any given strain-rate the flow stress was observed to decrease with increase in temperature. There is no general trend in variation of flow stress. Two distinct types of flow curves during deformation could be identified; one which show continuous strain hardening and while others show initial hardening up to very small strain followed by steady state flow behaviour. Strain hardening effect is seen primarily in those alloys which are deformed at 600° C and 650° C for all strain rates extent of which increases with increase in strain rates.

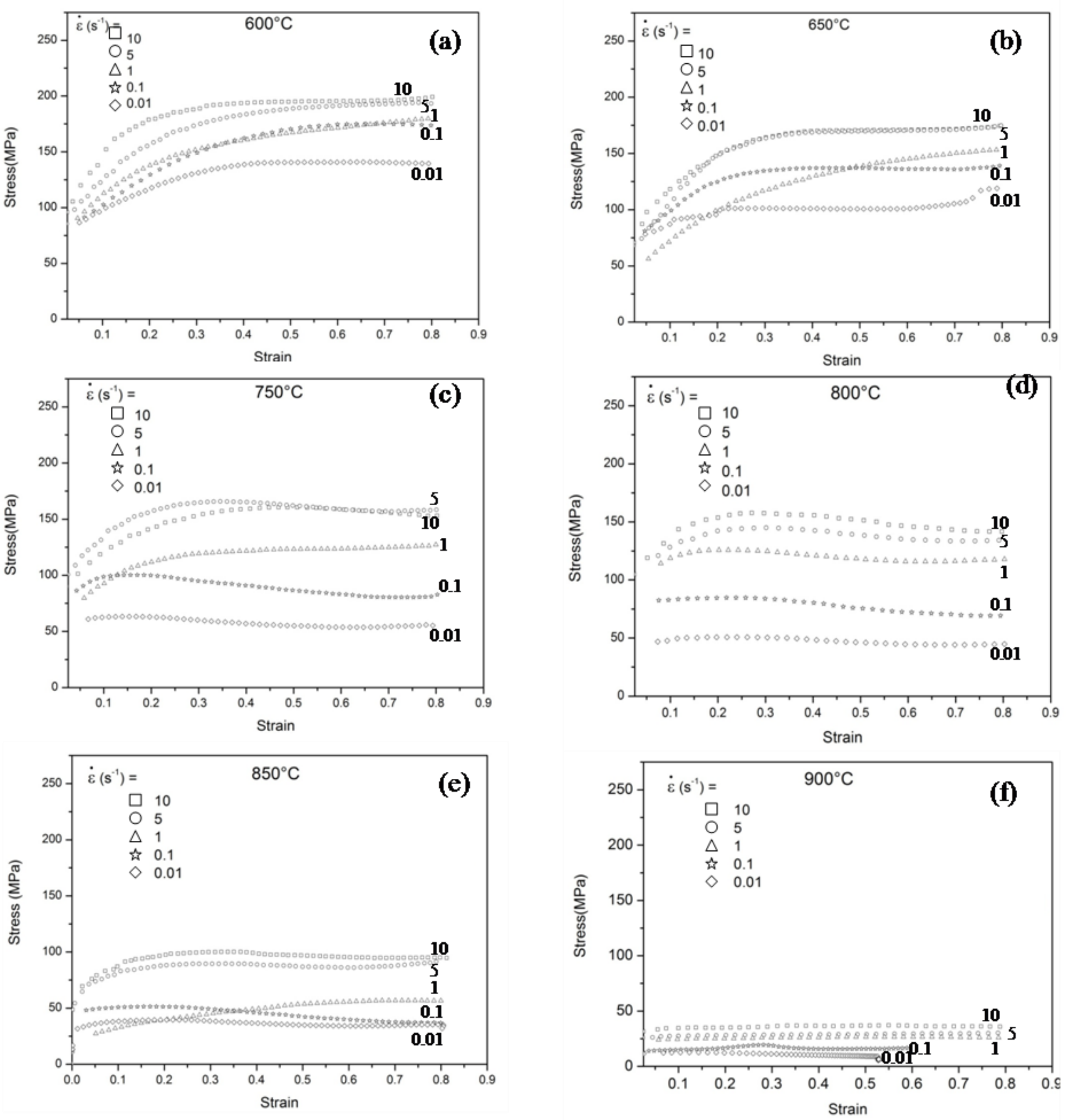

Fig. 4.1:The true stress-strain curves for the Zr-Sn alloy at different strain rates at temperatures of (a) 600° C, (b) 650° C, (c) 750° C, (d) 800° C, (e) 850° C and (f) 900°C.

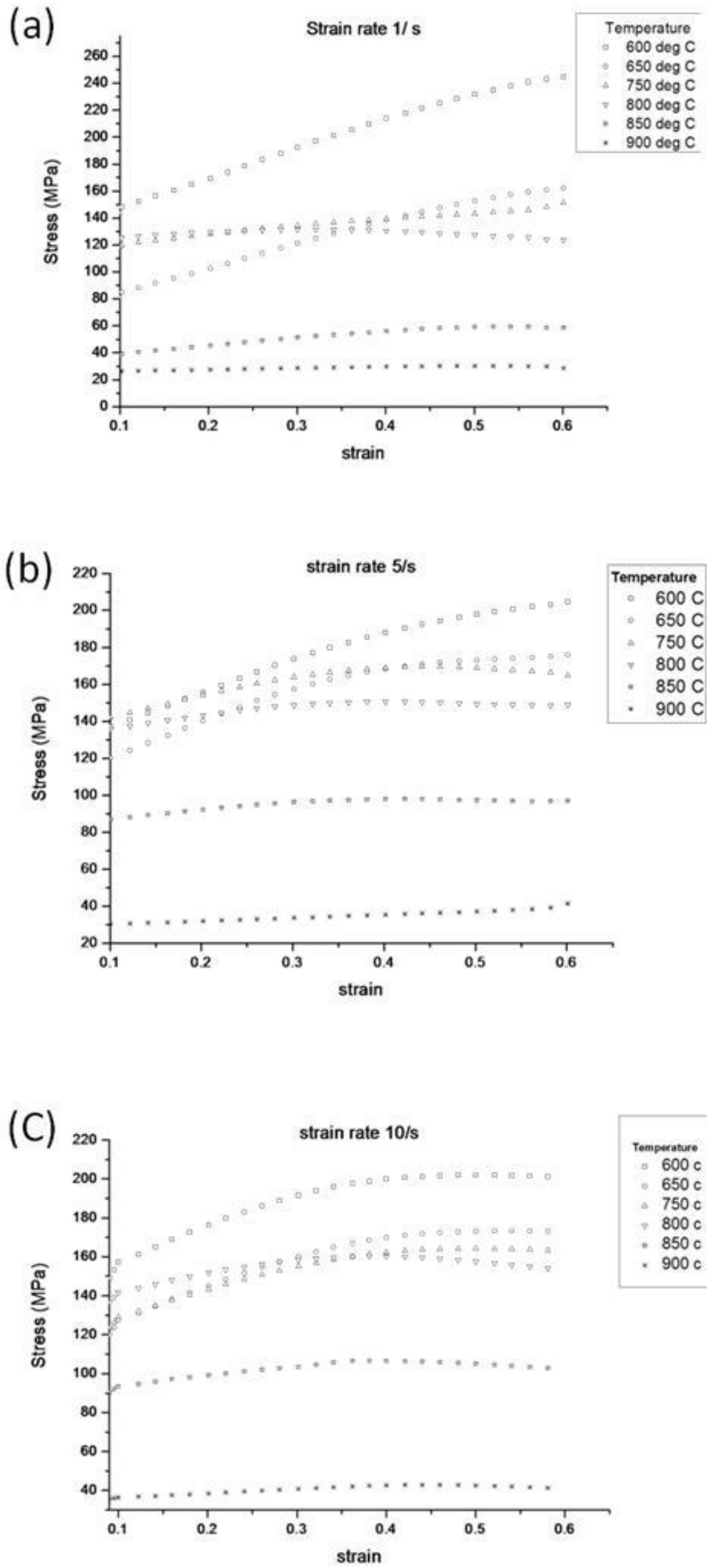

Fig 4.2 Stress–strain curves of Zr-Sn in at various temperatures and strain rates of (a) 1 s^{-1}, (b) 5 s^{-1}, (c) 10 s^{-1}

4.3. Microstructure evolution

4.3.1. Deformation at 600° C

At low strain rates (0.01 s^{-1} and 0.1 s^{-1}), the microstructure retained the as cast nature of the starting material (Fig 4.3). Very coarse grains typical of cast structure were seen in spite of heavy deformation. This indicates incomplete or insufficient grain fragmentation and essentially no recrystallization at these strain rates. As the strain rate was increased beyond 1s^{-1}, more signatures of deformation (like grain fragmentation, relatively higher proportion of non indexed regions) could be seen. At high strain rates, some instances of deformation twinning could be seen. The analysis of the twins confirmed them to be of 85°<2-1-10> type, known as tensile twins. No recrystallized grains could be identified at any strain rates at this deformation temperature [28]. Thus the temperature of 600° C was seen to be insufficient to promote dynamic recrystallization.

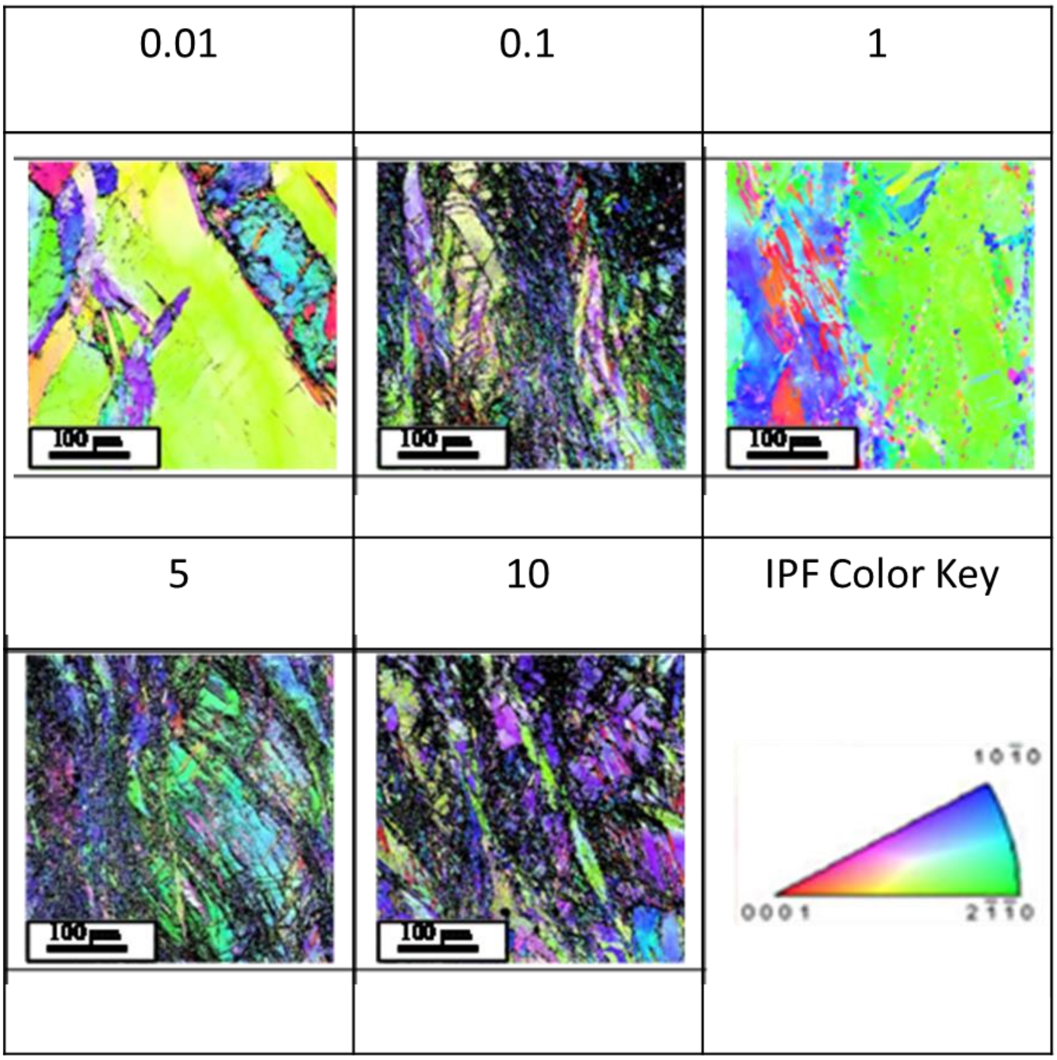

Fig4.3 The evolution of the microstructure after compression at different strain rates at 600 °C. RD and AD denote radial and axial directions respectively

4.3.2. Deformation at 650° C

The evolution of microstructure at different strain rates at 650° C, as seen in Fig. 4.4, was more or less similar to that observed at 600° C. The microstructure of the specimen deformed at 650°C at a strain rate of 0.01 s^{-1} showed a distinctly banded morphology. The banded structure showed fine dynamically recrystallized grains along with elongated deformed grains. Increase in the strain rate, however, lead to the formation of a microstructurewith features of significant remnant plastic deformation. These included, fine fragmented grains, low angle grain boundaries and high degree of in-grain misorientations. All of these features point towards lack of any appreciable dynamic recrystallization at these strain rates. Further, the highest strain rate deformed sample at this temperature exhibited formation of deformation twins similar to those observed in the high strain rate deformed samples of 600°C. While twinning, in general is expected to be a low temperature phenomenon, present results show that even at temperatures as high as 650°C, noticeable twining can be obtained under high strain rates. One potential reason for the same is the insufficient thermal activation of the alternate slip systems (at this temperature) making the twinning necessary to accommodate the imposed high strain rates.

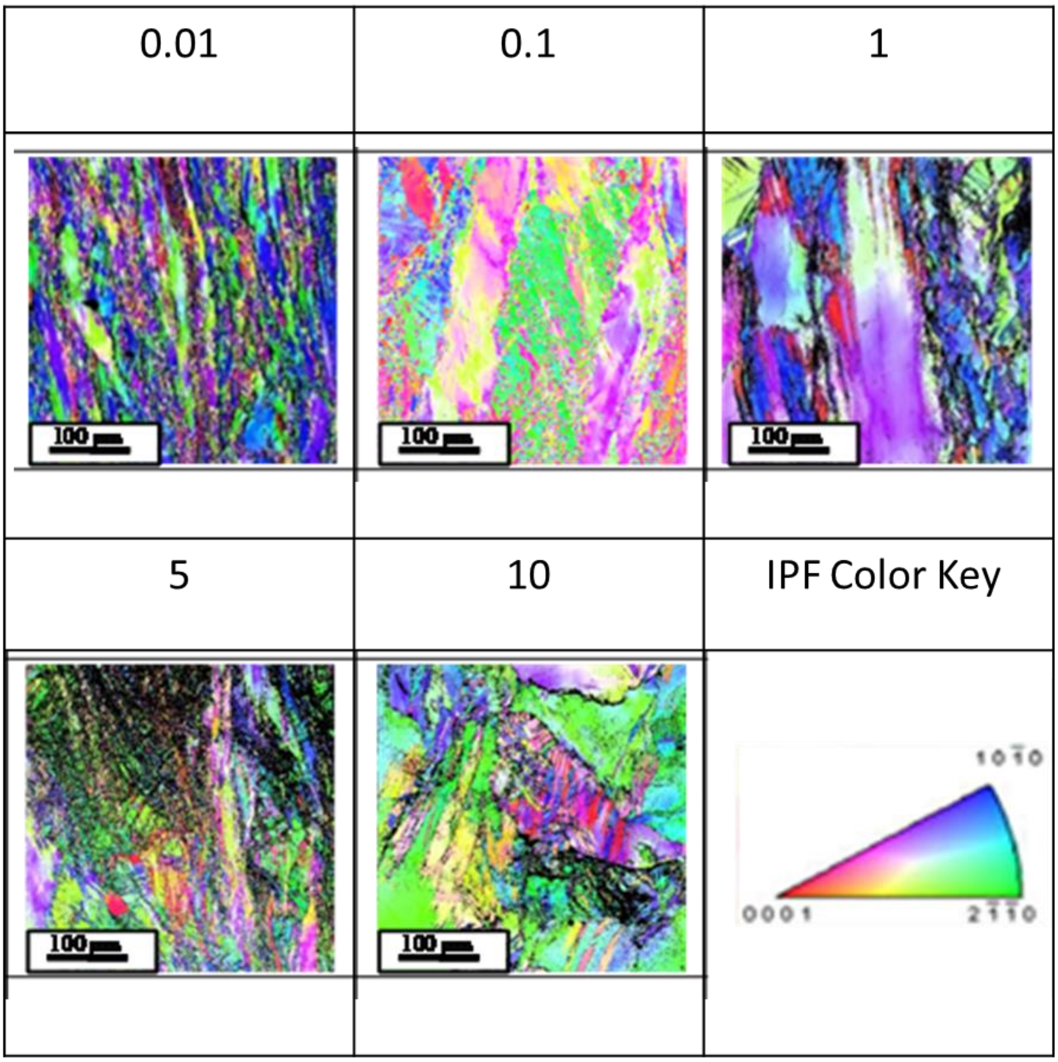

Fig 4.4The evolution of the microstructure after compression at different strain rates at 650 °C. RD and AD denote radial and axial directions respectively

The observation of signatures of recrystallization at lower strain rates but not at the higher ones has an important bearing on the suitability of this temperature for actual processing of the alloy. In general, optimized mechanical properties and ease of processing are achieved when the material undergoes dynamic recrystallization. In that context, present results indicate that while lower strain rates enable some degree of dynamic recrystallization, such recrystallization is not possible at higher strain rates at this temperature. This could be because the rate of generation of dislocations (due to deformation) at this temperature was much higher than the rate of recovery and recrystallization [28,29].

4.3.3. Deformation at 750° C

In contrast to the lower temperatures (600 and 650°C), dynamically recrystallized grains were distinctly observed throughout all strain rates at this deformation temperature. This observation has an important practical implication in terms of the processing of this alloy. During fabrication processes, the work-piece undergoes a series of complex stress states at any particular temperature and experiences a variety of strain rates, which vary throughout the work-piece as well as with time. An ideal working temperature should result in dynamic recrystallization over a wide regime of strain rates. This would lead to a relatively uniform microstructure throughout the sample. Hence, 750° C, based on the microstructural information generated in the present work, appears to be an optimum hot working temperature during fabrication (Fig 4.5).

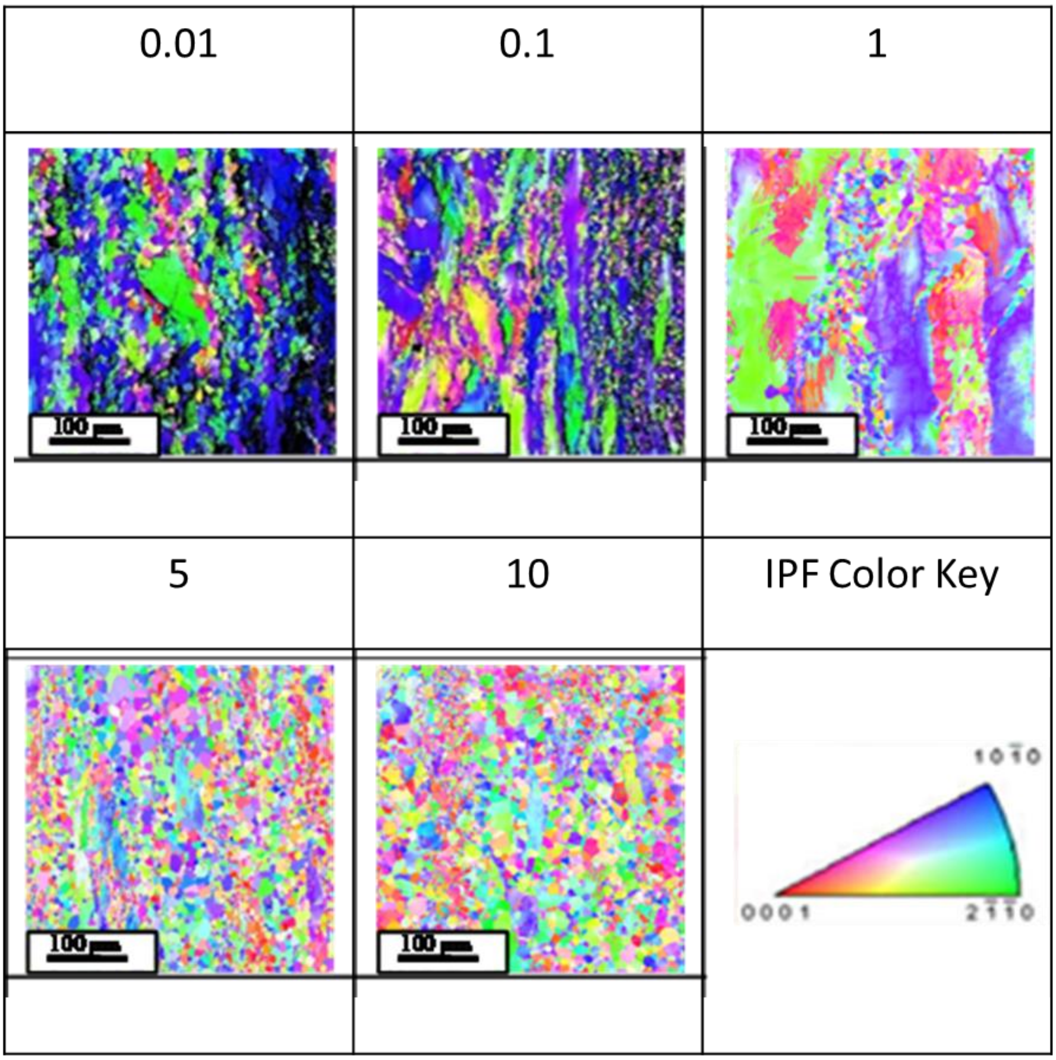

Fig 4.5 The evolution of the microstructure after compression at different strain rates at 700 °C. RD and AD denote radial and axial directions respectively

4.3.4. Deformation at 800° C

Deformation at 800° C resulted in a microstructure which was recrystallized and had a banded morphology (Fig 4.6). The banded nature was more predominant at lower strain rates. At higher strain rates, the banded structure was progressively replaced by equiaxed grains. This could be attributed to a greater driving force for recrystallization as a result of higher dislocation build-up. Application of higher strain rates led to the refinement of the microstructure, on account of more nucleation events. Comparison with the microstructure evolution at 750° C clearly shows that at higher temperatures, higher strain rates were required for the generation of a dynamically recrystallized microstructure.

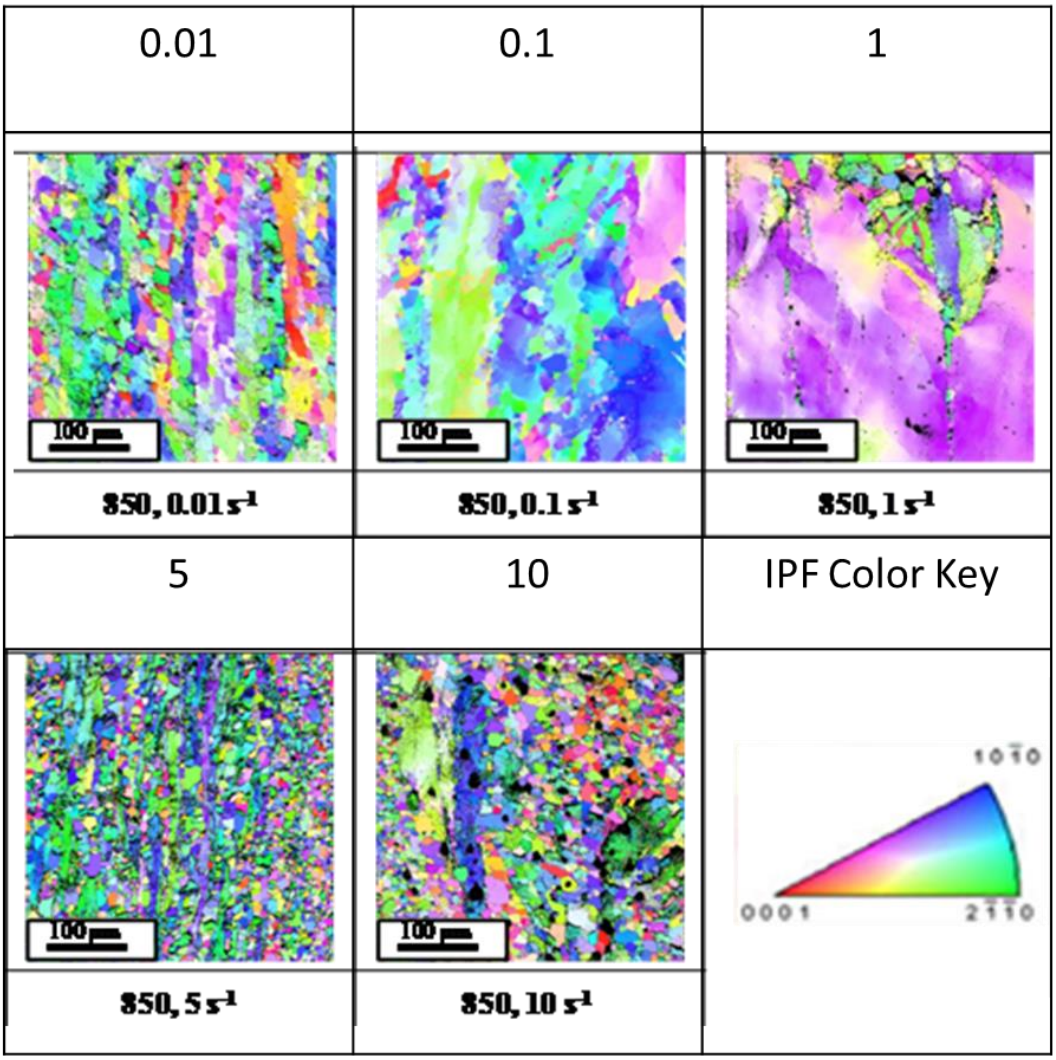

Fig 4.6 The evolution of the microstructure after compression at different strain rates at 800 °C. RD and AD denote radial and axial directions respectively

4.3.5. Deformation at 850° C

The microstructure evolved at 850° C was similar to that developed at 800° C. The higher temperature, however, led to visibly coarse grains (Fig 4.7). At 850° C, the banded morphology that was developed distinctly at lower strain rates was retained at higher strain rates as well, unlike the case of 800° C.While dynamic recrystallization at 800° C at 10 s^{-1} could remove the banded morphology completely, the softness of the material at 850° C appears to have resulted in the retention of the banded morphology.

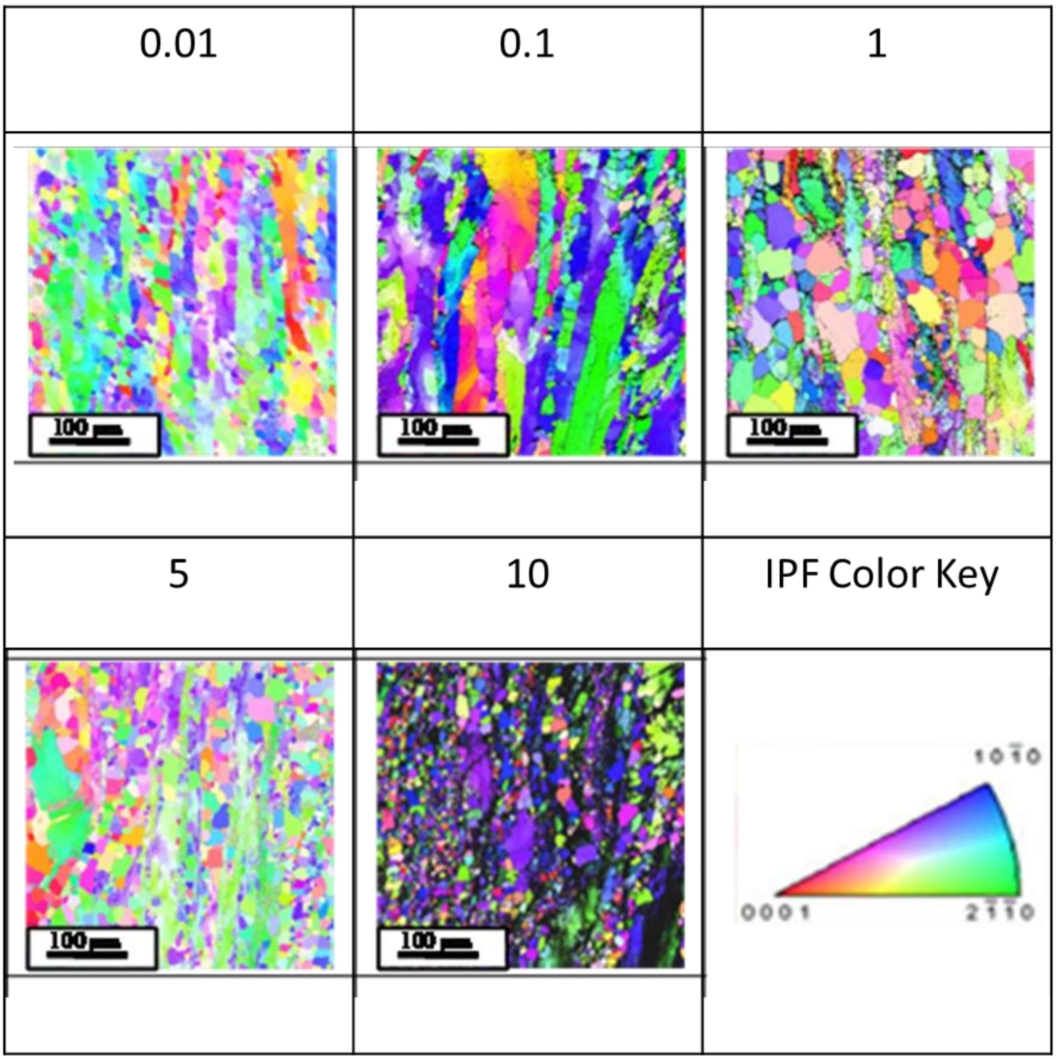

Fig 4.7 The evolution of the microstructure after compression at different strain rates at 850 °C. RD and AD denote radial and axial directions respectively

4.3.6. Deformation at 900° C

At lower strain rates, the microstructure was essentially composed of β → α transformation variants [30] in a typical Widmanstatten morphology, signifying no appreciable dynamic recrystallization. Increase in the strain rate resulted in the breakdown of the transformation microstructure and the generation of an increasing proportion of equiaxed grains. A glance at the series of microstructures evolved at the strain rates of 1 s^{-1} to 10s^{-1}, showed the sequential evolutionof equiaxed microstructure, see Fig 4.8. It could be seen that while the microstructure generated at 10 s^{-1} was fully equiaxed, the high temperature also resulted in rapid grain coarsening (grain diameter ~50 μm). Thus, a high strain rate was essential at this high temperature to generate sufficient stored energy to initiate dynamic recrystallization.

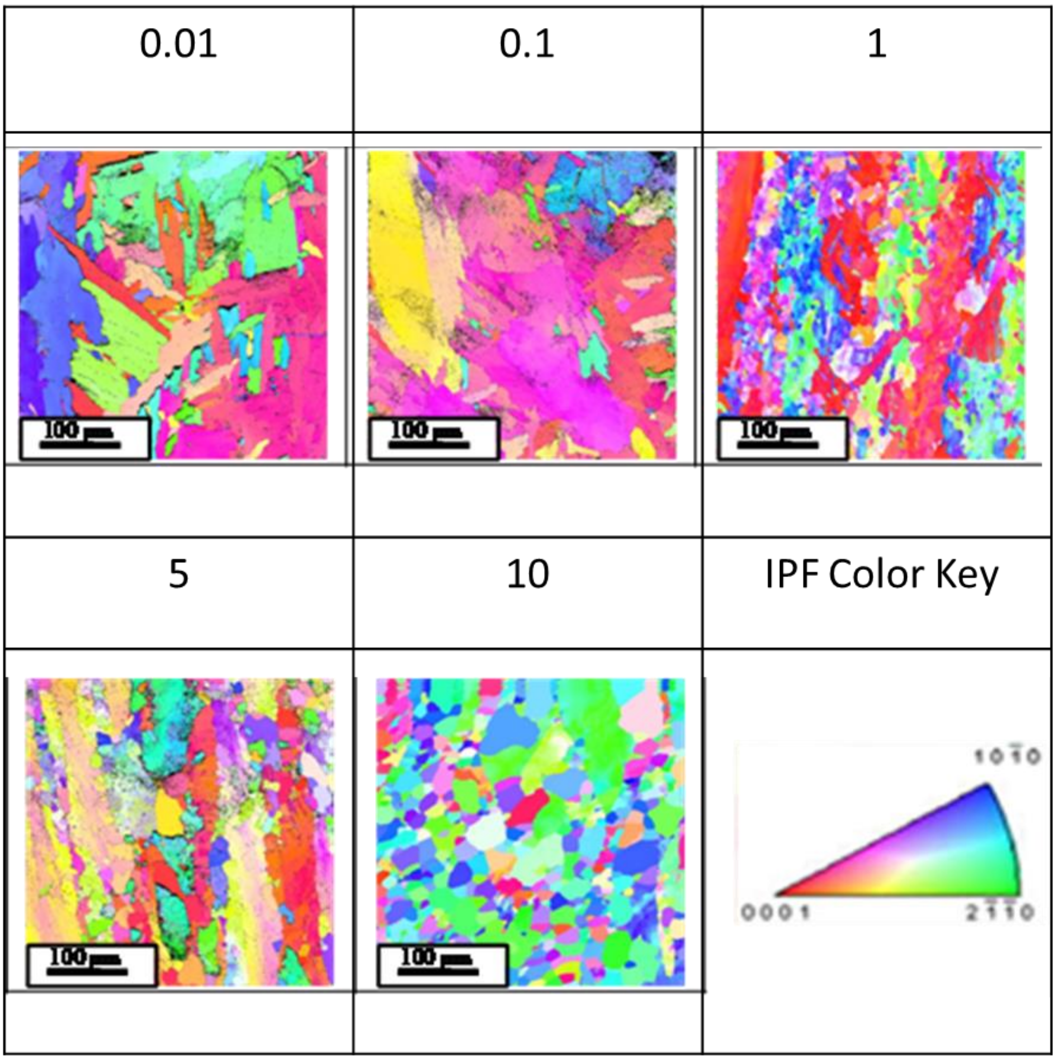

Fig 4.8 The evolution of the microstructure after compression at different strain rates at 900 °C. RD and AD denote radial and axial directions respectively

4.4. Texture evolution

The texture evolution, as depicted in Fig 4.9, can be broadly categorized into three temperature domains. These include domains where texture evolution is chiefly governed by deformation (600-650°C), dynamic recrystallization (750-850°C) and phase transformation (>850°C). The actual textural changes and possible micro-mechanisms for the same are discussed briefly below.

- The texture evolution behaviour in the temperature range of 600-650°C was a typical deformation texture of the Zr alloys. Basal poles were observed to have relatively higher concentration along the radial directions of the compression samples at all the strain rates considered. This behaviour may be contrasted with that of the typical room temperature deformation texture evolution. In the latter case, basal poles typically move towards the principal compression axis of the sample on account of operation of tensile twins [31]. Since the temperature of deformation, is quite high, the propensity for the twining is rather low [32] (as also confirmed by the microstructures in Fig 4.3 & 4.4) and hence no significant basal pole concentration along axial direction (principal compression direction in the present case) could be seen.
- Texture evolution in the temperature domain of 750-850°C has been observed to be characterized by the presence of strong texture components which were not observed in the samples deformed in the lower temperature domain. The origin of such texture components can be traced to the occurrence of dynamic recrystallization as revealed by the corresponding microstructures, see Fig 4.4. Since the recrystallized grains can have orientations distinctly different from the parent grains (oriented nucleation phenomenon) [33], the resulting final texture had several strong texture components far away from radial as well axial directions. This is in sharp contrast to samples deformed

in low temperature domain where no significant recrystallization could be seen, see Fig 4.3. Another point of note is the stronger dependence of final texture on the strain rate in this temperature domain, see Fig 4.4. This can be attributed to the fact that texture evolution in this temperature regime is chiefly governed by the extent of dynamic recrystallization, which in turn is a strong function of the strain rate as also confirmed by the respective microstructures shown in Fig 4.4 to 4.5.

- The texture evolution for the case of high temperature (>850°C) deformation has been seen to be dictated by the phase transformation. Presence of large number of strong individual texture components, in sharp contrast to the lower temperature domains, is the reason for this assertion. Transformation of β phase to α phase typically involves formation of multiple variants which result in the formation of several individual texture components as observed here [30,34]. In spite of the fact that significant deformation accompanied the phase transformation, the nature of observed texture confirms the prevalence of transformation induced texture over that of deformation induced texture.

(a)

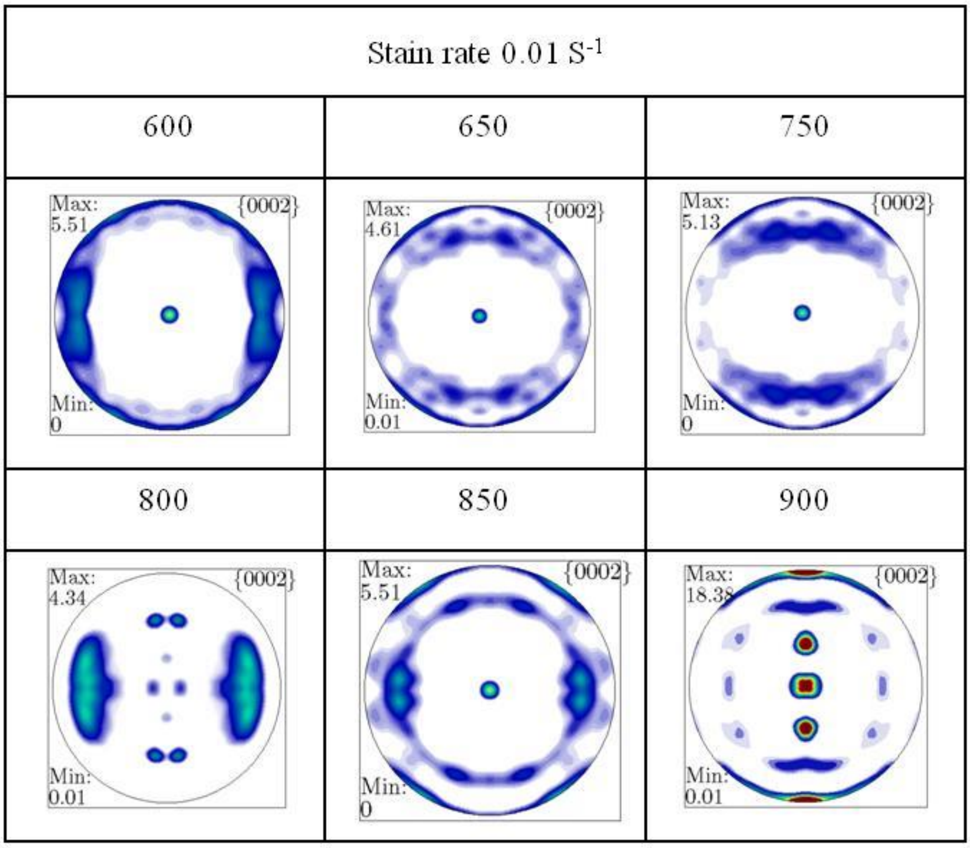
Stain rate 0.01 S-1
600
650
750
Max: 5.51
{0002}
Min: 0
Max: 4.61
{0002}
Min: 0.01
Max: 5.13
{0002}
Min: 0
800
850
900
Max: 4.34
{0002}
Min: 0.01
Max: 5.51
{0002}
Min: 0
Max: 18.38
{0002}
Min: 0.01

(b)

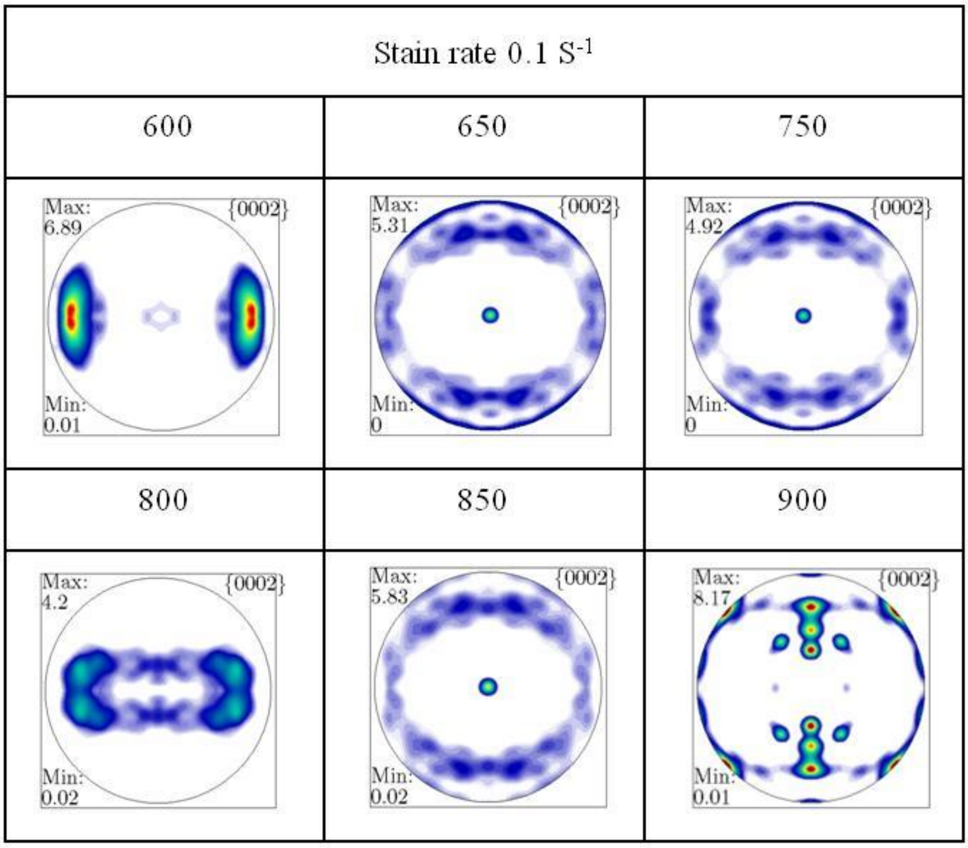
Stain rate 0.1 S-1
600
650
750
Max: 6.89
{0002}
Min: 0.01
Max: 5.31
{0002}
Min: 0
Max: 4.92
{0002}
Min: 0
800
850
900
Max: 4.2
{0002}
Min: 0.02
Max: 5.83
{0002}
Min: 0.02
Max: 8.17
{0002}
Min: 0.01

(c)

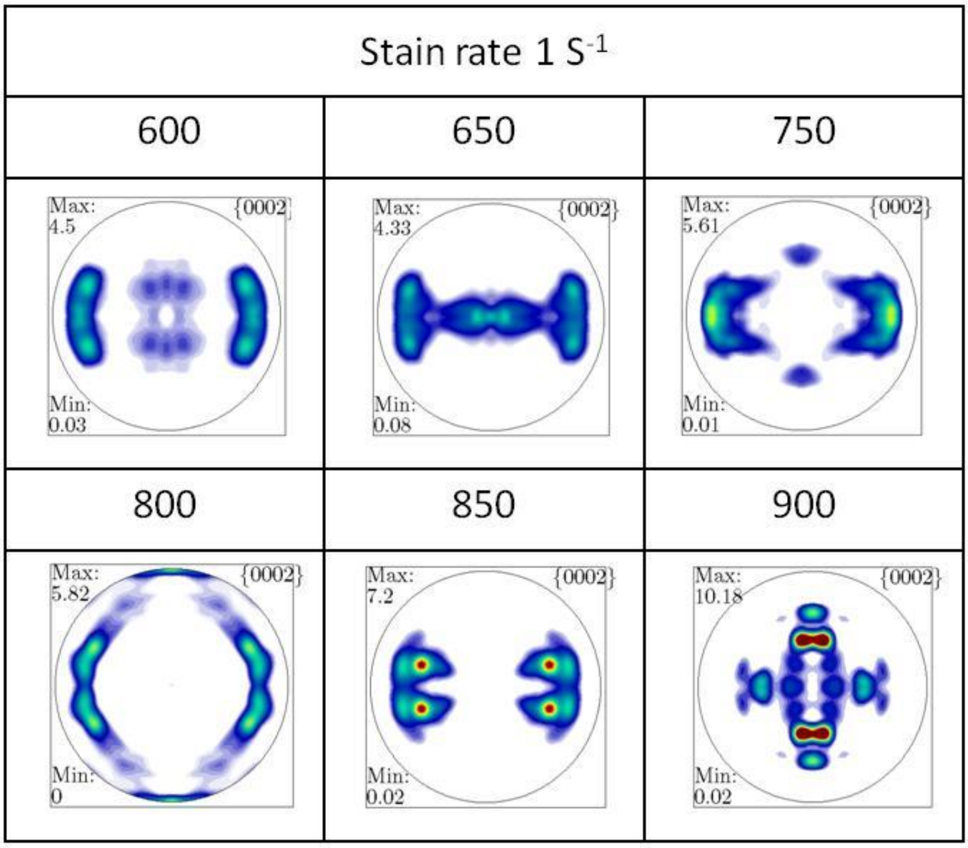
Stain rate 1 S-1
600
650
750
Max: 4.5
{0002}
Min: 0.03
Max: 4.33
{0002}
Min: 0.08
Max: 5.61
{0002}
Min: 0.01
800
850
900
Max: 5.82
{0002}
Min: 0
Max: 7.2
{0002}
Min: 0.02
Max: 10.18
{0002}
Min: 0.02

(d)

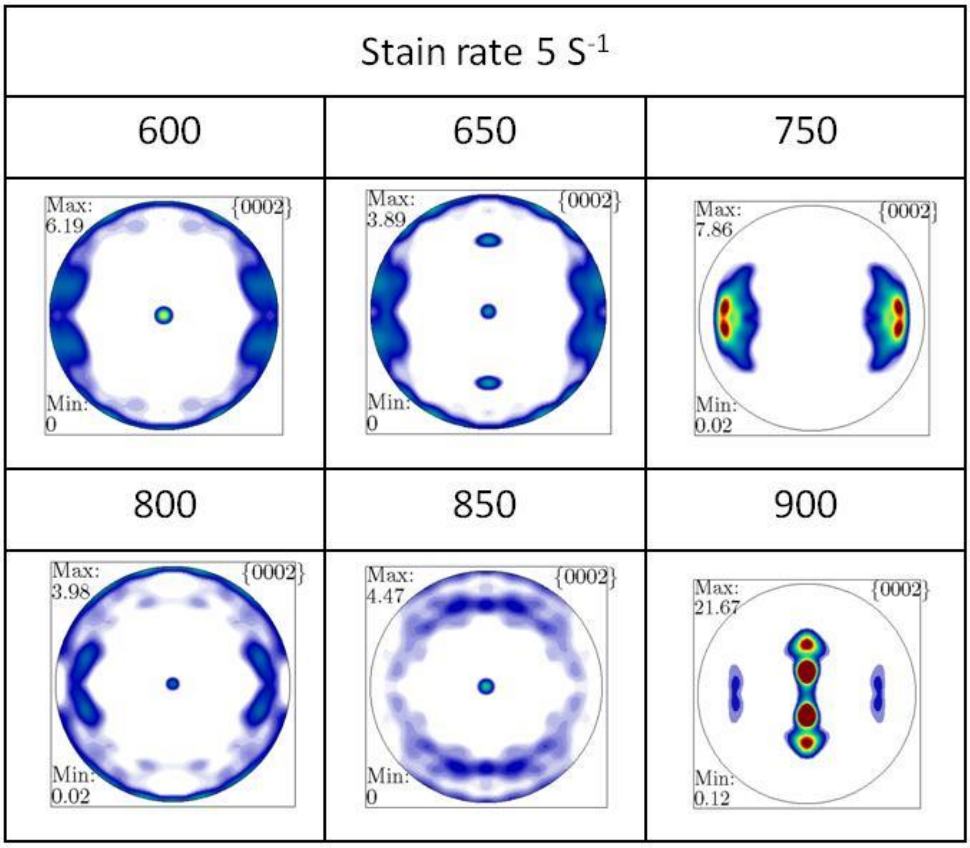
Stain rate 5 S-1
600
650
750
Max: 6.19
{0002}
Min: 0
Max: 3.89
{0002}
Min: 0
Max: 7.86
{0002}
Min: 0.02
800
850
900
Max: 3.98
{0002}
Min: 0.02
Max: 4.47
{0002}
Min: 0
Max: 21.67
{0002}
Min: 0.12

(e)

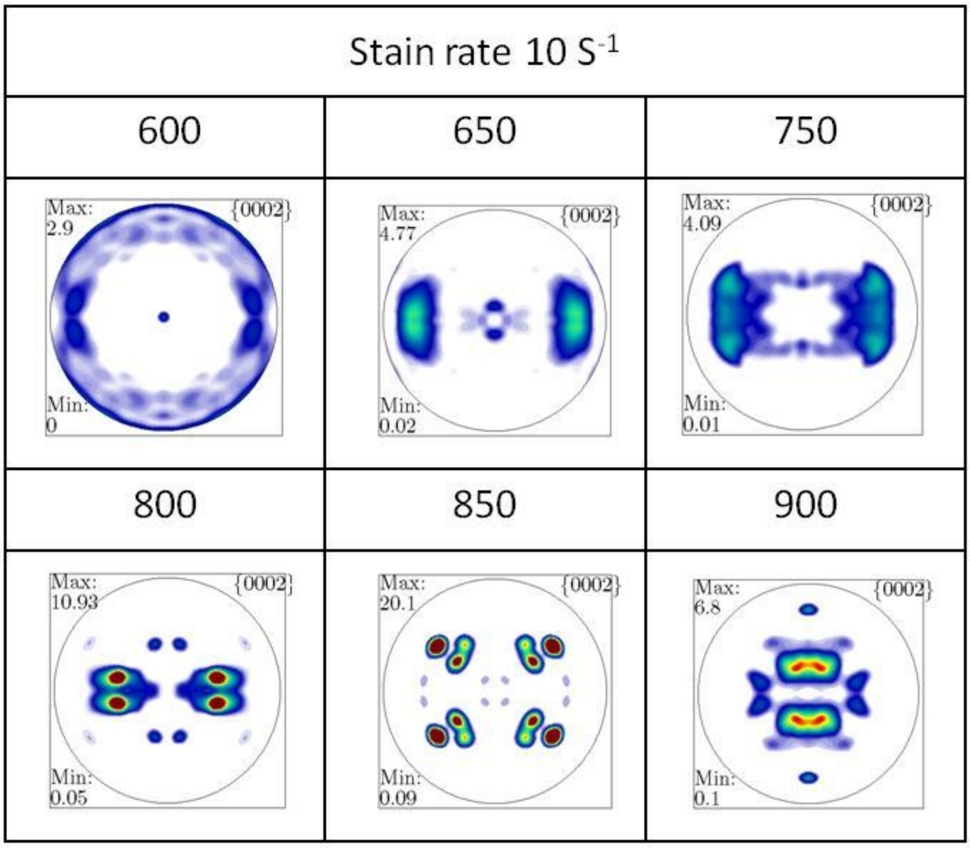

Fig 4.9: The evolution of the bulk texture after compression at different strain rates and temperatures. RD and AD denote radial and axial directions respectively.

4.5. Summary

The flow behaviour along with microstructural and textural analysis of hot compressed samples of Zr-0.3% Sn samples was carried out in this study. The deformation conditions, viz., temperature and strain rate, were seen to have a strong effect on the flow behaviour and resultant microstructure and texture.

1. Noticeable work hardening was observed in the deformation at temperatures below 750°C, with no signatures of dynamic recrystallization in the corresponding microstructures.
2. Dynamic recrystallization was seen to occur at 750° C and above, with the microstructure showing recrystallized grains and the flow curves displaying no appreciable work hardening.
3. At 900° C, the microstructure changed from the Widmanstatten structure of β to α transformation variants to equiaxed grains as the strain rate was increased. A high strain rate of 10 s^{-1} was found to be required result in complete dynamic recrystallization, overriding the microstructural features of β → α phase transformation.

Based on the present results, the temperature of 750° C appears to provide a wide margin of possible strain rates at which equiaxed recrystallized microstructure could be obtained and hence, this temperature may be deemed suitable for hot working processes. The implication of this, in the context of hot working stage of cladding fabrication, is that no drastic changes in process parameters need to be invoked for duplex clad fabrication in comparison with the conventional single cladding, where a temperature of 825°C [24] is employed in the hot extrusion stage.

4.6. References

[1] E.F. Ibrahim, R. Choubey, J.J. Jonas, Effect of texture and heat treatment on high temperature deformation of Zircaloy-2, J. Nucl. Mater. 126 (1984) 44–52.

[2] G. Sudhakar Rao, J.K. Chakravartty, S. Nudurupati, G.S. Mahobia, K. Chattopadhyay, N.C. Santhi Srinivas, V. Singh, Low cycle fatigue behavior of Zircaloy-2 at room temperature, J. Nucl. Mater. 441 (2013) 455–467.

[3] K. Linga Murty, I. Charit, Texture development and anisotropic deformation of zircaloys, Prog. Nucl. Energy. 48 (2006) 325–359.

[4] S.K. Sahoo, V. Hiwarkar, I. Samajdar, G. Dey, D. Srivastav, R. Tiwari, S. Banerjee, Heterogeneous deformation in single-phase Zircaloy 2, Scr. Mater. 56 (2007) 963–966.

[5] D.O. Northwood, Gamma and delta hydrides in zirconium alloys, J. Common Met. 48 (1976) 173–175.

[6] M. Griffiths, A review of microstructure evolution in zirconium alloys during irradiation in zircon, J. Nucl. Mater. 159 (1988) 190–218.

[7] D.O. Northwood, The development and applications of zirconium alloys, Mater. Des. 6 (1985) 58–70.

[8] P. Mishra, D.N. Sah, S. Kumar, S. Anantharaman, Microstructural examination of high temperature creep failure of Zircaloy-2 cladding in irradiated PHWR fuel pins, J. Nucl. Mater. 429 (2012) 257–262..

[9] G. Choudhuri, D. Srivastava, K.R. Gurumurthy, B.K. Shah, Optimization of stress relief heat treatment of PHWR pressure tubes (Zr–2.5Nb alloy), J. Nucl. Mater. 383 (2008) 178–182..

[10] B. Cox, Pellet-clad interaction (PCI) failures of zirconium alloy fuel cladding — A review, J. Nucl. Mater. 172 (1990) 249–292. .

[11] M. Fregonese, G. Delette, G. Ducros, F. Lefebvre, Amount of iodine responsible for I-SCC of Zircaloy-4 in PCI-conditions: recoil-implanted and thermally released iodine, Nucl. Eng. Des. 186 (1998) 307–322..

[12] N. Marchal, C. Campos, C. Garnier, Finite element simulation of Pellet-Cladding Interaction (PCI) in nuclear fuel rods, Comput. Mater. Sci. 45 (2009) 821–826..

[13] G.V. Ranjan, E. Smith, Determination of stress within ZIRCALOY cladding due to pellet-cladding interaction, Nucl. Eng. Des. 56 (1980) 263–272.

[14] T. Alam, M.K. Khan, M. Pathak, K. Ravi, R. Singh, S.K. Gupta, A review on the clad failure studies, Nucl. Eng. Des. 241 (2011) 3658–3677.

[15] S. Xia, Z. Wang, T. Yang, Y. Zhang, Irradiation Behavior in High Entropy Alloys, J. Iron Steel Res. Int. 22 (2015) 879–884.

[16] S.Q. Xia, X. Yang, T.F. Yang, S. Liu, Y. Zhang, Irradiation Resistance in Al x CoCrFeNi High Entropy Alloys, JOM. 67 (2015) 2340–2344.

[17] H.S. Rosenbaum, R.A. Rand, R.P. Tucker, B. Cheng, R.B. Adamson, J.H. Davies, J.S. Armijo, S.B. Wisner, Zirconium-Barrier Cladding Attributes, in: Zircon. Nucl. Ind. Seventh Int. Symp. ASTM STP 939, 1987: pp. 675–699.

[18] H.S. Rosenbaum, J.S. Armijo, J.H. Dayies, R.P. Tucker, Development of Zr-Barrier Fuel, in: Embrittlement Liq. Solid Met. Metall. Soc. AIME, 1984: pp. 457–471.

[19] J.S. Armijo, L.F. Coffin, H.S. Rosenbaum, Development of Zirconium-barrier fuel cladding, in: A.N. Garde, E.R. Bradley (Eds.), Zircon. Nucl. Ind. Tenth Int. Symp. ASTM STP 1245, Philadelphia, 1994: pp. 3–18.

[20] R. Krishnan, M.K. Asundi, Zirconium alloys in nuclear technology, in: Proc. Indian Acad. Sci. Sect. C Eng. Sci., 1981: pp. 41–56.

[21] H.G. Rickover, L.D. Geiger, B. Lustman, History of the Development of Zirconium Alloys for use in Nuclear Reactors, in: IAEA, 1975.

[22] S. Kass, The Development of the Zircaloys, ASTM STP-368. (1964).

[23] A.M. Garde, G.R. Smith, R.C. Pirek, In-PWR Irradiation Performance of Dilute Tin-Zirconium Advanced Alloys, in: Zircon. Nucl. Ind. Thirteen. Int. Symp. ASTM STP 1423, 2002: pp. 490–506.

[24] K.V.M. Krishna, S.K. Sahoo, I. Samajdar, S. Neogy, R. Tewari, D. Srivastava, G.K. Dey, G.H. Das, N. Saibaba, S. Banarjee, Microstructural and textural developments during Zircaloy-4 fuel tube fabrication, J. Nucl. Mater. 383 (2008) 78–85.

[25] K. Vaibhaw, S.V.R. Rao, S.K. Jha, N. Saibaba, R.N. Jayaraj, Texture and hydride orientation relationship of Zircaloy-4 fuel clad tube during its fabrication for pressurized heavy water reactors, J. Nucl. Mater. 383 (2008) 71–77.

[26] T. Wakui, J. Malzbender, R.W. Steinbrech, Mechanical testing of thermally stressed materials with rough interfaces: Mechanically induced delamination cracking in thermal barrier composites, Surf. Coat. Technol. 200 (2006) 5419–5426.

[27] B. Cox, Some thoughts on the mechanisms of in-reactor corrosion of zirconium alloys, J. Nucl. Mater. 336 (2005) 331–368.

[28] J.K. Chakravartty, S. Banerjee, Y.V.R.K. Prasad, M.K. Asundi, Hot-working characteristics of Zircaloy-2 in the temperature range of 650–950°C, J. Nucl. Mater. 187 (1992) 260–271.

[29] Z.N. Yang, F.C. Zhang, Y.Y. Xiao, Z.G. Yan, Dynamic recovery : The explanation for strain-softening behaviour in Zr – 2 . 3Nb alloy, Scr. Mater. 67 (2012) 959–962.

[30] R.A. Holt, The Beta to Alpha Phase Transformation in Zircaloy-4, J. Nucl. Mater. 35 (1970) 322–334.

[31] E. Tenckhoff, Deformation mechanisms, texture, and anisotropy in Zirconium and Zircaloy, in: ASTM STP 966 Phila. PA, 1988: p. 3.

[32] D.G. Westlake, TWINNING IN ZIRCONIUM, Acta Metall. 9 (1961) 327–331.

[33] H. Hu, TEXTURE OF METALS, Texture. 1 (1974) 233–258.

[34] M. Sattari, R.A. Holt, M.R. Daymond, Variant selection and transformation texture in zirconium alloy Excel, J. Nucl. Mater. 453 (2014) 120–123.

Chapter 5

Development of Processing Map and Constitutive Behaviour of Zr-03Sn Alloy

Preamble: Using hot deformation results, ie stress vs strain curves processing maps have been generated. Processing map developed based on dynamic materials model has different domains of deformation efficiency and microstructural studies carried out in lower and higher efficiency domain shows fully recrystallised and unstable microstructure respectively. Constitutive flow behaviour also studied and strain compensated constitutive equations have been made.

5.1. Introduction

The Zr-barrier cladding tubes are manufactured by co-extruding composite tube shell of Zircaloy with a liner of dilute Zirconium Tin alloy at elevated temperatures. High temperature deformation of zirconium and zirconium alloys is a complex process where both the work hardening and dynamic softening phenomena occur simultaneously. In addition to deformation parameters, such as the strain rate, degree of deformation and temperature, chemical composition and microstructure prior to deformation influence these phenomena significantly, which dictate the quality of the product. In addition to intrinsic variables, extrinsic factor, like forming process used, also decides the quality of the product. In the production of the co-extruded tube shell, deformation parameters need to be optimized in terms of strain-rate and temperatures that the interface between the two materials could be identified solely by the variation in chemical composition upon moving from Zirconium tin alloy to Zircaloy [1]. Such a characteristic indicates formation of good metallurgical bond which is a necessity for achieving good service performance of the composite tube.

Achievement of such bond requires optimum processing conditions which in turn require knowledge of flow behavior (like constitutive equations of deformation) of the individual alloy layers in question. Objective of this study is to develop a constitutive equation where combined effect of stress, strain rate, temperature and other process parameters can be represented in the form of a constitutive equation.

In this chapter deformation behavior of the cast Zr - 0.3 Sn alloy with respect to micro-structural stability is explained using power dissipation maps generated on the basis of the Dynamic Materials Model (DMM). Power dissipation map is developed using thermo-mechanical data generated using thermo-mechanical simulator, which systematically explain the influence of temperature and strain rate on the constitutive flow behavior of cast Zirconium tin alloy. Power dissipation map is also known as Iso-efficiency maps which identifies the domain of hot deformation which indicates the type of microstructure which is possible to obtain during hot-working of cast alloy, and output from this can be used to identify the different metallurgical processes such as dynamic recovery, dynamic recrystallisation, flow instability etc. occurring in the various temperature –strain rate regimes. Information is useful mainly for bulk deformation processes wherein there is need to know the deformation behavior of cast structure. As cast Zirconium tin alloy samples were taken from double melted ingot using vacuum arc remelting (VAR) for hot deformation studies. Thermomechanical properties obtained were analysed to develop processing map. For optimization for process parameters simulation studies has been carried out using hot deformation data. As the deformation mechanism of Zirconium based alloys are complex process where mechanism changes with not only change in temperature and strain rate but also with strain. Therefore, there is need to have a constitutive equation of alloy which can be used for entire domain of deformation range and fit into standard FEM based simulation technique used for bulk deformation process. Hot deformation studies of as cast Zirconium Sn alloy has been carried out using thermos-mechanical simulator. The flow stress data obtained at different temperatures, strain rates and strain were used to develop the constitutive equation. Constitutive equation thus obtained has been used as material flow equation in development of Finite element based model for hot extrusion of a tubular product. Simulation results were also validated by extruding the tube made from Zr-Sn alloy billet.

The results obtained from this study can be used to find the combination of extrinsic and intrinsic variables that can be translated into metallurgical phenomena, such as dynamic recovery and dynamic recrystallization using these information it will be possible to optimise the process variables to obtain required microstructure for ZrSn alloy [1]. Dynamic material model developed using hot deformation data can be utilized to predict the mode of deformation. In earlier studies was done [3], to know the constitutive flow behavior of commercial purity wrought Zirconium, were studied using power dissipation maps generated on the basis of the Dynamic Materials. This Model [4-5] has been used in the present study. The model considers the work piece as a dissipater of power and calculates the efficiency of power dissipation through micro-structural changes in the work piece similar to an ideal linear dissipater. The deformation efficiency variation as a function of temperature and strain rate is used to identify type of deformation mechanism operative in thermo-mechanical processing. The processing map is qualitatively utilized to know the constitutive flow behavior of the material [6-9]. On the other hand, the numerical simulation has been widely applied in various metal forming processes to optimize the design of forming tools and process parameters [10–13]. In order to simulate the material flow behaviour under specified conditions, constitutive equation correlating the flow stress, strain, strain rate and deformation temperature becomes an interesting tool which can be used to predict the flow stress and even the microstructure evolution during hot forming processes.

5.2. Processing maps

A processing map is an explicit representation of the response of a material, in terms of microstructural mechanisms, to the imposed process parameters and consists of a superimposition of power dissipation and an instability map. Prasad et al. [5] assumed that there is no storage of energy in the material during deformation and instantly all the power converts irreversibly into two different forms, namely, thermal and microstructural changes. This model forms a bridge between the continuum mechanics and the microstructural mechanisms occurring during hot deformation, and consists of principles of irreversible thermodynamics of large plastic flow. The dissipated power is related to the rate of entropy production due to metallurgical processes obtained by partitioning the total power between the temperature rise and the microstructural change. In view of the viscoplastic nature of hot deformation, the strain rate sensitivity of flow stress has been found to be the power partitioning factor. Processing map contains superimposed power dissipation map and instability map.

5.2.1. Generation of Processing map

A process map is generated using data of flow stress as a function of temperature and strain rate over a wide range and these are best obtained using a hot compression test. The flow stress (σ) variation given by

$$\sigma = K\dot{\varepsilon}^{m} \qquad (5.1)$$

where K= constant

With strain rate ($\dot{\varepsilon}$) at a given temperature is curve fitted using a spline function and the strain rate sensitivity [$m = \partial(\text{In}\sigma)/\partial(\text{In}\dot{\varepsilon})$] is calculated as a function of strain rate. The efficiency of power dissipation given by

$$\eta = 2m/m+1, \tag{5.2}$$

Efficiency of power dissipation is calculated and plotted as a contour map in a frame of temperature and strain rate. The variation of efficiency of power dissipation with temperature and strain rate constitutes a power dissipation map, which exhibits various domains in which specific microstructure mechanisms occur.

The flow instability parameter that is microstructure related is given by

$$\xi(\dot{\varepsilon}) = \{\partial \text{ In } [m/(m+1)]/\partial \text{ In } \dot{\varepsilon}\} + m \tag{5.3}$$

$\xi(\dot{\varepsilon})$ is calculated and also plotted as a function of temperature and strain rate. The regime where it is negative will give flow instabilities. Such a plot is called an instability map. The physical meaning of above instability criterion is that if the system is not able to generate entropy at a rate that at least matches with the imposed rate, the system will localize the flow and cause flow instability.

5.3. Processing Map for Zr-0.3Sn alloy

The compression test of as cast Zr - 0.3 Sn alloys were carried out in thermo-mechanical simulator. The tests were performed in the temperature range of 600-900°C, strain rate varying from 1/s to 10/sec. The tests were carried out up-to maximum of 0.6 strain value. The results were already shown in previous chapter 4. Further Processing map of Zr- 0.3 Sn alloys was developed using that data.

Table 5.1: Flow stress (MPa) of Zr 0.3Sn alloy deformed at different temperature and strain rate:

Strain	**Strain Rate (s-1)**	**temperature (°C)**					
		600	**650**	**750**	**800**	**850**	**900**
	0.01	98	94	65	51	39	13
	0.1	103	99	100	84	51	15
	1	111	73	92	119	37	25
	5	125	107	129	129	81	27
0.1	**10**	146	117	124	143	83	35
	0.01	118	92	62	49	40	12
	0.1	129	125	100	85	50	17
	1	139	100	113	126	41	25
	5	157	148	157	142	90	28
0.2	**10**	185	149	144	155	98	35
	0.01	130	101	59	52	39	11
	0.1	149	133	95	84	49	16
	1	152	117	119	125	44	26
	5	173	163	166	145	93	28
0.3	**10**	189	162	158	157	101	36
	0.01	138	100	57	49	36	10
	0.1	163	139	91	82	47	15
0.4	**1**	159	130	122	121	50	26

0.4	5	183	168	166	141	89	29
	10	194	169	160	156	98	36
0.5	0.01	141	100	54	46	35	9
	0.1	170	137	89	77	41	16
	1	168	140	124	118	53	27
	5	190	170	163	139	86	29
	10	196	170	161	151	99	37
0.6	0.01	102	15.5	42	37	9	7.5
	0.1	185	52.6	83	33	16.3	12.3
	1	230	158	125	74	30	29
	5	222	174.5	140	109.5	40.5	34
	10	203	188	158	119	45.4	43.5

5.3.1. Validation of Processing Map

At low temperatures i.e. between 600^0C to 650^0C there is no stable region for deformation for any combination of temperature and strain rate. Microstructure of alloy deformed at 650^0C with strain rate of $1S^{-1}$ in figure 5.2 shows the localised flow of large cast grains surrounded by heavily deformed grains with presence of very high dislocation density. Non-uniformity of deformation takes place due to favourable orientation of few cast grains in direction of applied stress. Between 700^0C to 800^0C at low strain rates alloy deforms with high deformation efficiency, however, as strain rate increases beyond $1S^{-1}$ again deformation domain falls into instability region. This inconsistency in deformation behaviour is mainly due to presence of large columnar grains in cast Zr-0.3Sn alloy. With increase in temperature beyond 700^{0}C there is sufficient energy available to initiate the nucleation and growth of new grains. However, to deform the material with

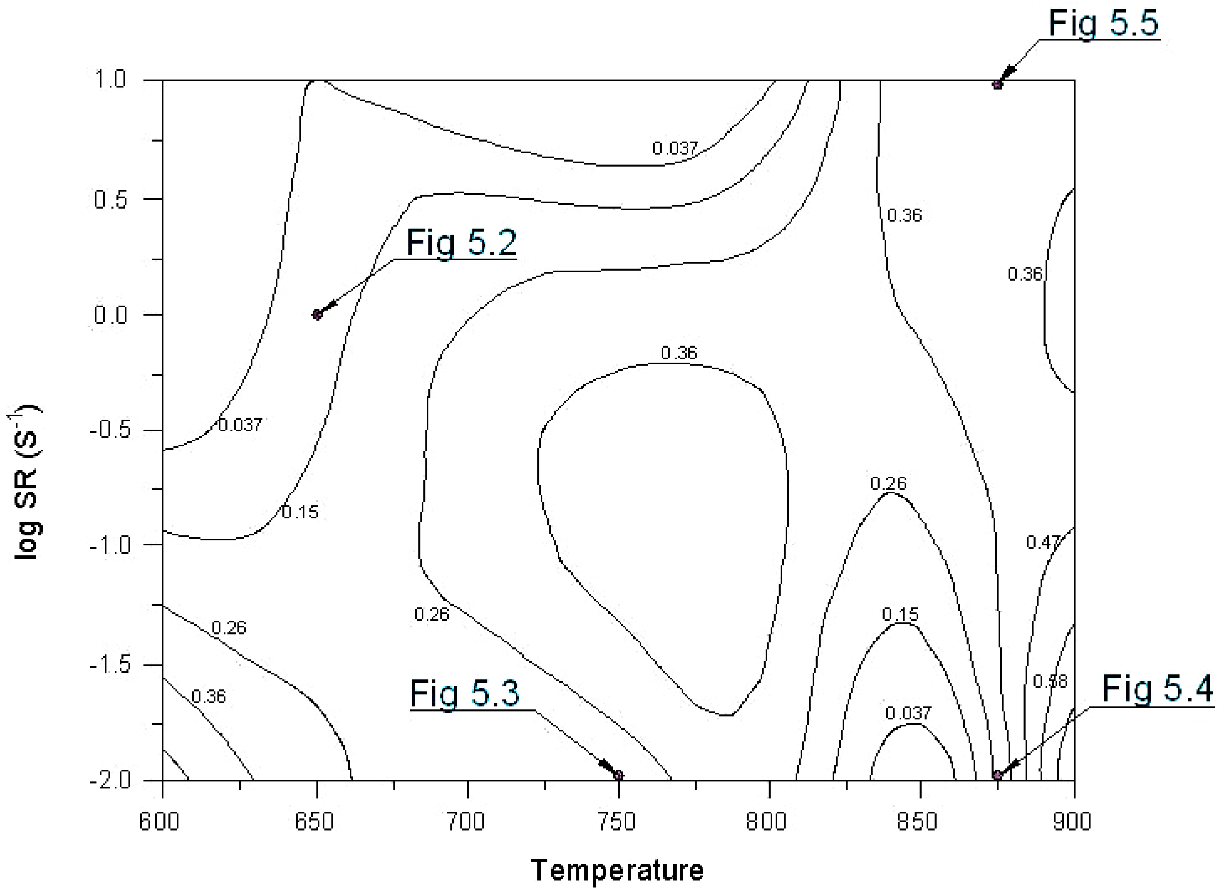

Fig. 5.1 Processing and Instability map of Zr Sn alloy at 0.6 strain

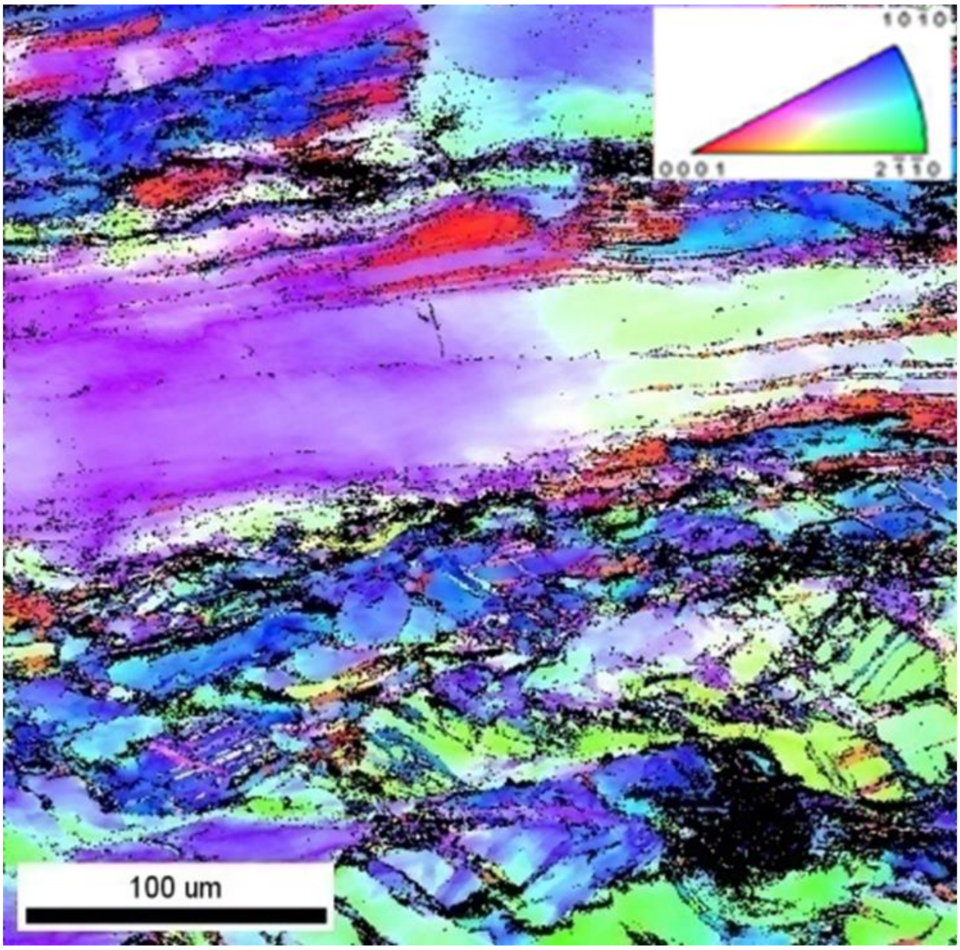

Fig 5.2 EBSD Micrograph of deformed Zr-0.3Sn alloy at 650^0C at strain rate of $1S^{-1}$.

Dynamic recrystallisation there is need for lower strain rate which will support nucleation and growth of new grains. Figure 5.3 shows fully recrystallised grains of Zr-0.3Sn alloy deformed at 750^0C at $0.01S^{-1}$ strain rate.

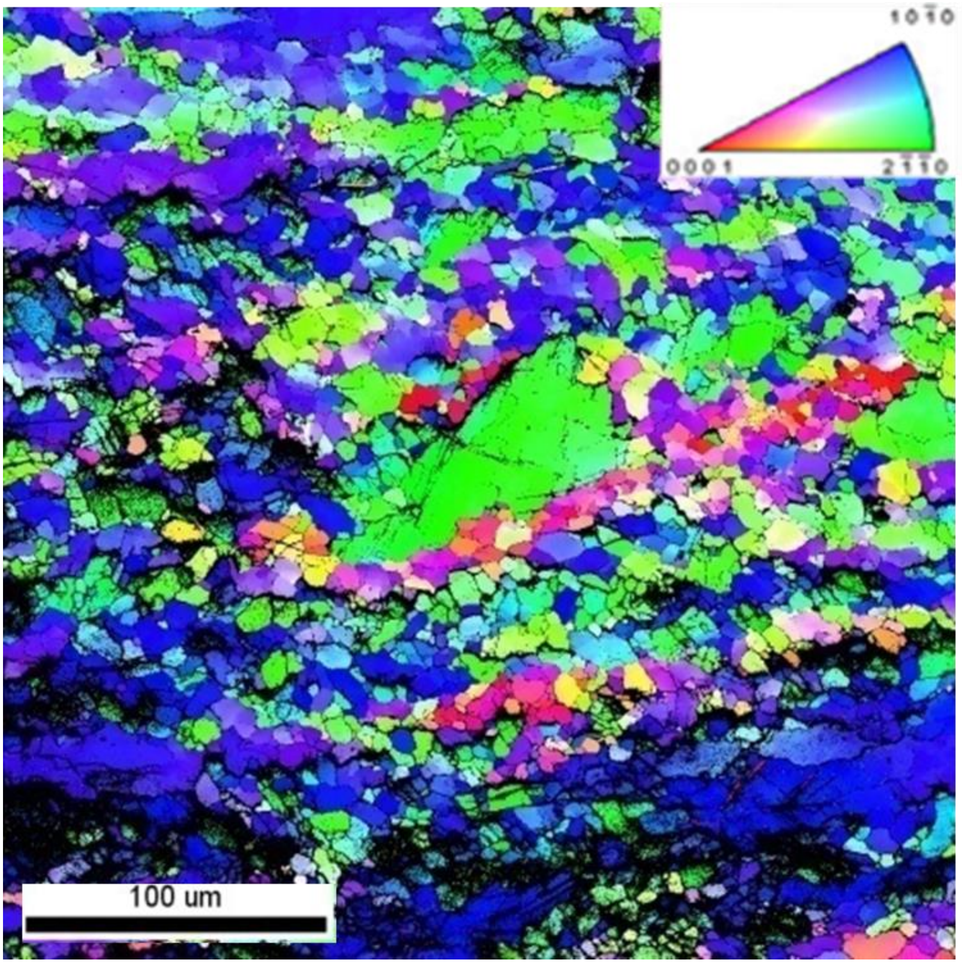

Fig. 5.3 Fully deformed and recrystallised microstructure of Zr-0.3Sn alloy deformed at 750^0C and $10^{-2}S^{-1}$.

The maximum efficiency of power dissipation is about 40 - 50 % for as castZr-Sn alloy obtained in the high temperature range between 875^0C-900^0Cwhich starts at low strain rate and continues upto very high strain rates Figure 5.4 (a) and (b) . Results indicate that fully recrystallised structure can be achieved by bulk deformation of this alloy at high strain rate and high temperature.

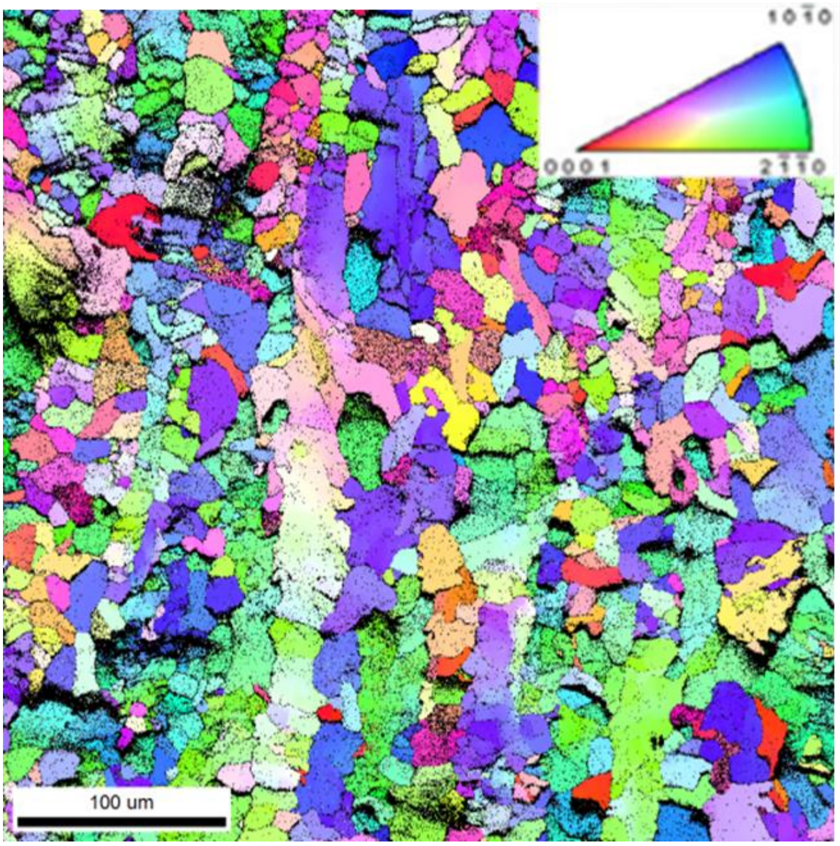

Fig. 5.4 (a) Fully deformed and recrystallised microstructure of Zr-0.3Sn alloy deformed at 875^{0}C and $10^{-2}S^{-1}$.

5.4. Constitutive Equation

Results obtained from deformation maps and flow stress obtained from stress strain curve clearly shows that microstructure developed during deformation is highly sensitive to strain rates and temperature. The information available from processing maps are quite helpful in identification of safe and unsafe domains for deformation. However, this information is of limited significance in bulk deformation processes such as extrusion and forging where quite complex deformation conditions exist. Parameters in these processes need number of information such as effect of ram velocity on strain rate variation, generation of temperature due to deformation along the cross section, effect of tool geometry on deformation pattern in the product and many more such information which is useful especially in case of co-extrusion. Constitutive modelling of alloy with processing maps can be used for realistic analysis of the deformation behaviour of the material. Constitutive modelling is a technique which has been used for number of materials and models have been verified with experimental results of flow[18-20].

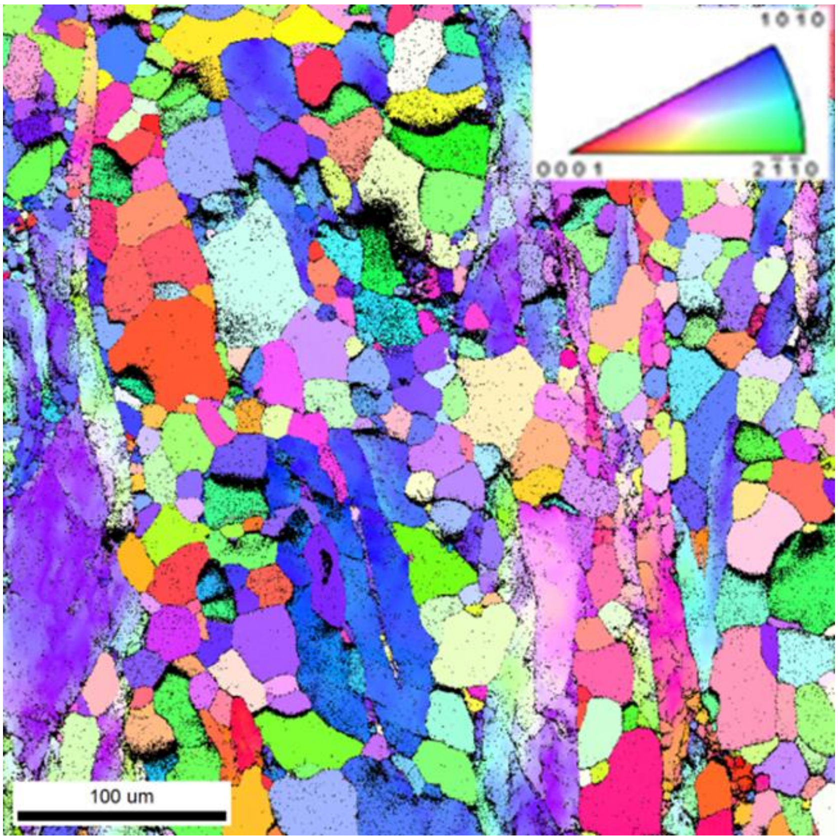

Fig. 5.5 Fully deformed and recrystallised microstructure of Zr-0.3Sn alloy deformed at 875^0C and $10S^{-1}$.

5.5. Development of Constitutive Modelling

As discussed in section 3.1.2 to analyse the deformation of any alloy, modelling and simulation is useful and finite element based deformation modelling is one of the chief techniques employed for this purpose. However, it requires empirical relationship between stress and strain at different temperatures and strain rates in the form of material constants. As it is understood from different studies, mechanism of deformation changes with change in deformation parameters and has significant effect on material constants. Development of single constitutive equation that covers entire range of deformation regimes (in terms of strain rates, strains, and temperatures) is desirable for facilitating the FEM based simulation of the actual industrial deformation process for achieving the optimized processing conditions.

5.5.1. Basis of Constitutive Modelling

High temperature deformation of an alloy takes place by simultaneous application of stress and temperature where strain rate plays important role in comparison to strain hence, strain rate is empirically related to temperature. The effect of temperature and strain rate on the deformation behaviour of the material is usually expressed using a temperature compensated strain rate parameter or Zener–Holloman parameter (Z) [14] in an exponent-type equation:

$$\mathrm{Z} = \dot{\varepsilon}\exp^{\frac{Q}{RT}} \tag{5.4}$$

The hyperbolic law in Arrhenius type equation gives better approximations between Zener–Hollomon parameter and flow stress [15–17]

$$\dot{\varepsilon} = Af(\sigma)exp^{\left(\frac{-Q}{RT}\right)} \tag{5.5}$$

Where f(σ) depends on the level of stress and it is defined as follows:

$$f(\sigma)=\begin{cases} \sigma^{n'} & for\ \alpha\sigma < 0.8 \\ \exp(\beta\sigma) & for\ \alpha\sigma > 1.2 \\ [\sinh(\propto \sigma)]^{n} & for\ all\ \alpha\sigma \end{cases} \tag{5.6}$$

In above equation $\dot{\varepsilon}$= strain rate, A, n',β,α and n are material constants in which n', β and α are related by β=αn' and depend on strain. Material constants are identified α as stress level parameter (mm^2 N^{-1}), n is stress exponent, A is called structure factor (s-1) and Q is thermal activation energy. Thermal activation energy is one of the important parameters of materials and it is also related to mechanical properties in the process of thermal deformation and reflects the degree of difficulty of thermal deformation (kJ/mol). In above equation R is gas constant (kJ/(mol^0K)) and T is the absolute temperature (K).

5.5.2. Determination of Material Constants

Strain rate $\dot{\boldsymbol{\epsilon}}$ is related to various constants as follows:

$$\dot{\epsilon} = B\sigma^{n'} \tag{5.7}$$

$$\dot{\epsilon} = C\, exp(\beta\sigma) \tag{5.8}$$

$$\dot{\epsilon} = \frac{\alpha}{n'} \tag{5.9}$$

Flow stress data obtained from the isothermal hot compression tests at different strain rates ($\dot{\epsilon}$) were used to estimate the above-mentioned materials constants. The procedure to estimate the material constants A, n', α, β and n is by using the variation of flow stress with temperature and strain rate for a true plastic strain of 0.6. A similar procedure has been used for estimating the material constants at other strains as well.

Taking logarithm on both sides of equation 5.7 and 5.8 it is possible to find the relationship between flow stress and strain rate with material constants n, and β.

$$\text{Ln}(\sigma) = \frac{1}{n'}\ln(\dot{\varepsilon}) - \frac{1}{n'}\ln(B) \tag{5.10}$$

$$\sigma = \frac{1}{\beta}\ln(\dot{\varepsilon}) - \frac{1}{\beta}\ln(C) \tag{5.11}$$

Eq. 5.10 and 5.11 represent a straight line and hence the value of n' and β can be obtained from the slope of lnσ– ln$\dot{\epsilon}$ and σ-ln$\dot{\epsilon}$ plots as shown in Fig.5.6 and 5.7 respectively. The lines are apparently parallel and hence the mean values of slopes are taken as n' and β. The values of n' and β estimated at a different strain values were calculated from results obtained for true strain of 0.6 is shown here, average value n' and β obtained are used to calculate α from α= β/n' relationship.

5.5.3. Determination of activation energy (Q) and Value of strain exponent (n)

In development of constitutive equation activation energy plays an important role and values are characteristic of composition and microstructure of the material. For Zirconium and dilute Zr - 0.3 Sn alloy activation energies have been determined for wrought material; however data for cast material is not available. To determine the value of Q sine hyperbolic equation which takes care of low and high stress values were used.

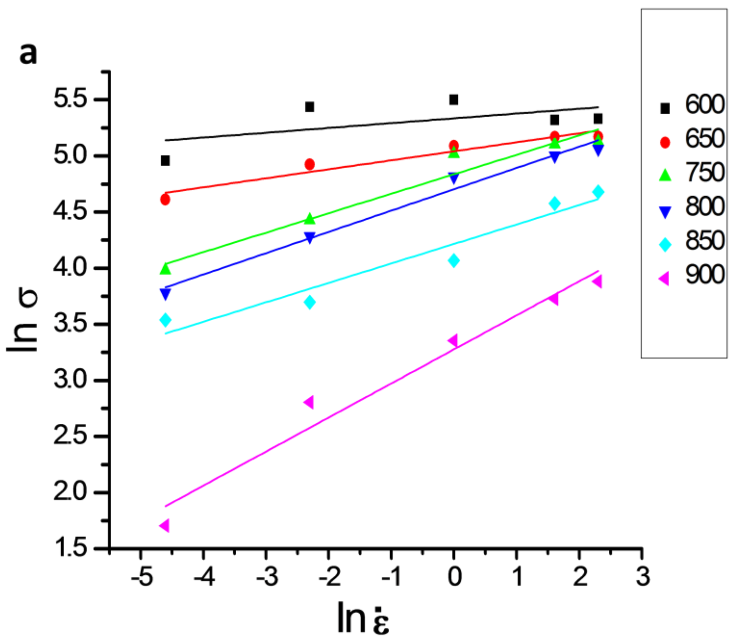

Figure 5.6 Logarithmic Plot of flow stress strain rate Vs ln σ

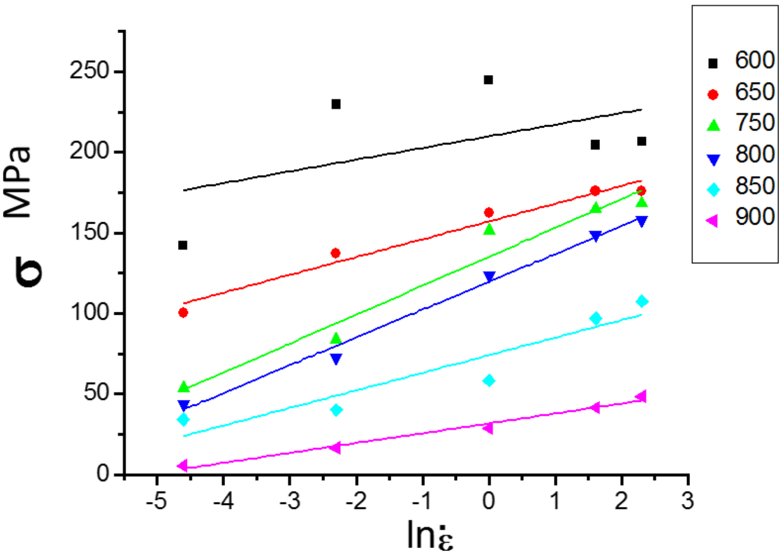

Fig. 5.7 Plot of strain rate $\dot{\epsilon}$ Vs flow stress σ (MPa)

For low and high flow stresses, the constitutive equation is given by:

$$\dot{\varepsilon} = A[\sinh(\alpha\sigma)]^n \exp\left(-\frac{Q}{RT}\right) \quad (5.12)$$

Taking logarithm on both sides of equation 5.12 gives:

$$\ln[\sinh(\alpha\sigma)] = \frac{\ln\dot{\varepsilon}}{n} + \frac{Q}{nRT} - \frac{\ln A}{n} \quad (5.13)$$

The flow stress and strain rate at different temperatures have been used to draw a plot as per equation 5.13 and slope of $\ln\dot{\varepsilon}\ vs\ \ln[\sinh(\alpha\sigma)]$ gives value of 1/n and reciprocal of this n at different temperatures. Average value of n is obtained by averaging all values of n obtained at different temperatures and by this method value of n is equal to 4.53 as is shown in Fig. 5.8 (a). From same equation keeping strain rate constant linear plot is made keeping 1/T along X-axis and $\ln[\sinh(\alpha\sigma)]$ along Y- axis, number of straight lines are obtained for different strain rates and using average value of slopes for different strain rates Q/nR is obtained. In which R as gas constant and n calculated from previous graph value of Q equal to

410KJ/mole obtained after taking average for all strain rates. Using figure 5.8 b value of A was also calculated for different strain rates and average value calculated is equal to 3.36 X 10^{18}.

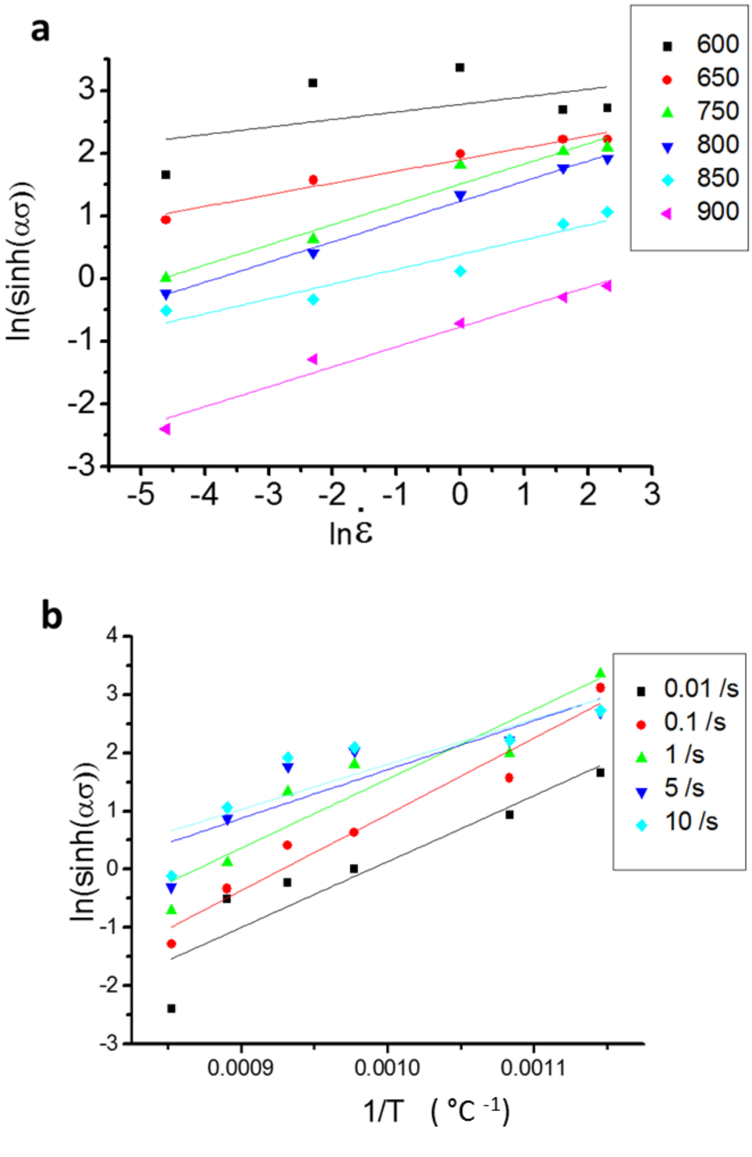

Fig. 5.8 (a) Logarithmic Plot of $\ln[\sinh(\alpha\sigma)]$ $vs \ln\dot{\varepsilon}$ and (b) $\ln[\sinh(\alpha\sigma)]$ vs 1/T

Thus, the constitutive modelling of flow stress related with the strain, deformation temperature and strain rate of Zr - 0.3 Sn alloys can be established during high temperature deformation and the expression is as follows:

$$\sigma_{p=}\ \frac{1}{\alpha}\sinh^{-1}\left(\frac{\dot{\varepsilon}\ exp(Q|RT)}{A}\right)^{1/n} \tag{5.14}$$

5.6. Strain Compensated Arrhenius model

From equation 5.14 it is obvious that the influence of strain is not taken into account in Arrhenius model. However it has been reported that the deformation activation energy and other material constants are significantly affected by strain [18-21]. Flow stress usually varies with strain especially during the occurrence of dynamic recrystallisation which could cause the obvious decreasing of flow stress. Thus Arrhenius model might be inappropriate for describing the dynamic softening phenomenon. In order to provide more precise prediction on flow stress, the strain compensated Arrhenius model is developed considering the effect of strain on all material constants.

To find the effect of strain on material constants α, Q, n and A under different strains similar steps as adopted to calculate for strain 0.6 were applied starting from minimum value of 0.1-0.6 in the interval of 0.1 and values obtained for all constants were plotted against strain. Curve fitting of 4^{th} order polynomial were used to find constants for empirical equation.

$$\alpha = \mathrm{B}_0 + B_1\varepsilon + B_2\varepsilon^2 + B_3\,\varepsilon^3 + B_4\,\varepsilon^4 \tag{5.15}$$

$$n = \mathrm{C}_0 + C_1\varepsilon + C_2\varepsilon^2 + C_3\,\varepsilon^3 + C_4\,\varepsilon^4 \tag{5.16}$$

$$Q = \mathrm{D}_0 + D_1\varepsilon + D_2\varepsilon^2 + D_3\,\varepsilon^3 + D_4\,\varepsilon^4 \tag{5.17}$$

$$lnA = \mathrm{E}_0 + E_1\varepsilon + E_2\varepsilon^2 + E_3\,\varepsilon^3 + E_4\,\varepsilon^4 \tag{5.18}$$

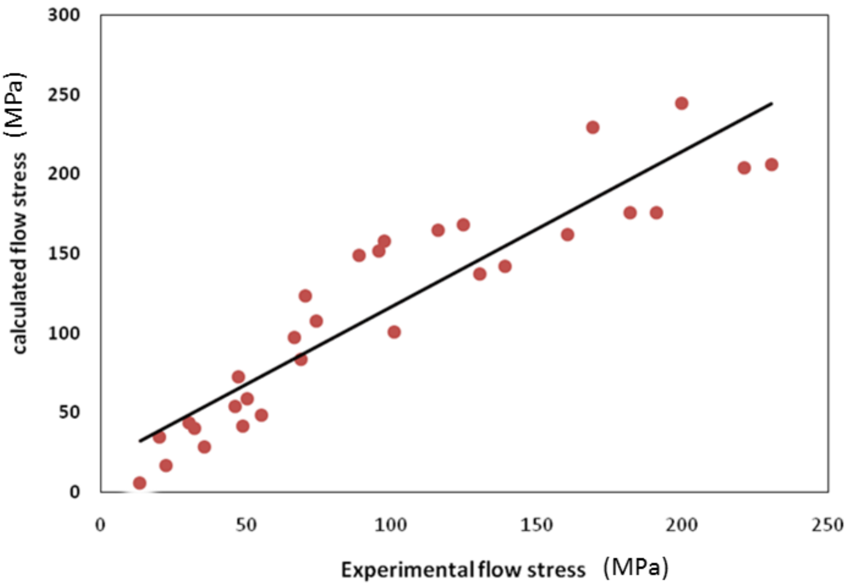

Fig. 5.9 Plot of experimental flow stress Vs calculated flow stress

5.6.1 Effect of strain on Material constants

Figure 5.10 shows change in value of stress level parameters (α) a material constant with variation in strain. Its value remains nearly constant in medium strain region but increases both at lower and higher strain.

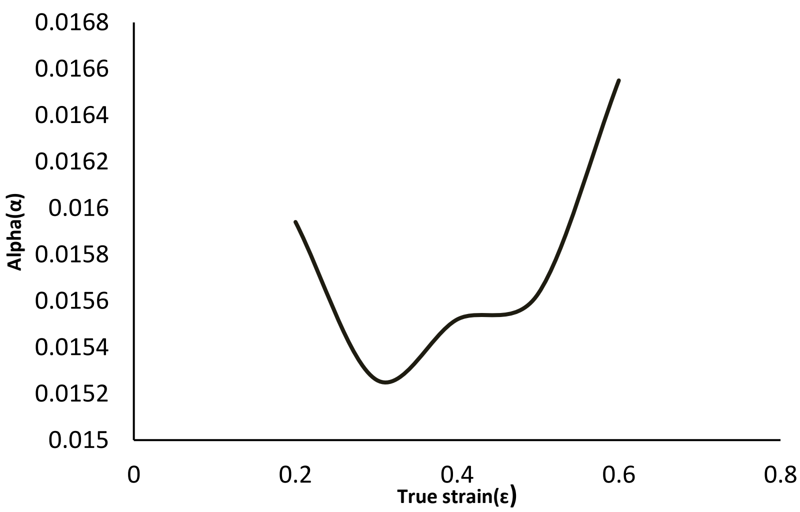

Fig. 5.10 Plot of Alpha Vs True strain shows minimum and maximum value

Another material constant stress exponent (n) decreases gradually as value of strain increases (figure 5.11). This effect is mainly due to reduced effect of strain hardening in material as value of strain increases in high temperature deformation of the material. Activation energy (Q) has significant effect of strain, where its value is high at low strain and decreases drastically with increase in strain and after reaching minimum at 0.4 it starts increasing again with increase in strain (figure5.12). A is a structure constant and its value decreases continuously with increase in strain (figure 5.13).

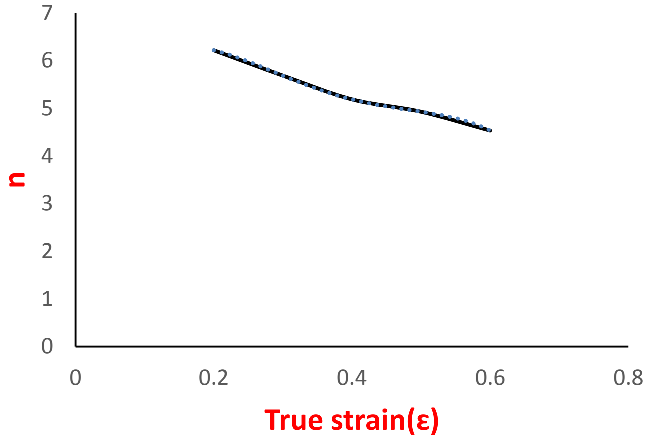

Fig. 5.11 Plot of n vs. true strain

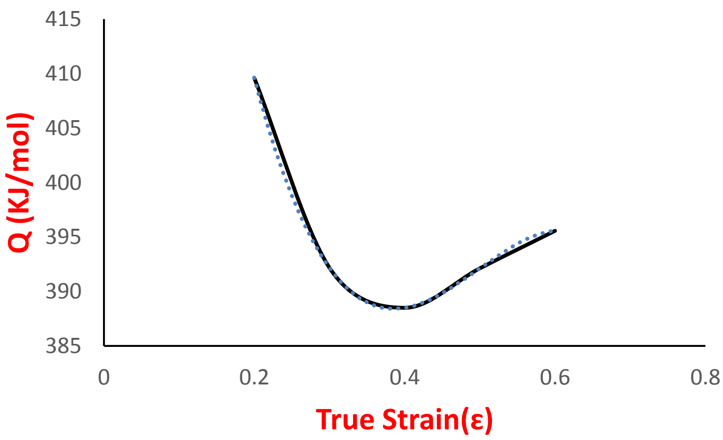

Fig. 5.12 : Plot of activation energy vs. true strain

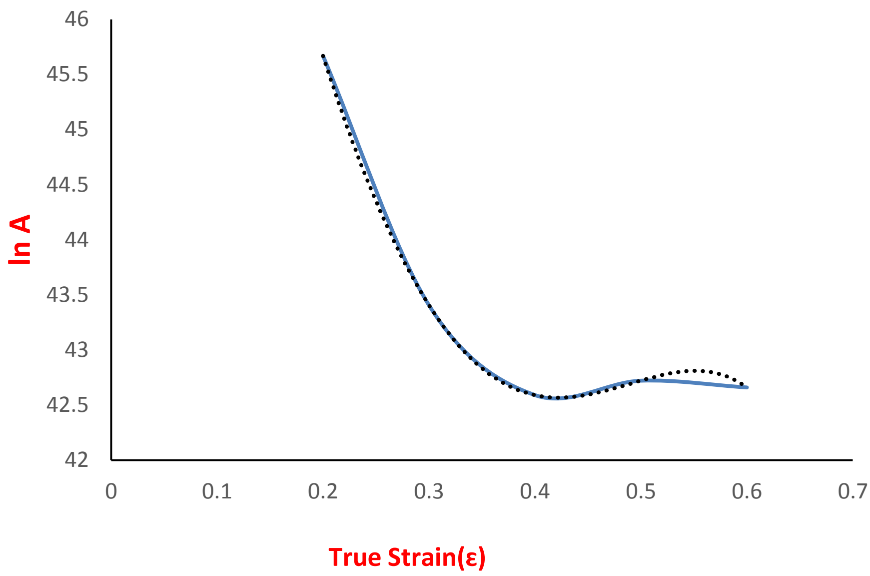

Fig. 5.13 : Plot of lnA vs. true strain

Based on above plots for all constants and curve fittings polynomial equation are developed which given below:

$$\alpha = 0.8542\varepsilon^4 - 1.3775\varepsilon^3 + 0.817\varepsilon^2 - 0.2091\varepsilon + 0.0347$$

$$n = -242.19\varepsilon^4 + 373.51\varepsilon^3 - 201.32\varepsilon^2 + 40.123\varepsilon + 3.6422$$

$$Q = -433.33\varepsilon^4 - 466.67\varepsilon^3 + 1345.3\varepsilon^2 - 730.03\varepsilon + 506.22$$

$$\ln A = -264.92\varepsilon^4 + 287.21\varepsilon^3 - 40.405\varepsilon^2 - 39.774\varepsilon + 53.365$$

Constants obtained from above equations are given in table 5.2. Flow stress for different value of strain and strain rate were calculated and after inserting these value in constitutive equation 4.14 value of flow stress related with the strain, deformation temperature and strain rate of Zr - 0.3 Sn alloys are obtained.

$$\sigma_{p=} \frac{1}{\alpha}\sinh^{-1}\left(\frac{\dot{\varepsilon}\, exp(Q|RT)}{A}\right)^{1/n} \tag{5.19}$$

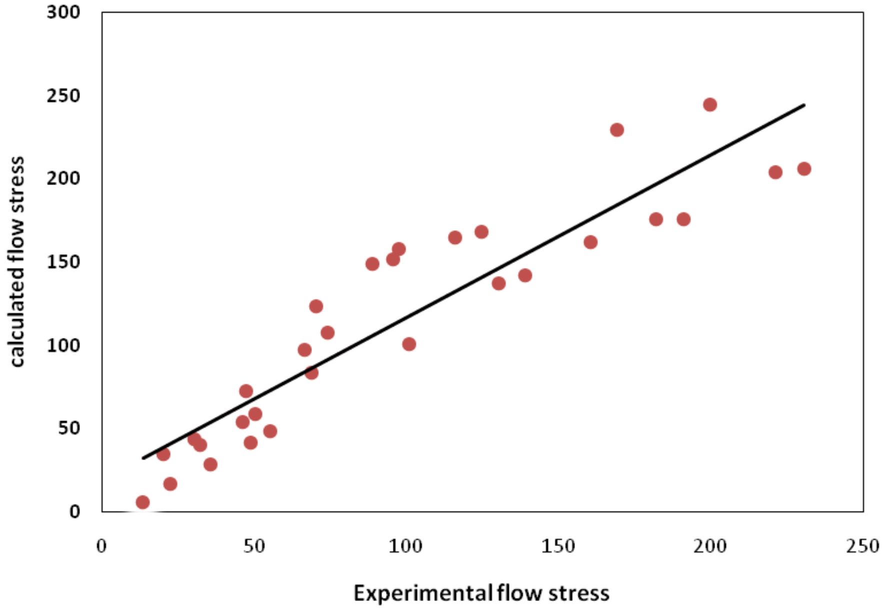

Fig. 5.14 Plot of calculated flow stress vs experimental flow stress

To check the accuracy of constitutive equation value of flow stress obtained using this equation and value obtained from experimental data were compared and maximum error of about 14 percent has been noted.

Table 5.2: Coefficients of polynomial fitting curves for material constants:

α		n		Q		lnA	
B0	.035	C0	3.64	D0	506.22	E0	53.37
B1	-0.21	C1	40.12	D1	-730.03	E1	- 39.77
B2	0.81	C2	- 201.32	D2	1345.3	E2	- 40.41
B3	- 1.38	C3	373.51	D3	-466.67	E3	287.21
B4	0.85	C4	-242.19	D4	-433.33	E4	-264.92

5.7. Validation of Constitutive Equation

The finite element method has been the most commonly used technique to simulate metal forming processes. A commercial finite element program HyperXtrude was used to simulate material flow during extrusion. This program uses arbitrary Lagrangian-Eulerian formulation to compute velocity, temperature, stress, strain, and pressure in the flow field and based on the stresses, forces on the tool are also computed. This technique has been used with variety of approaches including Lagrangian, Eulerian and more recently Arbitrary Lagrangian - Eulerian (ALE). Conservation of mass, momentum, and energy principles produce the fundamental equations that govern flow and heat transfer of incompressible viscous fluids. These equations are written in terms of primitive variables (velocity, pressure, and temperature) with reference to a Eulerian frame, i.e., a space-fixed system of coordinates through which the fluid flows. HyperXtrude software makes use of finite element model based on Zener Holloman relation as given in equation 5.4, 5.5 and 5.6 and using various constant values obtained for Zr Sn alloy simulation has been done and load curves and other values were validated for extrusion of ZrSn alloy.

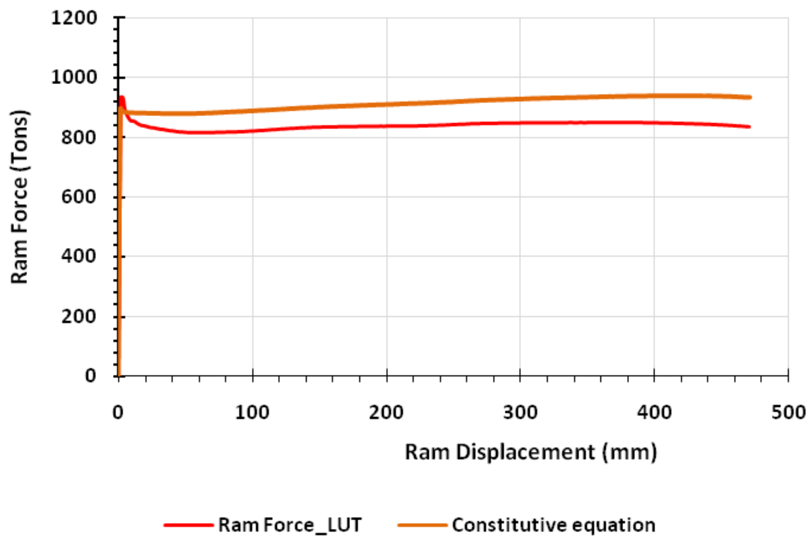

Fig. 5.15 Validation of constitutive Equation using Simulation of ZrSn Extrusion

It can be seen that the ram force computed using the look up table for material properties matched very well with that of the one computed using the constitutive equation developed in the present work for the material.

5.8. Summary

Co-extrusion of ZrSn lined zircaloy-2 tubes at elevated temperature requires optimization of extrusion parameters. Deformation behavior of liner material was studied using hot compression testing method at different temperature and strain rates. Deformation mechanism for cast Zr-Sn alloy with respect to micro-structural stability has been obtained by developing power dissipation maps with the concept of Dynamic Materials Model. Processing map has been developed using thermo-mechanical data generated using thermo-mechanical simulator. The map developed systematically explains the influence of temperature and strain rate on the constitutive flow behavior of cast Zr-Sn alloy. Different regions of processing maps have been validated with microstructure developed during deformation of cast Zr-Sn alloy. This type of maps is useful for bulk deformation process and can be utilized in industrial practice. For FEM based simulation and modelling of hot deformation process constitutive equation has been developed for cast Zr0.3Sn alloy. As deformation of as cast material is inhomogeneous, which was observed from true strain vs flow stress curves, it was difficult to obtain a constitutive equation which is valid in entire range of deformation conditions. Therefore, strain compensated constitutive equation has been developed for cast Zr-0.3Sn alloy. Flow stress obtained from this equation has a net error of 13.9 % compared to experimental data and this error is mainly in lower temperature and higher strain rate regime. Constitutive equation was validated using extrusion simulation software where both data were used for validation, i.e. one from look up table and another directly using constitutive equation and difference in flow stress between both methods is about 14 % similar to the error observed in flow stress. The variation in results is mainly observed due to variation in activation energy of the material at different temperature and strain rate.

5.9. References

[1] Davies, J. H., Armijo, J. S., and Wisner, S. B., "Zirconium-Barrier Cladding Attributes," Zirconium in the Nuclear Industry: Seventh International Symposium, ASTM STP 939, R. B. Adamson and L. F. P. Van Swam, Eds., American Society for Testing and Materials, Philadelphia, 1987, pp. 675-699

[2] O. Sabokpa, A. Zarei-Hanzaki, H.R. Abedi, N. Haghdadi, Artificial neural network modeling to predict the high temperature flow behavior of an AZ81 magnesium alloy, Mater. Des. 39 (2012) 390–396. doi:10.1016/j.matdes.2012.03.002.

[3] H.L. Gegel, J.C. Malas, S.M. Doraievelu and V.A. Shende, Metals Handbook, Vol. 14 (American Society for Metals, Metals Park, Ohio 1987), n.d.

[4] Y.V.R.K. Prasad, H.L. Gegel, S.M. Doraivelu, J.C. Malas, J.T. Morgan, K.A. Lark, D.R. Barker, Modeling of dynamic material behavior in hot deformation: Forging of Ti-6242, Metall. Trans. A. 15 (1984) 1883–1892. doi:10.1007/BF02664902.

[5] Y.V.R.K. Prasad, T. Seshacharyulu, Modelling of hot deformation for microstructural control, Int. Mater. Rev. 43 (1998) 243–258. doi:10.1179/imr.1998.43.6.243.

[6] J.K. Chakravartty, G.K. Dey, S. Banerjee, Y.V.R.K. Prasad, Characterization of hot deformation behaviour of Zr□2.5Nb□0.5Cu using processing maps, J. Nucl. Mater. 218 (1995) 247–255. doi:10.1016/0022-3115(94)00379-3.

[7] J.K. Chakravartty, S. Banerjee, Y.V.R.K. Prasad, M.K. Asundi, Hot-working characteristics of Zircaloy-2 in the temperature range of 650–950°C, J. Nucl. Mater. 187 (1992) 260–271. doi:10.1016/0022-3115(92)90506-G.

[8] R. Kapoor, J.K. Chakravartty, Characterization of hot deformation behaviour of Zr–2.5Nb in β phase, J. Nucl. Mater. 306 (2002) 126–133. doi:10.1016/S0022-3115(02)01290-4.

[9] J.K. Chakravartty, R. Kapoor, S. Banerjee, Y.V.R.K. Prasad, Characterization of hot deformation behavior of Zr–1Nb–1Sn alloy, J. Nucl. Mater. 362 (2007) 75–86. doi:10.1016/j.jnucmat.2006.11.007.

[10] L. Chen, G. Zhao, J. Yu, W. Zhang, T. Wu, Analysis and porthole die design for a multi-hole extrusion process of a hollow, thin-walled aluminum profile, Int. J. Adv. Manuf. Technol. 74 (2014) 383–392. doi:10.1007/s00170-014-6003-4.

[11] C. Zhang, G. Zhao, H. Chen, Y. Guan, F. Kou, Numerical simulation and metal flow analysis of hot extrusion process for a complex hollow aluminum profile, Int. J. Adv. Manuf. Technol. 60 (2012) 101–110. doi:10.1007/s00170-011-3609-7.

[12] A. FarjadBastani, T. Aukrust, S. Brandal, Optimisation of flow balance and isothermal extrusion of aluminium using finite-element simulations, J. Mater. Process. Technol. 211 (2011) 650–667. doi:10.1016/j.jmatprotec.2010.11.021.

[13] F. Parvizian, T. Kayser, C. Hortig, B. Svendsen, Thermomechanical modeling and simulation of aluminum alloy behavior during extrusion and cooling, J. Mater. Process. Technol. 209 (2009) 876–883. doi:10.1016/j.jmatprotec.2008.02.076.

[14] Y.C. Lin, Y.-C. Xia, X.-M. Chen, M.-S. Chen, Constitutive descriptions for hot compressed 2124-T851 aluminum alloy over a wide range of temperature and strain rate, Comput. Mater. Sci. 50 (2010) 227–233. doi:10.1016/j.commatsci.2010.08.003.

[15] W. Li, H. Li, Z. Wang, Z. Zheng, Constitutive equations for high temperature flow stress prediction of Al–14Cu–7Ce alloy, Mater. Sci. Eng. A. 528 (2011) 4098–4103. doi:10.1016/j.msea.2011.01.076.

[16] H.L. Gegel, J.C. Malas, S.M. Doraievelu and V.A. Shende, Metals Handbook, Vol. 14 (American Society for Metals, Metals Park, Ohio 1987), n.d.

[17] Y.V.R.K. Prasad, H.L. Gegel, S.M. Doraivelu, J.C. Malas, J.T. Morgan, K.A. Lark, D.R. Barker, Modeling of dynamic material behavior in hot deformation: Forging of Ti-6242, Metall. Trans. A. 15 (1984) 1883–1892. doi:10.1007/BF02664902.

[18] F. Ren, J. Chen, F. Chen, Constitutive modeling of hot deformation behavior of X20Cr13 martensitic stainless steel with strain effect, Trans. Nonferrous Met. Soc. China. 24 (2014) 1407–1413. doi:10.1016/S1003-6326(14)63206-4.

[19] Y.C. Lin, Y.-C. Xia, X.-M. Chen, M.-S. Chen, Constitutive descriptions for hot compressed 2124-T851 aluminum alloy over a wide range of temperature and strain rate, Comput. Mater. Sci. 50 (2010) 227–233. doi:10.1016/j.commatsci.2010.08.003.

[20] W. Li, H. Li, Z. Wang, Z. Zheng, Constitutive equations for high temperature flow stress prediction of Al–14Cu–7Ce alloy, Mater. Sci. Eng. A. 528 (2011) 4098–4103. doi:10.1016/j.msea.2011.01.076.

[21] H.L. Gegel, J.C. Malas, S.M. Doraievelu and V.A. Shende, Metals Handbook, Vol. 14 (American Society for Metals, Metals Park, Ohio 1987), n.d.

Chapter 6

Modeling of Co-Extrusion of Zircaloy-2 and Zr-Sn Alloy and its Validation

Preamble: Uniaxial hot compression tests results of Zr-Sn alloy were used in this chapter for numerical simulation of co extrusion and tabulated with proper boundary conditions. Results obtained from model in terms of optimum extrusion parameters such as extrusion ratio, temperature and strain rates are validated separately for both alloys and subsequently for their co-extrusion. Microstructural characterizations of co-extruded product in terms of liner thickness variation along the length and experimental co-extrusion load analysis were done to validate the FEM model. The optimised parameters obtained from simulation work can be used to establish the relative flow behavior of two alloys, viz Zr-2 and Zr-Sn during co-extrusion process to develop tubular product with good metallurgical bonding.

6.1. Introduction

It is discussed in earlier chapter that addition of extremely thin layer of highly soft layer of Zr-Sn innerclad layer provides resistance in clad to withstand the effect of stress corrosion cracking, which is one of the primary reasons for failure of a clad at higher burn up. Experimental trials have shown [1] that metallurgical bond, uniform thickness of liner and desired chemical composition of the Zirconium barrier are essential to provide good PCI resistance. The bond is quite unique where recystallization occurs across the Zirconium - Zircaloy interface, which is transgranular with no physical boundary that affect the flow of heat.

Metallurgical bond between the two layers of Zircaloy and ZrSn alloy with uniform lining are the two fundamental and critical requirements for double clad tube proposed for nuclear applications. In practice there are number of methodologies which can be used for this purpose such as diffusion bonding, explosive bonding, friction bonding, ultrasonic welding as compared to mechanical bonding developed by employing cold pressure bonding. Each of process envisaged for development of metallurgical bond has gross limitations to achieve desired results at industrial scale realization of double clad tube. The diffusion bonding takes place with only microscopic deformation between two dissimilar alloys under temperature and pressure. In case of explosive bonding the kinetic energy from detonation allows for metallurgical bond formation while conversion of explosive into kinetic and heat energy. However, the limitation comes because of geometry of the products, uniformity away from the detonation area and inherent hazard of the process. Friction bonding and ultrasonic welding are also potential joining techniques but cannot be employed on industrial scale to produce finished thin wall double clad tubes. Cold pressure bonding by techniques such as co-pilgering, co-drawing or rolling can give good mechanical bond between the layers of two dissimilar metals. However, if the cold mechanical deformation techniques are employed in conjunction with the high temperature deformation such as co-extrusion, there is greater possibility of eliminating bondline defects, non-uniformity of liner thickness and thus achieves desired mechanical properties in the finished thin wall double clad tube.

The Zr-barrier cladding tubes are manufactured by co-extrusion at elevated temperature to form a composite tube shell of Zircaloy with a liner of Zirconium, followed by cold reduction in several passes with intermediate recrystallization anneals. The interface quality should be such that it should be identified primarily by a change in chemical composition from that of dilute Zr Sn alloy to that of Zircaloy, and no distinct physical interface should exist. The interface should not have oxide and grain boundariesso that there is atomic continuity between the zirconium liner and the Zircaloy portion of the cladding.

It has been established that if the difference in flow properties of two inner liner and outer material are wide, fracture, decohesion or delamination and non-uniform flow may take place during thermo mechanical processing of composite billet or tube [2-5]. If the sleeve is hard and the core is soft then the tensile stress on the outer sleeve during co-extrusion can lead to fir-tree type of cracks on outer tube.

In order to achieve the above quality requirements of the double clad, the most critical operation is the co-extrusion of the composite billets. Some of the critical extrusion parameters that determine the quality of the interface are reduction ratio, semi-cone angle of the die, velocity of ram (imposed strain rate), friction between the billet and the container wall and difference in thermo-mechanical properties of liner and outer tubes. Determination of the optimum values for these parameters is rather a challenging and daunting task by the usual trial and error methods. In this context, modelling and simulation methodology can bring out the role of individual parameters and thus help in optimizing these crucial parameter. This is the motivation for this part of the study where in FEM based numerical simulations of hot extrusion have been employed to bring out the role of process parameters on the resulting the co-extrusion process.

Numerical simulation of hot extrusions of Zircaloy 2 and Zr-0.3Sn alloy composites requires the flow behaviour of both alloys at different temperature and strain rates. Thermo mechanical properties of Zircaloy-2 have been studied extensively and flow stress variation with respect to temperature and strain rate has been determined and available in literature [6]. Hot deformation of Zr-Sn alloys has been done in the range 625 to 825^{0}C and constant true strain rates in the range of 10^{-4} to $3x10^{-1}$ sec^{-1}[7-9].

Uniaxial hot compression tests were carried out to determine flow behavior of ZrSn alloy using Gleeble-1500 thermo mechanical simulator. The present chapter utilizes this data for the simulation and the tabulated data of flow stress with respect to temperature and strain rate discussed in experimental section of this thesis for numerical simulation of co-extrusion with proper boundary conditions. Results obtained from model in terms of optimum extrusion parameters such as extrusion ratio, temperature and strain rates are validated separately for both alloys and subsequently for their co-extrusion. Microstructural characterizations of co-extruded product in terms of liner thickness variation along the length and experimental co-extrusion load analysis were done to validate the FEM model. Further metallurgical characterization to establish complete metallurgical bonding was carried out using SEM. In the present work emphasis has been given to establish the relative flow behavior of two alloys viz Zr-2 and Zr-Sn during co-extrusion process to develop tubular product with good metallurgical bonding.

6.2. Numerical Simulation of Co-Extrusion

An FEM model was developed for numerical simulation of Co-extrusion process in Deform-2D Finite element software. The axi-symmetry model showing the objects and their positions in co-extrusion has been shown in fig 6.1. The figure shows bursting of liner prior to billet and the increased liner thickness in the leading end.The 4-noded quadrilateral elements were used for meshing. The Lagrangian incremental approach was used for finite element analysis and Newton Raphson methodology was employed for convergence. Some of the important assumptions made and boundary conditions considered during the co-extrusion simulation include,

- constant heat transfer and friction coefficients between workpiece and tools throughout the extrusion process (Since the deformation involved is relatively high rate, and the heat effects are primarily due to the preheat and plastic work, this assumption does not lead and any significant error in the calculated values)
- work pieces undergoes only plastic deformation. (since the extent of plastic strain is orders of magnitude higher than that of the elastic part, this assumption is justified).
- about 90 % conversion of deformation work into heat, perfect rigidity of the extrusion tools,.

The Input condition for the simulations included material properties of the two alloys, in the form of tabulated data of flow properties. The flow stress data for Zr-2 was taken from literature[6] whereas same was generated for Zr-Sn alloy by hot compression testing on a Gleeble 1500 thermo mechanical simulator. Other inputs such as billet and tooling geometry were given based on possible shop floor trials. The extrusion and co-extrusion parameters such as billet preheat temperature, ram speed, tool temperature for simulations were also designed to optimize the conditions. In the present simulation only initial billet preheat temperature and ram speed have been varied independently keeping the tool temperature constant at 150^{o}C for all the simulation experiments.

Table 6.1 Dimension of Co-extrusion Billet:

Items	Material	O. D. (in mm)	ID (in mm)
Outer layer	Zircaloy-2	142	53.6
Inner Layer	Zr-Sn	53.6	40

(a) (b)

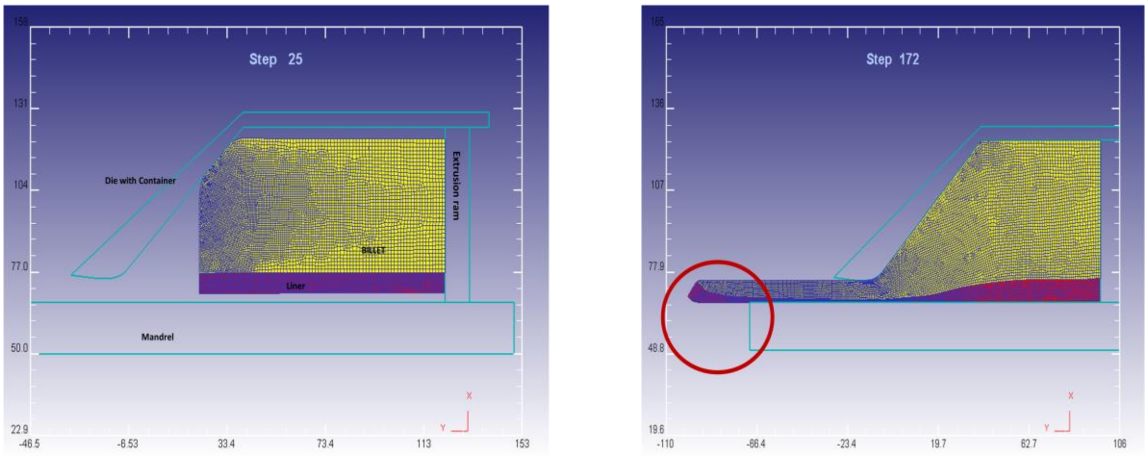

Fig 6.1 a) Co-extrusion Finite element model showing the billet and liner assembled position w.r.t extrusion tools and b)liner bursting in the leading end

6.2.1 Approximation of Heat transfer coefficient

For finding the heat transfer coefficient, simulations were performed by changing the heat transfer coefficient while keeping the friction coefficient as 0.3 at a preheat temperature of 800 ^{o}C and at a ram speed of 40 mm/sec with the material properties of Zr-2. The simulated extrusion load curves were compared with the extrusion load curve obtained in the experiment. The extrusion load was observed to be increasing with heat transfer coefficient. This was because as the heat transfer coefficient was increasing, the heat loss was also increases proportionately, which was decreasing the temperature of the material more and thereby increasing the flow stress and deformation load of the material. The comparison of the load curves at different heat transfer coefficients are shown in figure 6.2.

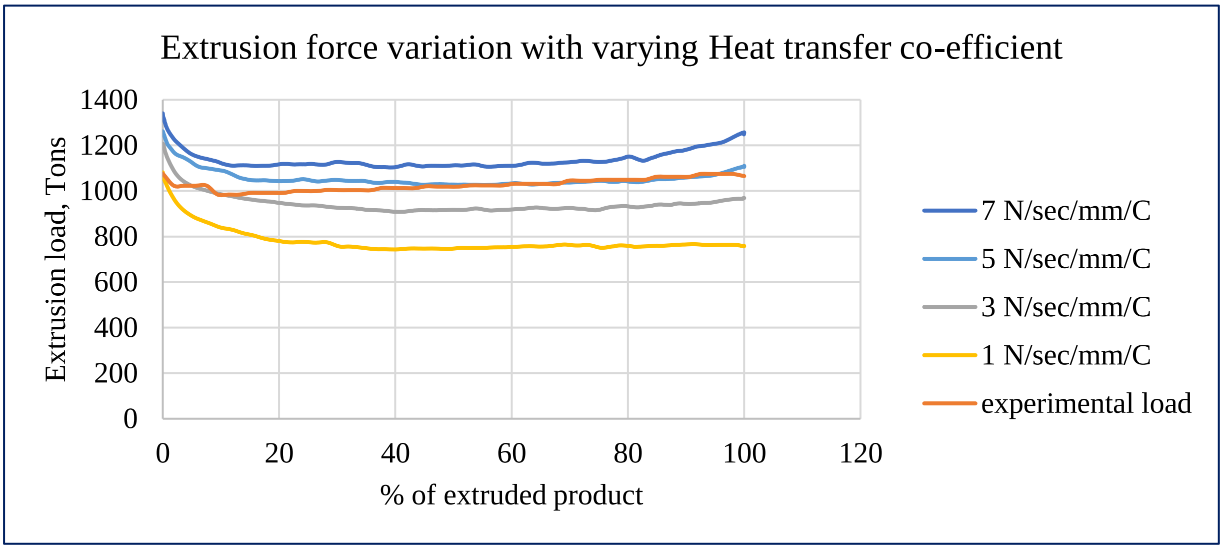

Fig. 6.2 Extrusion load variation with incresing heat transfer coeffcient

Friction Co-efficient : 0.3 (constant)

Heat transfer Co-efficient : 1, 2, 3, 5, 7 N/sec/mm/°C

From the above graph, it was observed that for a heat transfer coefficient of 5 N/sec/mm/ °C, the load curve was matching with that obtained from the experiment. So, the approximated heat transfer coefficient was 5 N/sec/mm/°C.

6.2.2 Approximation of Friction co-efficient

For finding the friction coefficient, keeping the above approximated heat transfer co-efficient as constant, the friction co-efficient was varied from 0.1 to 0.3 and the simulated extrusion load curves was again compared with the experimental load curve. It was observed from the comparison that the extrusion load was increasing with increase in the friction coefficient. This was because of the increase in the frictional load with the increasing friction coefficient. The comparison of extrusion load at different friction coefficient value is shown in figure 6.3.

Heat transfer Co-efficient : 5 N/sec/mm/^{o}C (constant)

Friction Co-efficient : 0.1, 0.2, 0.3

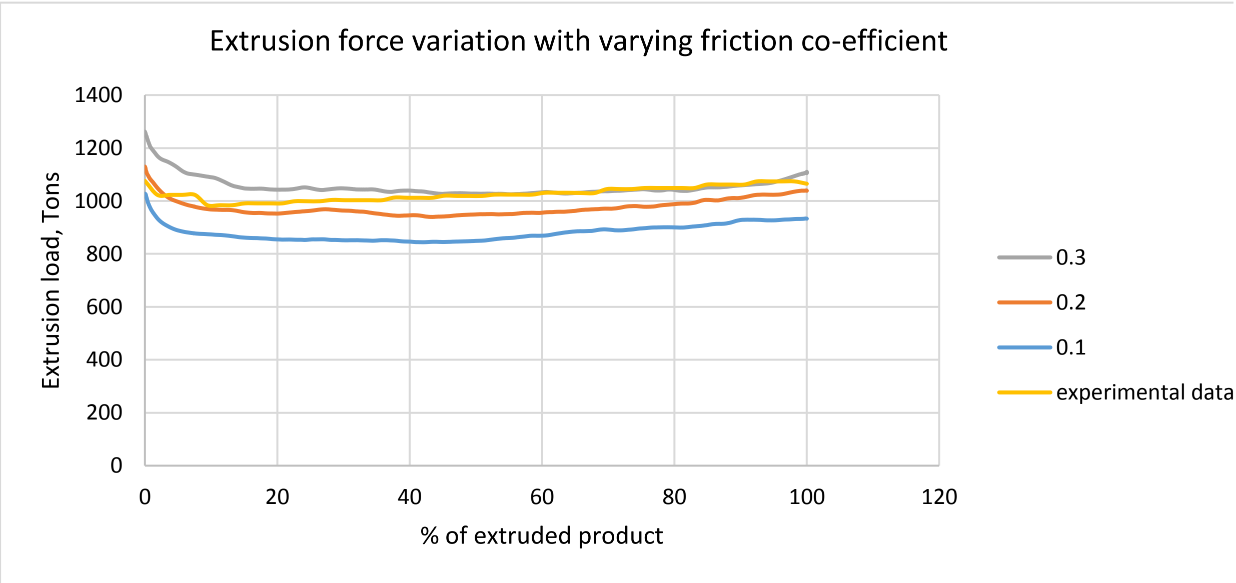

Figure 6.3 Extrusion load variation at different friction coefficient value

From the above extrusion load cures the load curve with the friction coefficient of 0.3 was matching with the experimental load. So, the friction coefficient for the extrusion process was assumed to be 0.3.

With these simulation trails we have approximated both the unknown coefficients. And they were finalized to Friction Coefficient – 0.3 and Heat transfer Coefficient 5 N/sec/mm/ ^{o}C. These coefficients will be used for further extrusion and co-extrusion simulations.

6.2.3. Simulation of Extrusion Load

6.2.3.1. Mesh Optimization

The model was simulated at a temperature of 800^{o}C and at a speed of 35 mm/sec with the same initial and final dimensions as that of the realistic component be produced. The input parameters of billet and product dimensions for co-extrusion were selected similar to what could have been used in the actual experiment. The Mesh sensitivity analysis was done for the FEM model for extrusion of Zr-2 material to reduce its effect on the accuracy of the results as shown in fig 6.4. The mesh element size has been refined by increasing the number of elements in the work piece (billet) of the FEM model. The mesh size was varied from 5000 elements to a maximum of 20000 elements. The variation of the extrusion load in all the simulations were compared with the load curve obtained from experiment. The optimized 9000 number of elements was obtained after which even if we increase the number of elements the variation observed was negligible.

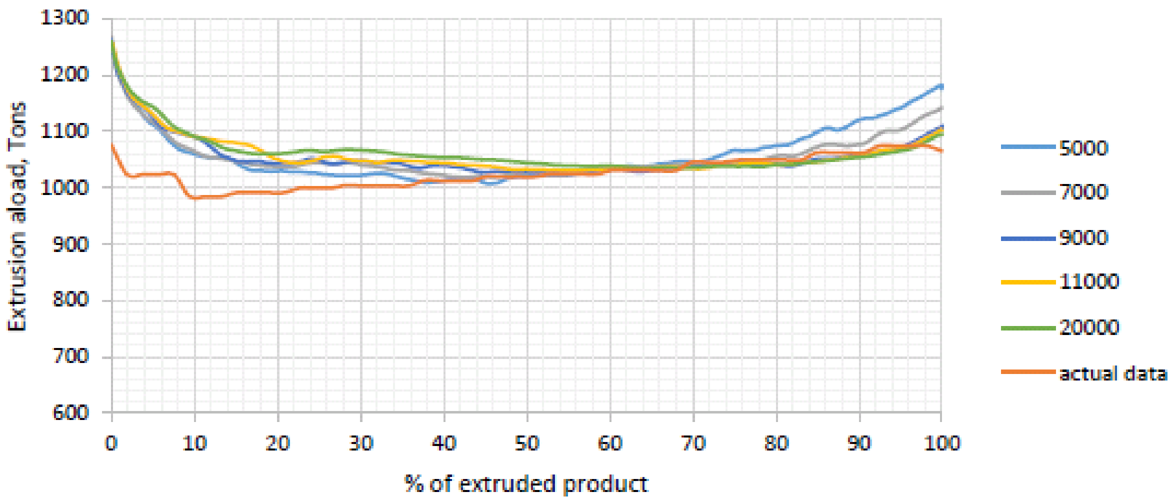

Fig 6.4 . Mesh Sensitivity Analysis indicating optimization of mesh numbers

6.2.3.2. Prediction Of Extrusion Load

Before the actual simulation of co-extrusion of two alloys, extrusion simulation was carried out for individual alloys of Zr-Sn and Zr-2. The simulated curves for two individual alloys have been shown in fig 6.5. The during simulation of extrusion and co-extrusions, flow stress variation with respect to temperature in the range of 650 to 950^0C and strain rate in the range of 10^{-2} to 10 S^{-1} were taken as input. Load curves against percentage of extrudate for simulation of Co-extrusion at the temperature of 800^0 C and 35mm/sec has been compared in fig 6.5. It was observed that the individual load curves are very consistent. At the same time there a significant difference between extrusions loads for the two alloys over the entire length of extrudate. The simulated extrusion load for Zr-2 in the steady state condition was approximately 1000T which is 17.6% higher than the steady state extrusion load for Zr-Sn alloy which is approximately 850T.

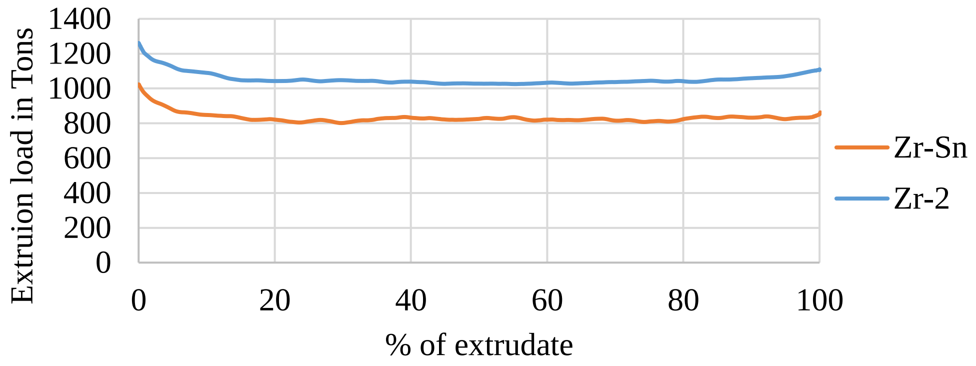

Fig 6.5. Comparison of simulated load for the two alloys

6.2.3.3. Validation Of extrusion Load

This exercise of simulated extrusion load for the ZrSn alloy was validated with the extrusion experiments (fig 6.6). Based on this validation two independent variables i.e heat transfer coefficient and friction co-efficient was established as 0.3 and 5N/Sec/mm/deg C and the same set was taken as input for simulation of co-extrusion of Zr-2/Zr-Sn billet.

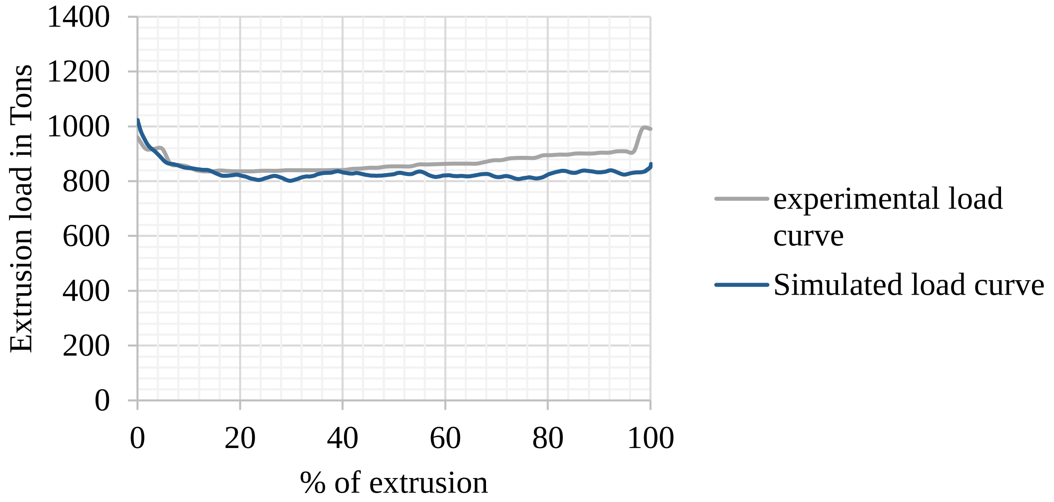

Figure 6.6 Comparison of simulated and experimental load for Zr-Sn alloy and Zr-2

6.3. Simulation of Liner Thickness Co-extrusion

6.3.1. Variation along the length

One of the important features that can indicate the quality of the co-extrusion is the variation in liner thickness. This parameter is readily accessible for determination both in experiments and simulations and hence was used for the optimization exercise.

Variation in liner thickness over the co-extruded length of approximately 1000mm length (from simulated model) was plotted for the co-extruded tube from the leading end as shown in fig 6.7. The co-extrusion was carried out at 800^{o} C and ram speed of 35mm/sec. the plot clearly indicates that there is a burst out of liner in the leading end of the simulated model in the same way as was observed in the experiment (described later). The liner thickness was maximum in the leading end and started reducing before stabilizing with a very limited variation. After initial co-extruded length of 150 to 200 mm from the leading end, the liner thickness got stabilized to a value ranging from 550 mm to 600 µm.

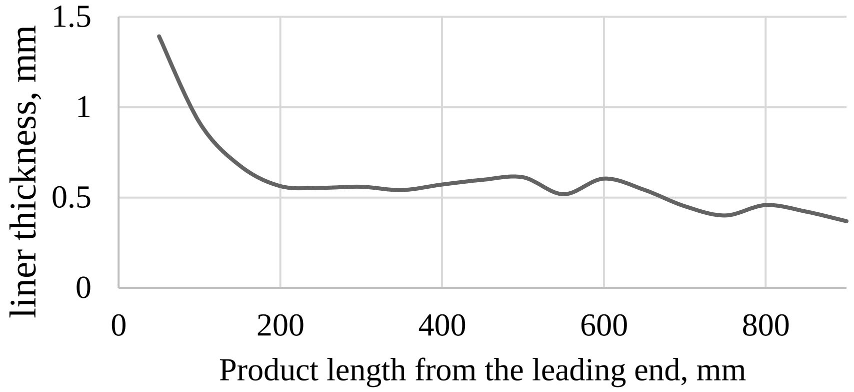

Fig 6.7 Liner thickness variation in simulation along the length of the extruded product

The thickness was in the stabilized range until a reduction was observed at the trailing or back end of the co-extrusion. The liner thickness started decreasing at about 250 mm from the back end. Thus there is a tendency of higher liner thickness variation in the leading and the trailing ends of co-extruded tube. In practice also the upsetting preceeds the actual co extrusion wherein an accumulation of liner material in the front end of composite billet is likely with resistance from co-extrusion die. Also, liner bursting out from the front end is due to the lower flow resistance/stress of the ZrSn alloy as compared to Zr2 which is clearly indicated in fig 6.1 b. Further, reduction in the liner thickness in the back end of the co-extruded is only to maintain the volume constancy. The phenomenon of liner bursting was reduced by employing EB welding at the interface of the composite billet. Novel idea of reduced core length for soft liner material to prevent liner bursting and reduced liner thickness variation has been discussed by Misiolek[11].

6.3.1.1. Effect of Ram Speed

Further, multiple co extrusion simulations were carried out to study the effect of ram speed in co-extrusion, billet preheat temperature and die angles on liner thickness variation keeping input billet size and product size same.

The simulated co-extrusion speed was varied from 5 mm/sec to a maximum of 70 mm/sec at a constant billet pre-heat temperature of 800^{o}C. The maximum liner thickness variation over the steady state condition of co-extrudate was plotted for each extrusion speed and has been shown in fig 6.8. For practical reasons the liner thickness was measured only variation in liner thickness of ZrSn alloy is more sensitive to the changing co-extrusion ram speed than the varying pre heat temperature.

In the stabilized regions linear thickness varies between 0.450 to 0.625 mm for individual co-extrusion ram speed (Table 6.2). It was noticed that the maximum variation in liner thickness is highest for very low co-extrusion speed of 5mm/sec. The variation in thickness decreased with increase in co-extrusion ram speed before reaching to a minimum of only 55µ i.e 9.2% at a speed of 50 mm/sec. On further increase in ram speed thickness variation further tend to increase. This indicated that the optimum speed with reference to the variation in liner thickness was close to 50mm/sec for given temperature of 800^{o} C and co-extrusion ratio.

Table 6.2 Variation of liner thickness with speed of co-extrusion

Sr. No.	Speed mm/sec	Maximum thickness, mm	Minimum Thickness, mm	Difference b/w max and min. thickness, mm	Variation in % of thickness
1	5	0.56	0.31	0.25	42
2	20	0.63	0.49	0.14	23

3	35	0.61	0.52	0.09	15
4	**50**	**0.62**	**0.57**	**0.06**	**9.2**
5	70	0.59	0.46	0.13	22

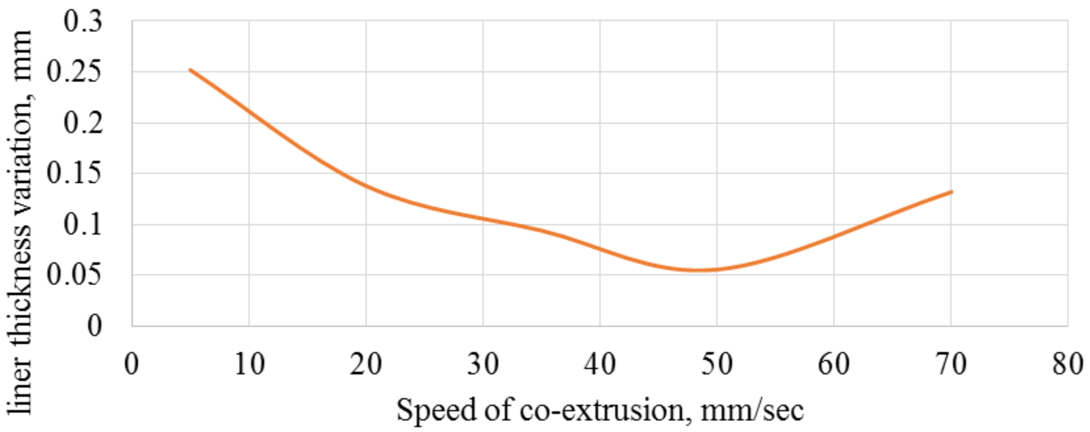

Fig 6.8 Maximum Liner thickness variation with speed of co-extrusion

6.3.1.2. Effect of Temperature on Liner thickness

The liner thickness variation was analyzed for different billet pre-heat temperatures. The billet preheat temperatures were varied from 650°C to 850°C and co-extrusion simulation was carried out at optimized co-extrusion optimum speed of 50 mm/sec. similar to earlier analysis the liner thickness variation along with minimum and maximum thickness was observed in the steady state region in each co-extrusion and has been shown in fig 6.9 and data was tabulated in table 6.3. It was observed that the liner thickness variation in the billet preheat temperature range 750°C to 825°C was not significant and found to be less than 10%. Much higher liner thickness variation of 22% and 38% were observed for the two extremes of preheat temperatures of 650°C and 850°C respectively. Thus for the given ram speed of 50 mm/sec an optimum range of preheating temperature range of 750°C to 825°C can be employed for co-extrusion. Also comparing table 6.1 and 6.2 it can be understood that the variation in liner thickness of ZrSn alloy is more sensitive to the changing co-extrusion ram speed than the varying pre heat temperature.

Table 6.3 Liner thickness variation with billet pre-heat temperature

Sr. No.	Temperature °C	Maximum thickness, mm	Minimum Thickness, mm	Difference b/w max and min. thickness, mm	Variation in % of thickness
1	650	062	0.49	0.13	22
2	750	0.63	0.61	0.03	5
3	775	0.62	0.58	0.04	7
4	800	0.62	0.57	0.06	10
5	825	0.61	0.58	0.03	5
6	850	0.62	0.38	0.23	38

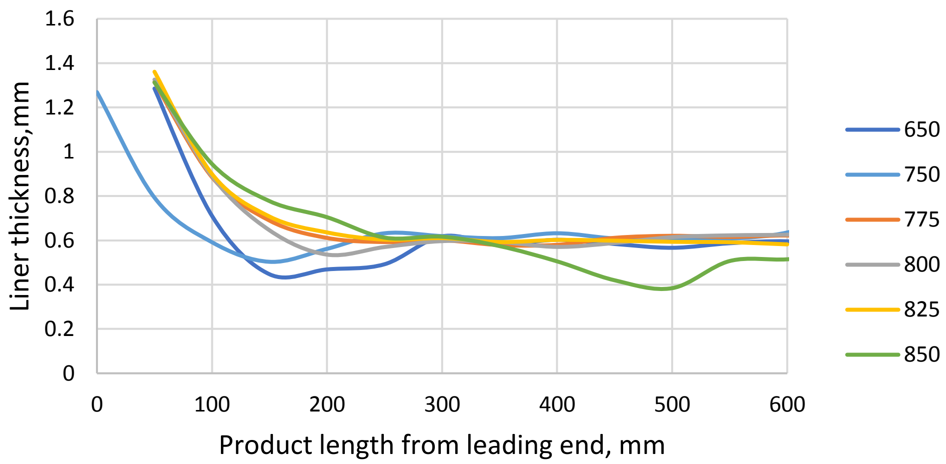

Fig. 6.9 Liner thickness variation with billet pre-heat temperature (°C)

6.3.1.3. Effect of Die Angle

The liner thickness variation was also analyzed in simulations with different die angles. The complex die geometry was exactly replicated to reduce any errors causing due to the variation in the die geometry. Three die angles were chosen for finding their effect on the liner thickness variation. Simulations were carried out with semi die angles of 30^o, 45^o and 60^o at optimized ram speed of 50 mm/sec and at a preheat temperature of 800^{o}C in the optimized range between 750 to 825^o C. Fig 6.10 indicates the maximum liner variation observed at each die angle.

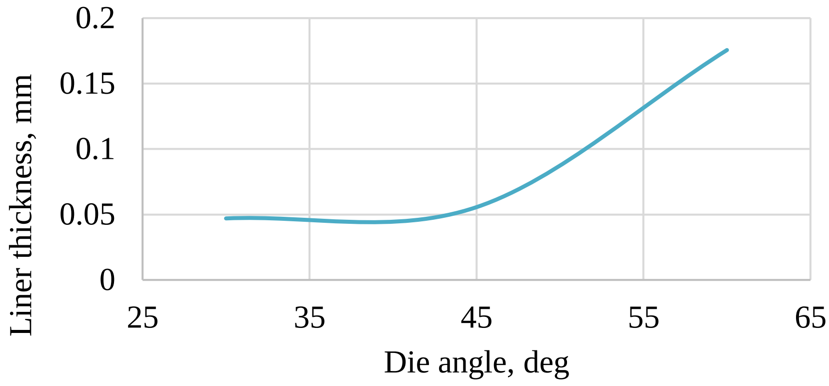

Fig. 6.10 Liner thickness variation with varying semi dies angle

Table 6.4 Liner thickness variation at different semi die angles

Sr. No.	Die angle	Maximum thickness, mm	Minimum Thickness, mm	Difference b/w max and min. thickness, mm	Variation in % of thickness
1	30^0	0.54	0.49	0.05	7.8
2	45^0	0.62	0.57	0.06	9.3
3	60^0	0.73	0.55	0.17	29.2

Also the liner variation along with minimum and maximum thickness observed in the steady state region in each co-extrusion has been shown in the table 6.4. It was observed that the liner thickness along the length was more uniform in the simulations performed with lower die angles. The least variation was observed at a die angle of 30^0. Variation increases with increasing the semi die angle. But the difference in liner variation at die angle 45^0 and 30^0 was very low when compared to liner variation observed between 45^0 and 60^0. Fig 6.11indicates that Co-extrusion load increased with decreasing semi die angle below 45^o toward 30^o but does not reduce significantly if increased to 60^o.

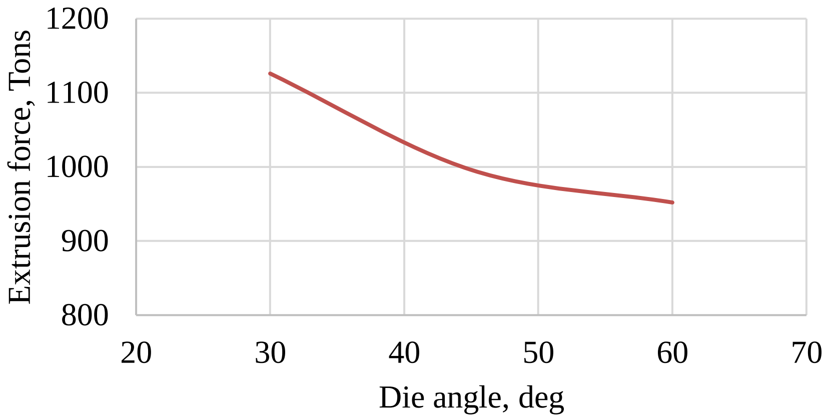

Fig 6.11 Simulated extrusion force variation at different semi die angles

Increase in load is at 30^o as compared to higher semi die angle is due to more surface area in contact with billet thereby increasing frictional resistance. Any simulation trial beyond semi die angle of 60^o was not considered due to non feasibility of co-extrusion experiments. In practice failure of Cu-jackets are most likely due to formation of dead-metal zone during co-extrusion of composite billet. Thus, results of both, the low co-extrusion load and lesser liner thickness variation favor semi die angle close to 45^o.

6.4. Validation of Co-extrusion model

After the thorough analysis of the various parameters in Co–extrusion model, shop floor experiment for co-extrusion was carried out on 3780 T horizontal extrusion press.

Zr2 with Zr-Sn tube as inner layer in composite billet (prepared as described in section 3.1) was produced by hot extrusion experiment on a 3780T horizontal extrusion press (HEP) facility.Composite billet was pre heated in a resistance heating furnace to 800^{o}C and then extruded in the range of ram speed of 35 to 50 mm/sec and semi die angle of 45^{o}.In practice it was not feasible to carry out co-extrusion at constant ram speed. The online co-extrusion load was recorded with respect to time. The raw data of co extrusion load was further plotted with respect to percentage of extrudate for analysis. The co-extrusion load from simulation and experimentation has been compared in fig 6.12 and table 6.5.

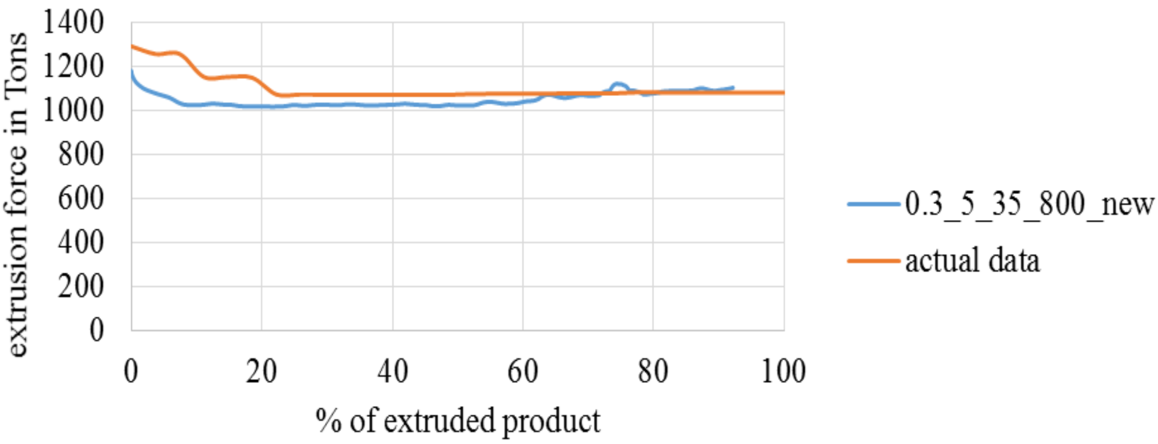

Fig 6.12 Comparison of the simulated and experimental load curve for Co- extrusion of Zr-2/Zr-Sn alloys

Fig 6.12 indicates that the peak co-extrusion load in case of experiment is approximately 1300T and then begins to decrease. The peak load in simulated condition is below the actual condition and is close to 1180 T. However, further the decreasing trend in load is similar before the steady state co-extrusion load condition is achieved between 1070 to 1085T which was very close to the load range 1020 to 1100T predicted by co-extrusion simulation. Both the load curves were observed to be converging beyond 20% co-extrusion. The maximum variation observed in the steady state part of the co-extrusion was found to be only 4 %.

The actual liner thickness and co-extrusion load obtained in the experimental co extrusion were compared with the results obtained for simulated co-extrusion at the optimized parameters. Liner thickness was obtained after metallographic examinations of multiple samples under SEM. Table 6.5 indicates that the ZrSn liner thickness in the range of 570 to 660µ was obtained which is very close to the predicated range of 550 to 620µ for co-extrusion in the optimized range of parameters.

Table 6.5 Comparison of simulated and experimental results of Zr-2 and Zr-Sn

Parameters	Experimental result	Simulated result
Extrusion Load	1070 – 1085 tons	1020 to 1100 tons
Liner thickness	572 to 660 µm	550 to 620 µm

The Zr2 with ZrSn liner co-extruded 50mm OD X 8mm WT tube was successively cold pilgered to finished size of 11.2 mm OD C 0.6mm WT (table 6.6). The 600µ thick ZrSn liner was reduced from extruded stage to the average of 34µ thick in the finished double clad in multiple thermo mechanical steps.

Table 6.6 Liner thickness of Zr-Sn inside Zr-2 shell

Dimension of Tube	Zr-Sn liner thickness (µm)
50 mm OD X 8 mm WT	572 – 660
11.2 mm OD X 0.6 mm WT	29-38

6.5. SEM and Texture Analysis of Zr-2/Zr-Sn Co-extrudate

Polished Samples of the co-extruded tubes were metallographically examined after annealing using low and high magnification SEM. Examinations included the qualitative checking the integrity of the metallurgical bond and quantitative analysis of liner thickness and grain size. Fig 6.13 and 6.14 show the micrographs obtained under SEM followed by quantitative results in table 6.6.When the composite billet prepared with hot shrink fitting and non-EB welding was used for co-extrusion, a significant bondline defects as shown in fig 6.13 were observed in the transverse cross section. Further images in fig 6.14 shows the continuity of interface formed between the Zr2 and Zr-Sn alloy in the co-extruded section after the employing modified composite billet preparation technique. The microstructure clearly indicates the fully recrytallised conditioned in both the alloys across the boundaries. The grain size variation has been tabulated in table 6.7 which indicated that the grain obtained for Zr-Sn in co-extruded blanks is slightly higher compared to that in Zr2, which may be due to an additional hot working step for starting ZrSn material before the assembly of composite billet. With the continuous cold working and annealing passes the difference in grain sizes for Zr2 and ZrSn have been narrowed down. Table 6.8 indicates the variation in the quantitative texture variation in individual layers in term of Kearns f-parameters in three principal direction of the tube.

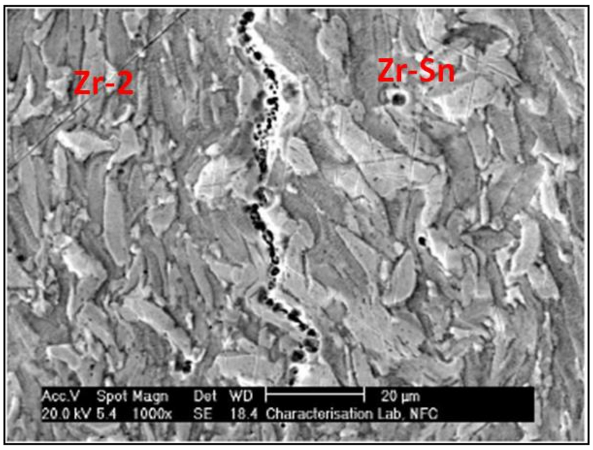

Fig. 6.13 SEM micrographs of co-extruded tube showing defective interface.

It was observed that at the co-extruded tube stage the (0002) basal pole texture in the ZrSn and Zr2 layers were both preferentially transverse. With the successive cold reduction a significant reorientation in basal pole was observed and eventually the final texture was found to be predominantly radial. There was no change in basal pole orientation in longitudinal or rolling direction throughout the thermo mechanical processing.

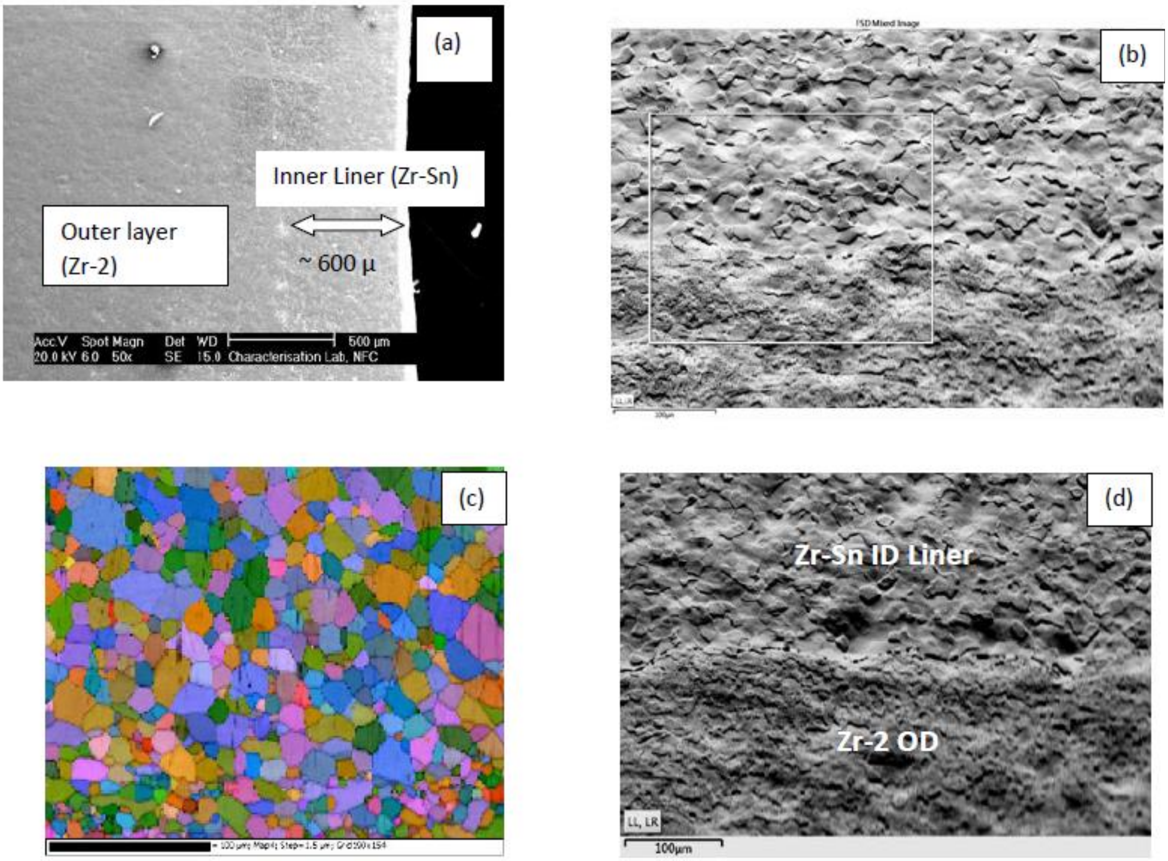

Fig. 6.14 Microstructure of Co-extruded clad tube shown a)Low Mag SEM image (b) image of the region covering Zr-Sn layer and Zr-2 c) Orientation Map of interface region d) High Mag SEM image of interface region showing well bonded layer Zr-2 respectively

Table 6.7. Grain size (µm) of Zr-Sn lined Zr-2 double clad at co-extrusion and final stage

Stages		**Average**	**Std. deviation**	**Min.**	**Max.**
50 mm OD X 8 mm WT	Zr2	8.3	2.7	5.4	20.7
	Zr-Sn	12.3	4.4	5.4	29.3
11.2 mm OD X 0.6 mm WT	Zr2	3.4	1.6	1.3	8.3
	Zr-Sn	4.0	1.7	1.8	8.3

Table 6.8. Kern’s (f) factor for Zr-Sn liner and Zr-2 at co-extrusion and finished stage

Stages		**Kern’s (f) factors**		
		f_r	f_t	f_a
50 mm OD X 8 mm WT	Zr2	0.40	0.52	0.06
	Zr-Sn	0.34	0.61	0.04
11.2 mm OD X 0.6 mm WT	Zr2	0.70	0.24	0.05
	Zr-Sn	0.64	0.27	0.08

6.6. Summary

1. An FEM based Co-extrusion model was developed and numerical simulation of a very complex process of Co-extrusion was successfully carried out for Zr2 and ZrSn composite.

2. Optimization of Co-extrusion parameters in terms of ram speed, preheat temperature and semi die angles through numerical simulation was carried out over the fairly wide range. The co-extrusion ram speed was varied between 5 to 70 mm/sec whereas preheat temperature was varied between 650 to 850^o C and semi die angle varied between 30^o to 60^o. The entire exercise of optimization of parameters through simulation was carried out with the aim to minimize the variation in liner thickness of the co-extrudate.

3. It was observed that the variation in ZrSn liner thickness were most sensitive to the ram speed of co-extrusion. The ram speeds close to 50 mm/sec at the billet preheat temperature of 800^{o}C.

4. Billet preheat temperature in the range of 750 to 825^o C was found to be an optimum range with ram speed closer to 50 mm /sec.

5. Semi die angle of 45^o was observed to be most suited for minimizing the Zr-Sn liner thickness vation under the optimum conditions of Ram speed and pre heat temperature.

6. Results of the numerical simulation was successfully validated by full scale co-extrusion trial under a set of optimum condition. Ram speed in the range of 35- 50 mm/sec at 800^{o}C with semi die angle of 45^{o} was employed and the actual steady state co-extrusion load of 1070 to 1085 T was observed to be close to predicted range of 1020-1100T. Also The actual average ZrSn liner thickness of 600 μm obtained was close to predicted range of 550 to 620 μ.

7. Under the optimized set of co-extrusion parameters and systematic composite billet preparation technique co-extruded blanks of Zr2 with ZrSn liner was successfully developed with complete metallurgical bonding at the interface and without presence of bond line defects.

6.7. Reference

1. Rosenbaum, H. S., Rand, R. A., Tucker, R. P., Cheng, B., Adamson, R.B., Davies, J. H., Armijo, J. S., and Wisner, S. B., "Zirconium-Barrier Cladding Attributes," Zirconium in the Nuclear Industry: Seventh International Symposium, ASTM STP 939, R. B. Adamson and L. F. P. Van Swam, Eds., American Society for Testing and Materials, Philadelphia, 1987, pp. 675-699
2. B. Avitzur, Handbook of Metal-Forming Processes, Wiley, New York, 1983
3. Wojciech Z. Misiolek Et Al, Final Technical Report On "Physical And Numerical Analysis Of Extrusion Process For Production Of Bimetallic Tubes", 2008, ORNL/TM-2006/72
4. H. Dyja Et Al In "Theoretical Analysis And Optimisation Of Parameters In Extrusion Process Of Explosive Cladded Bimetallic Rods", Journal Of Materials Processing Technology 157–158 (2004) 208–212
5. A. Khosravifard Et Al In "Investigation Of Parameters Affecting Interface Strength In Al/Cu clad Bimetal Rod Extrusion Process", Materials And Design 31 (2010) 493–499
6. J.K. Chakravartty ", S. Banerjee ", Y.V.R.K. Prasad ' and M.K. Asundi "Hot-working characteristics of Zircaloy-2 in the temperature range of 650-950°C, Journal of Nuclear Materials 9 January 1992
7. Michael J. Luton "High Temperature Deformation Of Zirconium And Zirconium Tin Alloys" Doctor of Philosophy Metal1urgical Engineering
8. D. J. Abson and J. J. Jonas "Substructure Strengthening In Zirconium And Zirconium-Tin Alloys" Journal Of Nuclear Materials, 24 September 1971
9. Michael J. Luton "High Temperature deformation of Zirconium and Zirconium Tin Alloy" Doctor Of Philosophy Metallurgical Engineering, McGill University Montreal.

10. Wojciech Z. Misiolek Et Al, Final Technical Report On “Physical And Numerical Analysis Of Extrusion Process For Production Of Bimetallic Tubes”, 2008, ORNL/TM-2006/72

Chapter 7

Thermo-Mechanical Simulation of Hot Extrusion Process for Zr-2.5Nb-0.5Cu Alloy

Preamble: Hot extrusion is one of the important steps in thermo mechanical processing of two phase Zr-2.5Nb-0.5Cu alloy. Hot compression testing was done to obtain the results of variation in flow stress with temperature and strain rate. Computation was made for velocity, temperature, stress, strain and pressure in the flow field and based on the stresses, forces on the tool were also determined.

7.1. Introduction

Zr-2.5Nb-0.5Cu alloy is an important structural component of pressurized heavy water reactors (PHWRs) and used to manufacture garter spring. It separates pressure tube from calandria tube. It is a helical extension or compression springs whose ends are connected in order to form each spring into a circle which exerts radial forces around pressure tube. Garter spring needs adequate strength to support pressure tube and it should prevent contact between pressure tube andcalandria tube in the event of diametral creep of pressure tube. Copper is added to Zr-2.5%Nb alloy used as pressure tube material in PHWRs to improve its strength by precipitation. The corrosion properties are also improved due to addition of copper. Although physical metallurgy and characterization of Zr-2.5 %Nb has been studied significantly [6-9], however the study on Zr-2.5Nb-0.5%Cu is rather limited. Both metastable and equilibrium phase transformation behavior of Zr-2.5%Nb is known to be affected by presence of alpha and beta phase stabilizing elements. The properties of Zr-2.5Nb-0.5Cu alloy are very sensitive to the thermo mechanical fabrication steps starting with hot extrusion followed by multiple working with intermediate annealing. In extrusion, correct design and control requires, among other things, the determination of the deformation mechanics involved in the process. Without the knowledge of the influence of variables such as friction process conditions, material properties and workpiece geometry on theprocess mechanics, it would not be possible to design the dies and the equipment adequately, or to predict and prevent the occurrence of defects.

. Thus, the use of FEM in the extrusion process provides an excellent means of obtaining information on how the material flows, how the desired geometry can be achieved, and what the expected mechanical properties in the extrudate [111-115]. Such objectives essentially consist of, a) establishing the kinematic relationships (velocities, strain-rates) between the deformed and unreformed part, i. e. predicting metal flow, b) establishing the limits of formability, i. e. establishing, whether it is possible to form the extrudate without surface and\or internal defects and c) predicting the forces and stresses necessary to execute the process so that tooling and equipment can be designed or selected accordingly.

7.2. Hot extrusion model

The three main types of FE methods that are utilized in extrusion simulation are Lagrangian, Eulerian and Arbitrary Lagrangian Eulerian (ALE). The ALE method is essentially an arbitrary combination of the Lagrangian and Eulerian methods and attempts to bring the advantages with both Lagrangian and Eulerian formulations together. In an ALE formulation the displacements of material and mesh are decoupled and the mesh can move independently of the material. The ALE formulation is ideally suited for modeling of fluid-structure interaction and motion of free surfaces in fluid mechanics. Since the heavy plastic deformation involved in extrusion resembles fluid flow, ALE method is well suited for extrusion simulations. The present work uses HyperXtrude®, a commercial simulation software module dedicated to simulation of extrusion process using the ALE approach. The models were prepared using a structured mesh with appropriate biasing to maintain accuracy and continuity across the faces of different elements. Figure 7.1 shows the geometry of the model along with the various boundaries and the way interactions with surrounding are modeled. As can be seen, the model is made up of different zones representing the container portion, die cavity, die land and exit region. The interaction of the billet material with the surroundings is modeled through appropriate heat transfer and friction boundaries as show in the figure 7.1. Error in heat balance and mass balance at successive simulation time steps were kept below 5% and 1% respectively in order to achieve good convergence in a reasonable time frame.

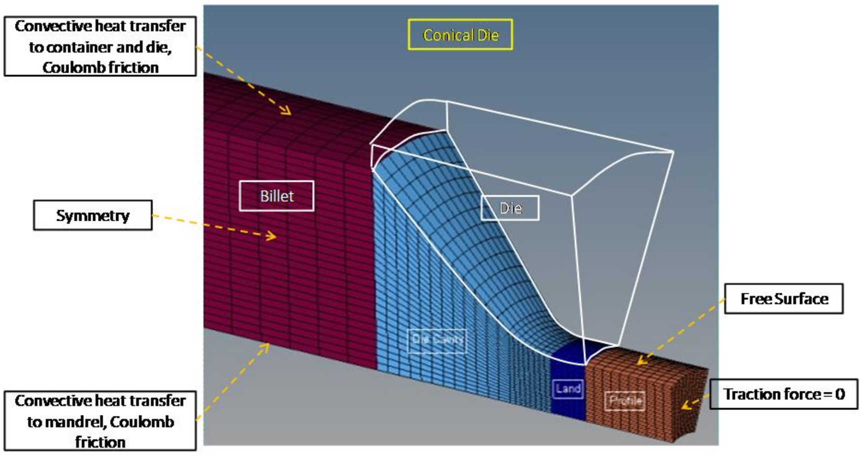

Fig7.1 Schematic explaining the meshing scheme, various components of the model geometry and various interactions of the model with the bounding surfaces.

7.2.1. Mathematical formulation

The fundamental equations that govern flow and heat transfer of incompressible viscous fluids are derived from principles of conservation of mass, momentum, and energy. These equations are written in terms of primitive variables (velocity, pressure, and temperature) with reference to an Eulerian frame, i.e., a space-fixed system of coordinates through which the fluid flows.

$$\nabla \cdot U = 0 \qquad 7.1\ (a)$$

$$\rho (U \cdot \nabla) U = \nabla \cdot (\sigma) \qquad 7.1\ (b)$$

$$\rho C_P\ U \cdot \nabla T = \nabla \cdot q + \varphi \qquad 7.1\ (c)$$

Where, U is the velocity vector, σ is the total stress tensor, T is the temperature, ρ is the mass density, C_P is the specific heat of the fluid at constant pressure, q is the heat flux vector, and φ represents internal heat generation rate due to viscous dissipation.

7.2.2. Constitutive model

For viscous incompressible fluids, the components of total stress tensor (σ), can be represented as the sum of viscous stress tensor (the deviatoric part of the stress tensor) (τ), and a spherical hydrostatic pressure (P).

$$\sigma = \tau - P \qquad 7.2$$

The material behavior is specified by the constitutive relations for the viscous stress tensor, (τ) and the heat flux vector (q) by the following equations [28].

$$\tau = 2\mu\gamma \qquad 7.3\ (a)$$

$$\gamma = [(\nabla U) + (\nabla V)]^T \qquad 7.3(b)$$

$$q = -k\nabla T \qquad 7.3(c)$$

In the above equations, μ is the viscosity, and k is the isotropic thermal conductivity of the material. This viscosity is a function of strain rate and temperature of the material and described using sine-hyperbolic inverse relation:

$$\mu = \frac{\sigma}{\sqrt{3}\dot{\varepsilon}} \qquad 7.4\ (a)$$

$$\varepsilon = \frac{2}{3}[\gamma : \gamma]^{\left(\frac{2}{3}\right)} \qquad 7.4\ (b)$$

Where, σ is the flow stress, and $\dot{\varepsilon}$ is the effective strain rate, α is stress multiplier, n is stress component, Z is Zener-Hollomon parameter, Q is Activation Energy, R is Universal Gas Constant and θ is the temperature. The flow stress for any metal depends on an internal state variable representing the material microstructure. An accurate description of the flow stress requires solving an evolution equation, which governs the internal state variable. In case the flow stress values cannot be fit into a single constitutive equation, as is the case for Zr-2.5Nb-0.5Cu alloys, tabulated experimental data for flow stresses at different temperatures, strains and strain rates has to be utilized as explained in section 7.2.3.

Following are the boundary conditions assigned to various regions of the simulation model (see figure 7. 1):

- Convective Heat Transfer boundary: All tool face boundaries are assigned convective heat transfer boundary, i.e., heat removal from these faces is through convection.
- Friction Boundary: When shear stress over contact surfaces exceeds critical shear stress, material starts to flow.
- Inflow Boundary: A constant velocity and temperature boundary condition is assigned at billet ram face.
- Free Surface Boundary: Free surface boundary is assigned at profile surface. This boundary is assigned an insulated boundary i.e. q (heat flux) = 0.
- Outflow Boundary: This boundary is assigned to profile face.

  Traction forces = 0 (as the extrudate is not pulled out of the die), Displacement = 0 (as extrudate is free to expand),

  Heat Flux = 0
- Symmetric Boundary: This is assigned to symmetric faces.

Mathematically, these are expressed as:

Billet-Ram Interface :

$$U = U_{Ram} ; T = T_{Ram} \qquad 7.5$$

Billet-Container Interface :

$$\tau_S = \mu\sigma_N ; T = T_{Container} \qquad 7.6$$

Die Face :

$$\tau_S = C(U-U_{Tool})\ ;\ T = T_{Container}\ ; \tag{7.7}$$

Bearing Surface :

$$\tau_S = C(U-U_{Tool}) \tag{7.8}$$

Free Surface :

$$\sigma \cdot n = 0 \tag{7.9}$$

7.2.3. Material properties used for simulations:

The accuracy of the results of numerical simulations is determined by the extent to which the subject material and the environment are accurately represented in the model. The main inputs to any deformation modeling code are material properties and boundary conditions. As for the mechanical properties of the material, the flow stress data as a function of strain, strain rate and temperature have to be introduced to the FEM software. Conventionally, constitutive equations such as power law or sine-hyperbolic inverse law are utilized by fitting the experimental flow property data to suitable equations [116]. In the present case of Zr-2.5Nb-0.5Cu alloys, flow stress values were experimentally determined fora range of strains, strain rates and temperatures. However, these flow stress values could not be fitted to any single constitutive equation. This is on account of the fact that, within the range of temperature so interest, complications due to phase transformation, variation of relative amounts of phase with respect to temperature render fitting mechanical properties to a single equation difficult. Hence, a Look-Up Table (LUT) was used which had experimentally measured flow stress values for compression tests at a number of temperatures, strains and strain rates (see table 7.1).

The flow stress values for any intermediate values of temperature, strain and strain rate were calculated by trilinear interpolation scheme.

7.3. Modeling and simulation of Zr-2.5Nb-0.5Cu hot extrusion

Computation was made for velocity, temperature, stress, strain and pressure in the flow field and based on the stresses, forces on the tool were also determined. While deciding the meshing both tetrahedron and hexahedron elements were tried. The tetrahedrons however showed a stiff behavior and the extrusion force was heavily overestimated by these elements whereas hexahedral elements indicated reasonably good results hence hexahedral elements were finally used in the extrusion simulation.

During hot processing, the temperature has a significant influence on structural state and mechanical properties of billet. Furthermore plastic strains during hot extrusion processes are much larger than the elastic ones, those leads to the necessity of considering a thermoplastic process. Moreover, flow stress depends on effective strain, effective strain rate and temperature. Other mechanical properties are temperature dependent. The initial temperature was taken as input before submitting for each simulation run. Cooling of the surface in contact with the tools, as well as of the free surfaces takes place during the process (as can seen from figure 7.1), convection heat exchange between the workpiece and the tools and between the workpiece and the surrounding area was considered. Furthermore, the contact condition of surfaces between the workpiece and tools was also considered.

FEM based HyperXtrude program was used in conjunction with the determined flow properties to optimize the extrusion parameters.Direct flow data table was used for simulation purpose and its validity was checked using extrusion force directly obtained from Gleeble hot compression data.

7.3.1. Hot Extrusion of Zr-2.5Nb-0.5Cu Billet:

β-quenched billets of 142mm OD X 550mm length were mechanically jacketed with seamless copper tubes. Jacketed billet was preheated in a resistance heating furnace at 800^{o}C and extruded in a 3780T Horizontal Extrusion Press (HEP) maintaining extrusion ratio of 44:1 and ram speed in the range of 20 to 50 mm/sec. Billets were preheated in a resistance heating furnace and temperature were varied in the range of 700 to 850^{o}C. Copper jacketing of billet prevents oxidation of Zr-2.5Nb-0.5Cu billet and also provides the additional lubricant with oil based graphite. Copper cladding prevents direct contact of material with the extrusion tooling surfaces which otherwise would stick because of galling nature of Zirconium alloys. Copper jacketing remained on therod surface after extrusion was removed by dissolution into HF& HNO_3 solution.

7.4. Results and Discussion:

7.4.1. Flow properties of Zr-Nb-Cu:

Hot compression testing was carried out at four different temperatures using gleeble-3500 viz.700, 750, 815, 850 and 925^o C and constant true strain rates of 1.0, 5.0 and 10 S^{-1}. Cylindrical hot compression samples of size 10mm diameter and 15 mm length were used for compression testing. True strain value of 0.8 was used for conducting the test at all temperature and strain rates. Fig.7.2 a, b & c indicate the plot of true stress and true strain at varying temperatures and constant strain rate of 1,5 and 10S^{-1} respectively. Whereas, Fig 7.3 a, b and c indicate the plot of true stress and true strain at varying and constant temperature of 815, 850 and 925^{o}C respectively. The table 7.1 lists the flow stress value as function of temperature, strain and strain rate.

Table 7.1: Look-Up Table (LUT) showing different experimental flow stress values for different temperatures, strains and strain rates. Flow stress values for only one strain value are shown here.

Temperature (^{0}C)		**700**	**750**	**815**	**850**	**925**
Strain	**Strain rate(s^{-1})**					
0.5	0.01	70.9	40.8	34.8	27.1	18.5
	0.1	128	78.5	49.2	39.5	30.3
	1	180.4	120.6	67.1	63.4	47.4
	5	210.2	142.5	90.1	81.8	66.3
	10	229.3	164.7	103.4	92.7	75.4
0.6	0.01	65.4	36.9	34.6	26.6	18.2
	0.1	118.1	72.6	47.7	38.3	29.5
	1	167.6	114.6	69.4	64.7	48.0
	5	195.5	135.2	87.4	79.5	65.7
	10	214.3	156.1	100.3	91.1	74.1

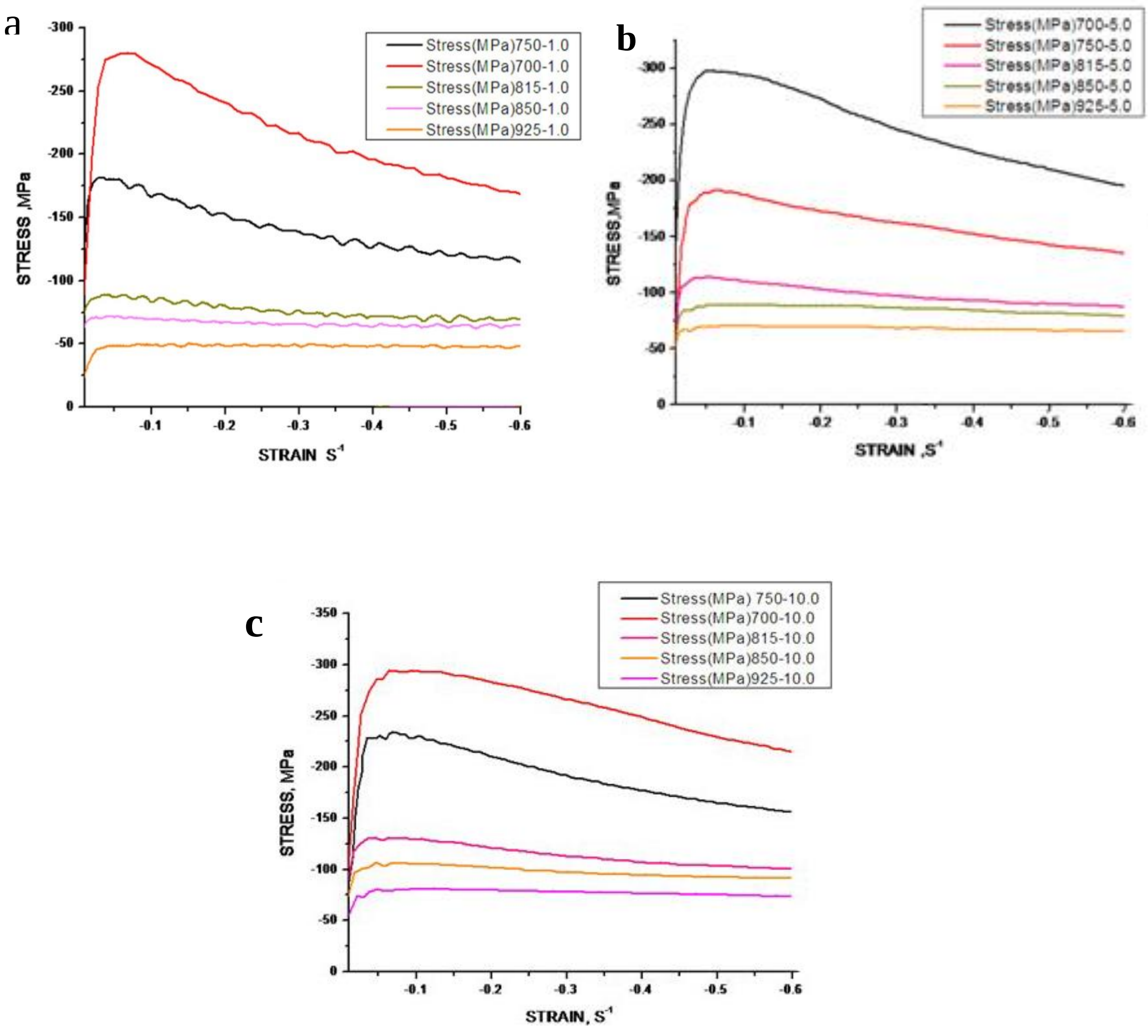

Fig 7.2(a-c) Shows stress strain behaviour at difrrtent temprature of Zr 2.5 Nb 0.5 Cu alloy at 1, 5, 10 S^{-1} strain rate respectivly

Fig. 7.2(a), (b) and (c) show there is wide variation of flow stress at low temperature with true strain (ε) and as expected flow stress decrease with increase in temperature for a given strain rate ($\dot{\varepsilon}$). Extent of decrease in flow stress is higher for low temperature flow curves i.e. 700°C & 750^0C compare to 815, 850 and 925^0C. The flow of material at lower temperatures do not stabilizes with the increase of strain which can lead plastic instability while deformation of material in lower temperature region where volume fraction of alpha phase is likely to be very high. However, this decrease in flow stress is reduced once temperature of material increases from 815°C and flow behavior indicates to get stabilized after the strain of 0.3 to 0.4. Fig. 7.3(a), (b) and (c) indicate that at constant temperature as the strain rate increases from 1 to10s^{-1}, peak flow stress increases significantly while as deformation progresses this variation is reduced.

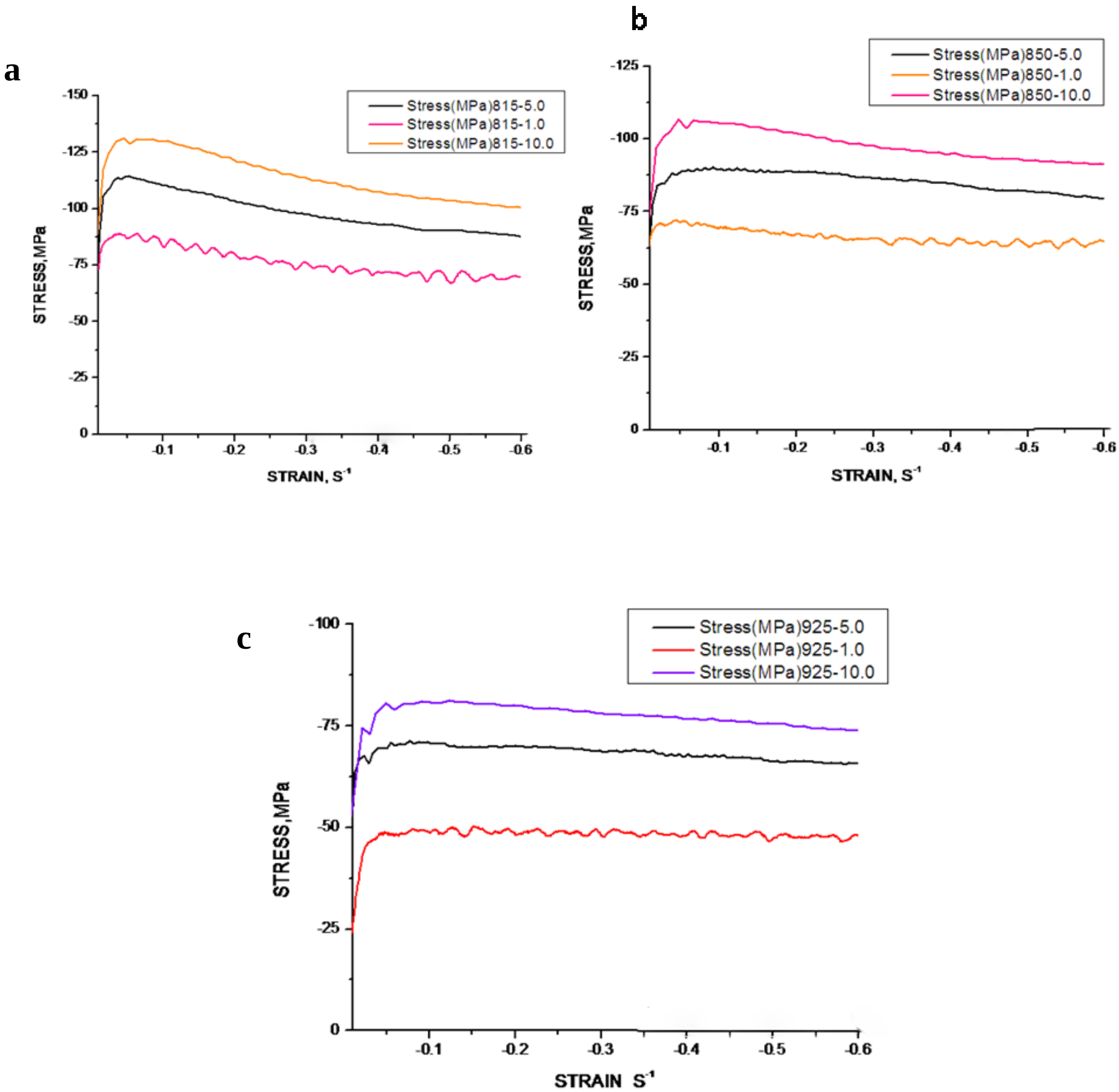

Fig 7.3 (a-c) Shows stress strain behaviour at difrrtent value of strain rate for 815 °C, 850 °C, and 925 °C

It was also observed from characteristics of all the flow curves that irrespective of temperature there is serrations in the plastic flow at low strain rate i.e. strain rate of 1.0 S^{-1}. But the extent of serrations reduces as test temperature is raised beyond 815°C. Fluctuations in plastic flow low strain rate and lower temperature region mainly occur in HCP metals due to formation of adiabatic shear band and dynamic recovery in this region. Extrusioncarried out in this region and it shows flow instability in extruded material. In other Zirconium alloys such as Zr-2.5% Nb, where same kind of studies have been made elsewhere shows flow curves having less fluctuation. Presence of copper Zr-2.5%Nb is responsible for reduction in tendency for dynamic recrystallization. High temperature deformation of this alloy at high strain rate provides very smooth flow curve and it is considered as flow curve suitable for dynamic recrystallization.

Microstructure of Two Phase Zr-2.5Nb-0.5Cu: Deformation of Zr-2.5Nb-0.5Cu was carried out mainly in two phase region and microstructure developed at 815^0C had fully recrystallized lamellar structure ,which consists of lamella of α-phase aligned longitudinally in direction of deformation. Fig 7.4 shows thin layer of β-phase was sandwiched between lamella of α-phase. Microstructural observation indicates stable flow and fully recrystallized structure at optimised extrusion temperature and strain rate.

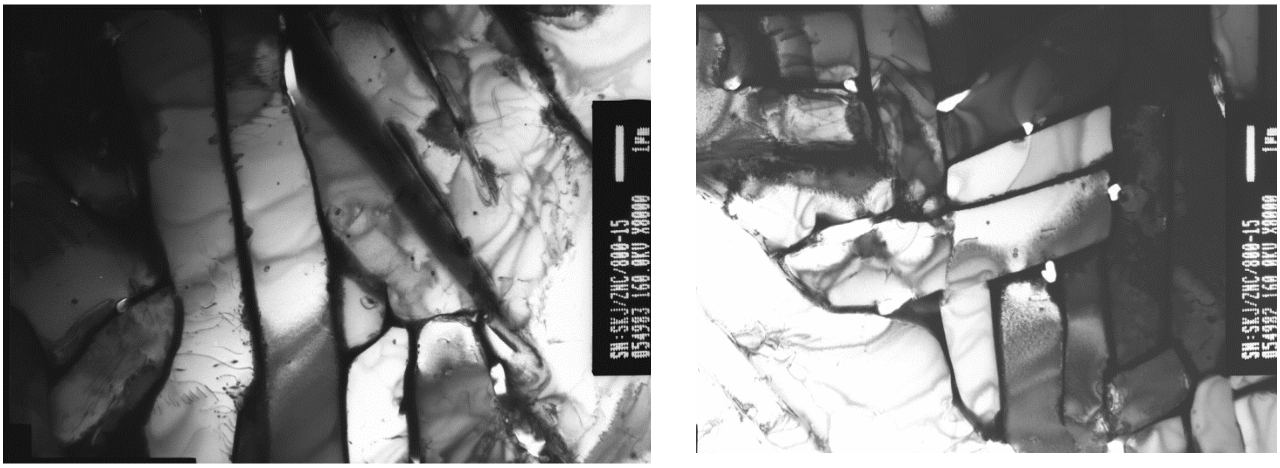

Fig 7.4. Recrystallised microstructure of Zr-2.5Nb-0.5Cu deformed at 815^0C strain rate of 1 S^{-1}

7.4.2. Results of extrusion Simulation:

Extrusion forces were determined by inserting data obtained from hot compression testing for different temperature and strain rate. Since, for Zr-2.5%Nb-0.5% Cu no constitutive equation is available hence, the actual flow properties data obtained by hot compression tests in Gleeble-3500 were used for simulation for extrusion model. Fig. 7.5(a) shows the variation of extrusion force along the billet length for die angle of 60^0 and at temperature of 815^0 C, as a function of ram speed from 20 mm/sec to 50 mm/sec. there is increase in peak extrusion force as ram velocity increases which results in increase of strain rates. Similar trend in increase of peak flow stress can be seen in the flow curves obtained for all temperatures. It can be seen that for a given ram speed as the extrusion length decreases, the extrusion load increases which is contrary to the conventional extrusion concept of reduced friction force load should decrease. In this case load increase due to temperature loss is more predominant than reduced friction load with surface area contact with container.

It was analyzed that during extrusion of billet at a constant ram speed cumulative heat loss from the billet to the tooling over extrusion time duration is dominant and increasing the flow stress as compared to softening effect of deformation temperature rise.

The peak extrusion loads at 815^oC for different ram speed are shown in fig 7.5b. It can be seen that with increasing initial speed the peak load requirement for extrusion increases almost linearly, this suggests that for a given extrusion temperature there ram speed should be minimum to reduce peak load. Temperature contours for different extrusion speed obtained in simulation are shown in Fig 7.6 (a). Simulation results for the temperature variation across the radius billet during hot extrusion have been shown in fig 7.6 (b)-(e). This temperature distribution across the radius has been plotted for after 2 secs and 20secs of extrusion at 815^oC, i.e at the start and almost end of extrusion respectively. This can be interpreted in terms of temperature variation between the leading and the trailing end of the extrudate. Graphs 7.6 (b-e) clearly indicates that for a given extrusion temperature as the extrusion speed increases from 20 mm/sec to 50 mm/sec the temperature variation between leading end and trailing end nearer to surface over the length reduces from about 15^oC to 5^oC. This is mainly due to higher deformation heat increase takes place at higher extrusion ram speed compensating the billet heat loss to the tooling to the greater extent.

a

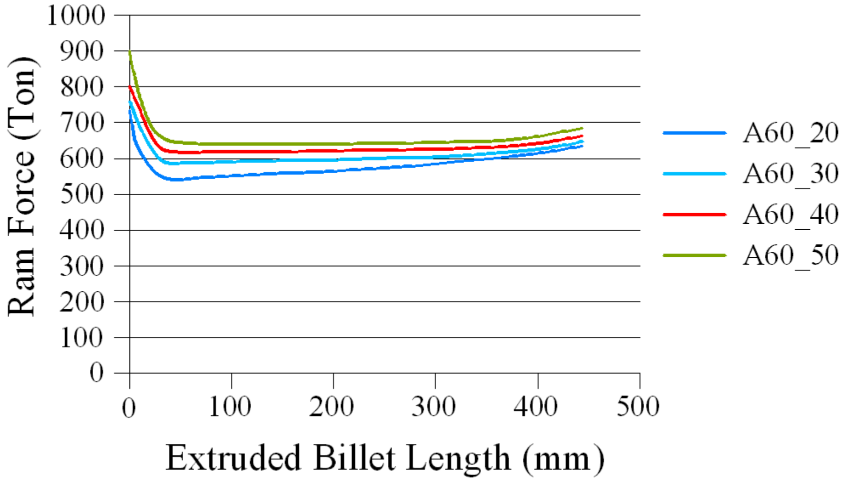

b

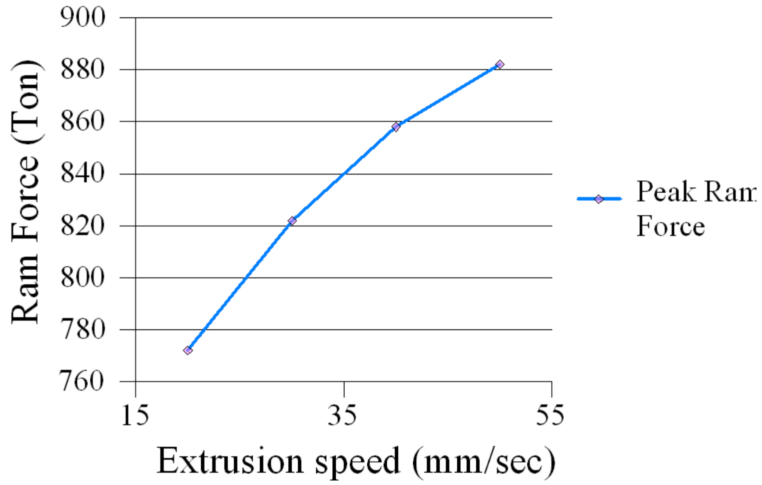

Fig 7.5 (a) showing extrusion force along the billet length at 815 °C, die angle 60° for ram speed 20 to 50 mm/sec. (b) showing peak ram force at varying extrusion speed at 815 °C.

a

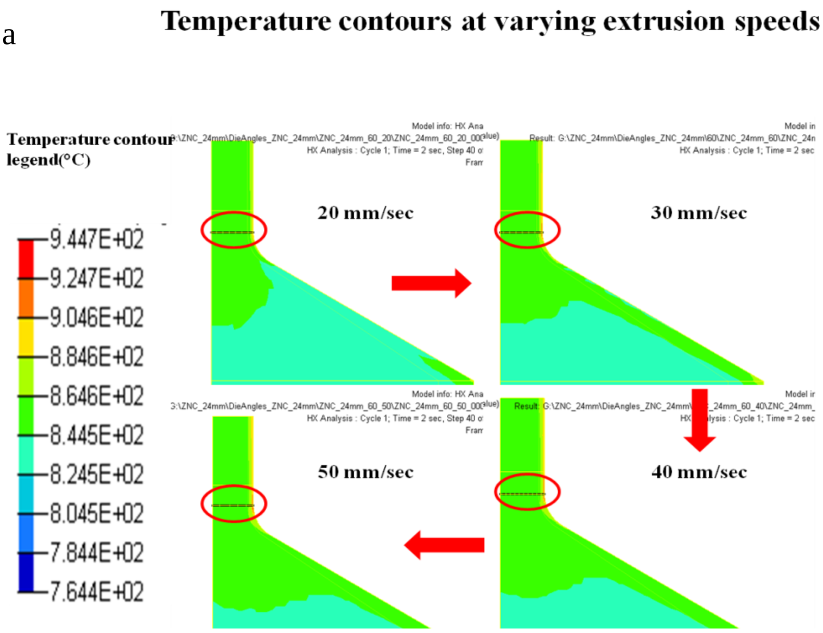
Temperature contours at varying extrusion speeds
Temperature contour legend(°C)
9.447E+02
9.247E+02
9.046E+02
8.846E+02
8.646E+02
8.445E+02
8.245E+02
8.045E+02
7.844E+02
7.644E+02
20 mm/sec
30 mm/sec
40 mm/sec
50 mm/sec

b

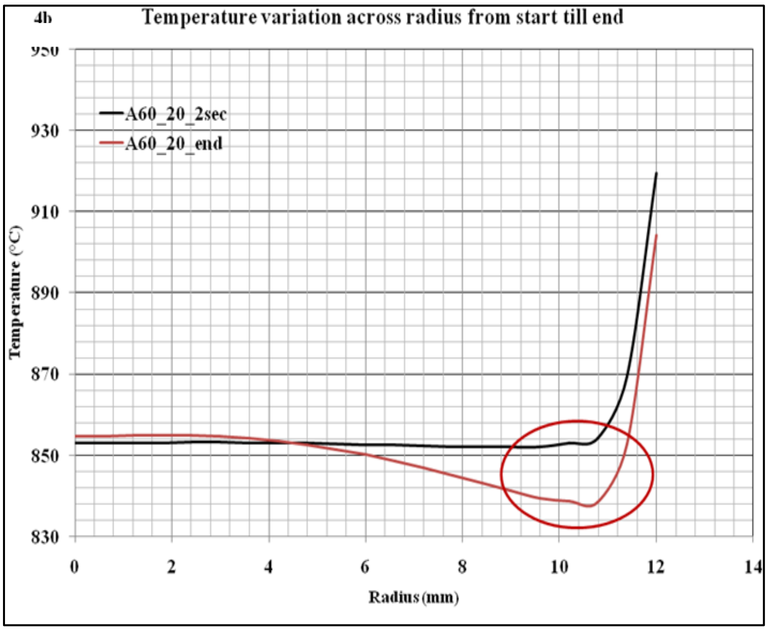
4b
Temperature variation across radius from start till end
A60_20_2sec
A60_20_end
Temperature (°C)
Radius (mm)

c

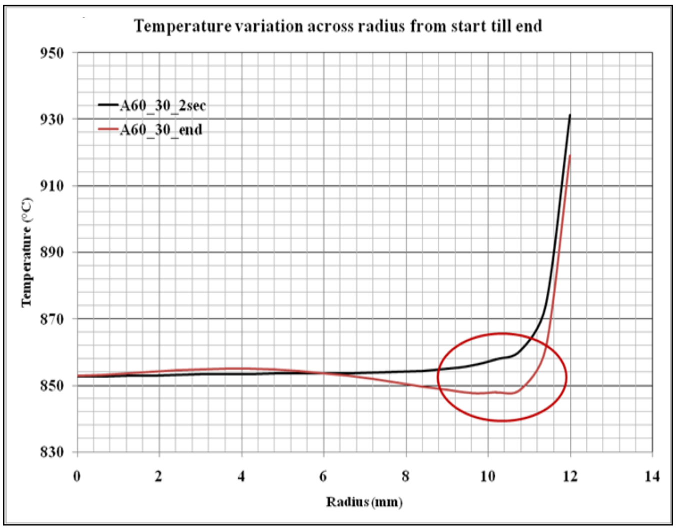

d

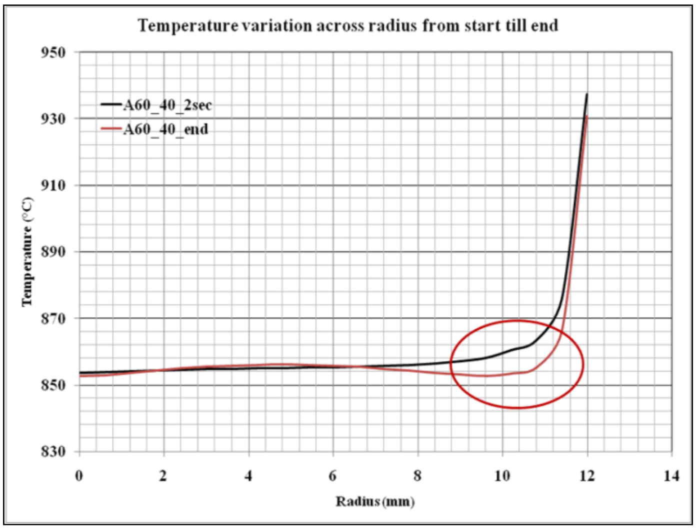

e

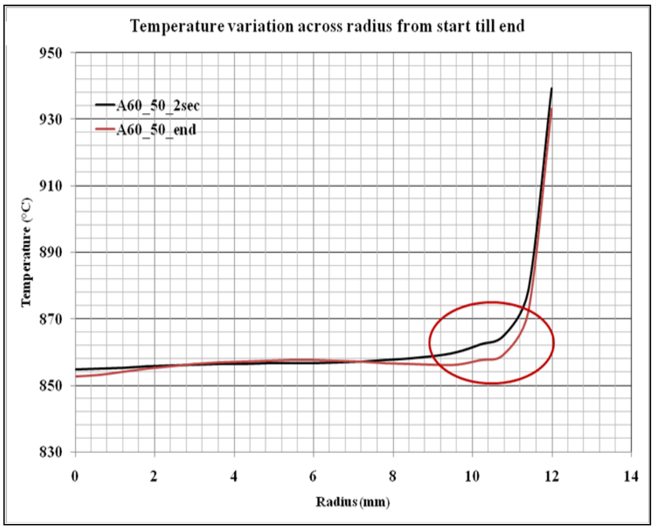

Figure 7.6 (a) simulation of temprature profile during the extrusion (b-e) temprature v/s radius of tube

7.5. Summary:

a) Flow behavior of Zr-2.5Nb-0.5Cu alloy at lower temperature results shows flow instabilities, and results from extrusion also shows similar results.

b) At lower strain rate there is fluctuations of flow stress which is not used for hot deformation of this alloy

c) Optimization of extrusion temperature and ram speed was done within this work for extrusion of Zr-2.5Nb-0.5Cu alloy.

7.6. Reference

[1] A. Paine, M. Aloe, and J. Walters. Simulation of hot extrusion processes. Aluminium Extrusion, 7(1):39–44, 2002.

[2] Sofia Hansson, Doctoral thesis, Modeling of the Stainless Steel Tube Extrusion Process, Lulea University of Technology ,Department of Applied Physics and Mechanical Engineering, Division of Material Mechanics.

[3] Mahender P. Reddy Computational Mechanics Company, Austin, TX.78757 and Olivier P. Hardy, Harold L. Thomas, Pramod R. Bangarpet Altair Computing, Inc., World Head Quarters, Troy MI, 48084, Optimal Design Of Extrusion Dies Using Hp-Adaptive Finite Element Model, Aiaa-98-4790.

[4] Monica Relli, Francesco Agostoni , Mahender P. Reddy, HakanCarlsson, Ola Bergqvist, Numerical Simulations of Flow Near Bearings During Aluminum Extrusion, 5th World Congress “Aluminium 2000”. Rome, Italy. 18-22 March 2003.

[5] Mahender P. Reddy, Edward G. Schaub, Computational Mechanics Company, Inc., Austin, TX Louis G. Reifschneider, Industrial Technology Department, Illinois State University, Normal, IL Harold L. Thomas, Altair Computing, Inc., Irvine, CA, Design And Optimization Of Three Dimensional Extrusion Dies Using Adaptive Finite Element Method, Presented At Antec'99 New York.

[6] Mahender P. Reddy, RavisankarMayavaram, David Durocher, HakanCarlsson, Ola Bergquist ,Altair Engineering, USA , Altair Engineering AB, Sweden, Analysis and Design Optimization of Aluminum Extrusion Dies, 8th International Extrusion Technology Seminar – Orlando, FL – May 2004.

[7] Mahender P. Reddy, Osama N. Hamzeh, Computational Mechanics Company, Inc., Austin, TX Charlotte Svensson, HakanCarlsson, Altair Engineering AB, Lund, Sweden,

Optimization Of Bearing Surfaces In Aluminum Extrusion Die Design, Presented At Opticon ’99.

[8] PHLEXprocess 1.0 An hp-adaptive Finite Element Program for Materials Processing, ComputationalMechanics Company, Inc. Austin, TX. (1998).

[9] Reddy, J. N., and Reddy, M.P., “Three Dimensional Finite Element Analysis of Non-Newtonian Fluid Flows,” in Fluid DynamicsReview, W. G. Habashi (ed.), John Wiley & Sons, pp.437-485, (1995).

[10] Ainsworth, M., and Oden, J. T., “A posteriori error estimation in finite element analysis,” Comput.Methods Appl. Mech. Engg., Vol 142**,**pp. 1-88,(1997).

Chapter 8

Important Results obtained from this thesis

1. Thermo-mechanical properties of as cast Zr-Sn alloy were studied and flow curves obtained show wide variation in flow stress with changes in strain and strain rates. In low temperature region, flow stress increases continuously with increase in strain and strain rate and microstructure shows non-uniform deformation. Micro-texture of entire deformation range has shown wide variation in texture. As deformation is carried out at higher temperature i.e. more than 700^0C and strain rate initiation of dynamic recrystallisation takes place at a temperature of about 750^0C flow stress also becomes constant throughout the deformation regime. Extensive characterisation of entire deformation range with respect to microstructure and texture has been done to know the variation in microstructure in wide range of temperature.
2. Dynamic recrystallization has occurred at 750° C and above, with the microstructure showing recrystallized grains and the flow curves display no appreciable work hardening. Noticeable work hardening was observed in the deformation at temperatures below 750°C, with no signatures of dynamic recrystallization in the corresponding microstructures.
3. Dynamic recrystallization was seen to occur at 750° C and above, with the microstructure showing recrystallized grains and the flow curves displaying no appreciable work hardening. This result has provided reason to deform the cast ingot of ZrSn at higher strain rates to get recrystallised structure.

4. At 900° C, the microstructure changed from the Widmanstatten structure of β to α transformation variants to equiaxed grains as the strain rate was increased. A high strain rate of $10S^{-1}$ was found to be required to result in complete dynamic recrystallization, overriding the microstructural features of β → α phase transformation. This result has unique application in deformation process of as cast alloy in which deforming at high strain rate, it is possible to produce dynamically recrystallised structure. With increased rate of deformation it becomes very easy in beta phase to provide large amount of deformation with less power.
5. Based on the present results, the temperature of 750° C appears to provide a wide margin of possible strain rates at which equiaxed recrystallized microstructure could be obtained and hence, this temperature may be deemed suitable for hot working processes.
6. Processing maps developed for cast alloy has wide range of flow instabilities. As the deformation is carried out at higher temperature flow instabilities reduce and Zr-Sn alloy deforms by dynamic recrystallisation. New information has emerged with this work indicate that in Beta phase working of this material instead of a widmanstatten structure it is possible to get fully recrystallised structure for strain rate of $10\ S^{-1}$. This result has significant industrial applications. Result obtained from above study has significant application in deformation of cast material of other alloys, where it is possible to make similar type of studies to know the flow behaviour in a cast alloy.
7. Development of constitutive equation for as cast Zirconium alloys and its validation is completely new work carried out in this thesis and results have been also validated with bulk deformation process. Future work in this area can be done to develop constitutive equation for other cast alloys which can provide significant information not only for their deformation but also design data.

8. Co-extrusion parameters for Zircaloy-2 and Zr-Sn have been studied extensively and criticality in co extrusion has been identified by simulation results from this work. Simulated results have been validated for co-extrusion with an error of about 4%. Effect of extrusion temperature, die angle and ram speed were simulated using FEM based software and validation of model not only for microstructure but also liner thickness variation have been done. This work has potential application in development of duplex and also triplex clad tube for high burnup fuel. Methodology adopted here can be also used in development of other coextruded tubes in high technological applications.
9. In simulation work of Zr-2.5Nb-0.5Cu extrusion parameters have been optimized. It shows the effect of ram speed on increase in surface temperature, which provides crucial information in designing extrusion without surface defects and variation of microstructure from surface to centre.

Finally it is obvious from results and analysis from this thesis, that type of work initiated in new areas can be extended to do analysis of many more alloys.